6.8 Tptpll THC MODEL REV02

The Tptpll THC Model REV02 presented in this section is an update of the REV01 model presented in Section 6.7. This model uses the same stratigraphic column and numerical grid (including drift design) as the REV01 model, but with updated rock thermal and hydrological properties. In-drift thermal properties remain unchanged since the REV01 model. Key elements of this model include:

- Initial heat load of (1.45 kW/m) (Attachment VIII)

- 50-year preclosure period with 86.3% ventilation efficiency

- Drift in the Tptpll unit

- Model stratigraphy at a location near the center of the repository (at approximately Nevada State Plane coordinates E170572, N233195)

- Use of an extended-case geochemical system (Section 6.2.2.2)

- Drift wall open to fluid and gas advective and diffusive fluxes

- Vapor pressure lowering due to capillary pressure (Section 6.4.6)

- Updated rock thermal and hydrological properties (Section 4.1.2)

- Updated thermodynamic data (Attachment VI and Section 4.1.4)

- Updated kinetic data (Section 4.1.5 and Table 4.1-4)

- Use of most recent TOUGHREACT V3.0 (LBNL 2002 [161256]). This version takes into account the precipitation of solids in dry gridblocks where water influx occurs and therefore models more precisely the mineral deposition at the boiling front.

In addition, this revised model was used to conduct a broader range of evaluations than done previously with the Tptpll THC Model REV01, including simulations using:

- Different input thermodynamic data (ambient conditions)

- Five different input water compositions (Section 6.2.2.1 and Table 6.2-1)

- Fixed and variable infiltration rates

- Different water-vapor-pressure models (with and without vapor-pressure lowering)

- Two values of CO_2 gas molecular diameter (resulting in a six-fold difference in the diffusion coefficient).

6.8.1 Numerical Mesh (Tptpll)

Simulations of thermal loading were performed on a vertical 2-D mesh identical to the mesh described in Section 6.7.1 (Figure 6.7-1), and representing the same stratigraphic column (Table 6.7-1). The drift discretization was not changed from REV01 (Figure 6.7-2), with the same preclosure and postclosure configurations as implemented previously (Section 4.1.7 and 6.7.1).

Simulations of ambient conditions (no thermal load) were run with a one-dimensional (vertical column) grid having the same stratigraphy and vertical discretization as the Tptpll 2-D mesh. This 1-D model does not have a drift opening and uses uniform vertical gridding through the area cutting across the drift on Figure 6.7-2. This approach is different than for REV01 ambient simulations (Section 6.7), which were carried out on the same 2-D mesh (including a drift opening) as used for simulating thermal loading. The use of 1-D columns here was adopted to speed up the computational effort. Because of the no-flow boundary conditions existing on each side of the model mesh, the horizontal geologic contacts, and the laterally continuous rock properties, 2-D simulations under ambient conditions are essentially the same as 1-D simulations (vertical flow only). Close to the drift, however, flow is diverted around the drift opening because of the capillary barrier created by this opening. Therefore, the only differences between 1-D and 2-D ambient simulations result from the effect of the drift opening.

6.8.2 Boundary Conditions

Boundary conditions were set as in the Tptpll THC Model REV01 (Section 6.7.2), except for the higher preclosure ventilation efficiency and another important difference: the drift wall was specified open to advective gas and liquid fluxes (Section 4.1.7) (Table 6.8-1). Also, three cases of infiltration were considered, as shown below in Table 6.8-2.

One-dimensional simulations of ambient conditions were run with the same boundary conditions as the 2-D runs, except that these simulations did not include a drift opening. A constant infiltration rate of 6 mm/yr was used in 1-D simulations to evaluate the model sensitivity to thermodynamic data (Section 6.8.5.1). The Mean Infiltration case in Table 6.8-2 (step-wise infiltration increase) was used for all other ambient simulations (Section 6.8.5.2).

Table 6.8-1.   Tptpll THC Model REV02 Boundary Conditions

Boundary	Boundary Condition	Reference
Top	$T = 16.13°C$	Table 4.1-1
	$S_g = 0.99$	Table 4.1-1
	$P = 84725$ Pa	Table 4.1-1
	Time-varying infiltration rate (mean infiltration regime only)	Table 6.5-3
	Constant composition of infiltration and PCO_2	Table 6.2-1
Bottom	$T = 32.62°C$	Table 4.1-1
	$S_L = 0.99999$	Table 4.1-1
	$P = 92000$ Pa	Table 4.1-1
	Constant water composition and PCO_2	Table 6.2-1
Sides	No flux for water, gas, heat, and chemical species	Not Applicable
Drift Wall	Open to gas and liquid fluxes (advective and diffusive); conduction only for heat.	Not Applicable
Waste Package	Initial full heat load of 1.45 kW/m decreasing with time (due to radioactive decay), and reduced by 86.3% during the first 50 years (due to heat removal by ventilation)	Attachment VIII and Table 4.1-2

NOTES: T = Temperature
S_g = Gas saturation
S_L = Liquid saturation
P = Pressure

Table 6.8-2.   Tptpll THC Model Infiltration Rates

Case	Infiltration Rate (mm/y)	Time Period (years)	Reference DTN
Mean Infiltration (increasing stepwise)	6	0 to 600 (present day)	Table 4.1-1
	16	600 to 2000 (monsoon)	
	25	2000 to 100,000 (glacial transition)	
Mean low (fixed)	6	0 to 100,000	NA (sensitivity only)
Mean high (fixed)	25	0 to 100,000	NA (sensitivity only)

NOTE: All simulations were carried out with the Present Day Mean calibrated rock properties set. Also see Table 6.8-4.

6.8.3 Input Data and Modeling Procedure

The Tptpll THC Model REV02 was run using TOUGHREACT V3.0 (LBNL 2002 [161256]). Simulations were carried out in the same manner as done for REV01 (Sections 6.5.3 and 6.7.3). Many input data were revised, compared to the Tptpll THC Model REV01 (Section 6.7.3). The revised data include: rock properties (Section 4.1.1, Table 6.4-1), modeled geochemical system (Table 6.2-2: the addition of nitrate and sepiolite), thermodynamic data (Attachment VI), and kinetic data (Table 4.1-4). In addition, five water compositions were considered (Table 6.2-1), as discussed in Section 6.2.2.1 and summarized below in Table 6.8-3.

Table 6.8-3. Selected Input Waters (Section 6.2.2.1) for the Tptpll THC Model REV02

Name of Alternative	Sample or Water Name	Location	Lithostratigraphic Unit
W0 (also used in REV01)	HD-PERM[1]	ESF Alcove 5	Tptpmn
W5	CS-1000/7.3-7.7/UC	ECRB Cross Drift	base of Tptpul
W4	CS-2000/16.5-21.1/UC	ECRB Cross Drift	Tptpll
W6	SD-9/990.4-991.7	Borehole SD-9	Tptpll
W7	CS-500/12.0-16.7/UC	ECRB Cross Drift	Tptpul

NOTE: [1] Average of two samples as discussed in Section 6.2.2.1.
See Table 6.2-1 for compositions.

The noteworthy revisions to the Tptpll rock properties since REV01 include a two-fold decrease in fracture porosity and permeability, a one-order-of-magnitude decrease in matrix permeability, and some decrease in the capillarity of fractures (by 20%) and rock matrix (by 40%). The revised rock thermal properties account for the presence of lithophysae in the Tptpll (and other lithophysal units), although they do not differ significantly from the earlier data (Table 6.4-1).

The diffusion coefficient of CO_2 in gas was increased in this model compared to the REV01 model. This change was unintentional and resulted from inserting a default molecular diameter $(1 \times 10^{-10}$ m) into the thermodynamic database during automatic conversion of this database. The value used in previous models $(2.5 \times 10^{-10}$ m) was specific for CO_2 (Section 4.1.6). This change in molecular diameter, through the use of Equation 4.2-1, causes approximately a six-fold increase in the CO_2 diffusion coefficient. This change, however, is within the range of uncertainty affecting the calculation of gas diffusivity in the model. It was used as an opportunity to evaluate the model sensitivity to CO_2 diffusivity. In order to do so, an additional simulation was run using the original CO_2 molecular diameter value $(2.5 \times 10^{-10}$ m), with results compared in Section 6.8.5.3.

Simulations of ambient conditions (i.e., without thermal loading, under natural geothermal gradient, and without drift opening) were run using the same input data as described above. However, to evaluate the model's sensitivity to thermodynamic data (Section 6.8.5.1), three different sets of thermodynamic data were used, as described further in Section 6.4.8.2: "Set 1," the current database, and alternative data sets "Set 2" and "Set 3."

The maximum time step length allowed for transport was reduced significantly, compared to REV01 simulations, to minimize the effect of numerical errors. Maximum time steps of 15 days, 1 month, 2 months, 1 year and 5 years were used for the time periods spanning 0–50, 50–600, 600–2,400, 2,400–20,000, and 20,000–100,000 years, respectively. To change infiltration rates and the maximum time step length, each run was stopped and then restarted at 50, 600, 2,000, 2,400, and 20,000 years after changing these input data. These differences apart, the same modeling procedure was applied as previously (Sections 6.5.3 and 6.7.3).

6.8.4   Model Runs

Sixteen simulations were performed, as summarized in Table 6.8-4.

Table 6.8-4.   Tptpll THC Model REV02 Runs Using the Mean Infiltration Rock-Property Set for All Simulations

Input Water (Table 6.8-3)	Thermo. Data Set (Section 6.4.8.2)	Infiltration Case (Table 6.8-2)	Equation of State (EOS) Module[a]	Simulation Type	Run ID (used In Output-DTNs: LB0307DSTTHCR2.001; LB0307DSTTHCR2.002; LB0302DSCPTHCS.001; LB0302DSCPTHCS.002; also see Attachment X)
None	None	Mean Infiltration	EOS4	TH (2-D)	th6_1.45kw
W0	Set 1	Mean Infiltration	EOS4	THC (2-D)	thc6_w0
W0	Set 1	Mean Infiltration	EOS3	THC (2-D)	thc6_w0e3
W0	Set 1	Mean Infiltration	EOS3 (isothermal)	THC (1-D, ambient)	thc6_w0amb1
W0	Set 1	Mean Low (fixed)	EOS4	THC (2-D)	thc6_w0a
W0	Set 1	Mean High (fixed)	EOS4	THC (2-D)	thc25_w0
W0	Set 1[b]	Mean Infiltration	EOS4	THC (2-D)	thc6_w0b
W4	Set 1	Mean Infiltration	EOS4	THC (2-D)	thc6-w4
W4	Set 1	Mean Infiltration	EOS3 (isothermal)	THC (1-D, ambient)	thc6_w4amb1
W5	Set 1	Mean Infiltration	EOS4	THC (2-D)	thc6_w5
W5	Set 1	Mean Infiltration	EOS3 (isothermal)	THC (1-D, ambient)	thc6_w5amb1
W6	Set 1	Mean Infiltration	EOS4	THC (2-D)	thc6_w6
W6	Set 1	Mean Infiltration	EOS3 (isothermal)	THC (1-D, ambient)	thc6_w6amb1
W7	Set 1	Mean Infiltration	EOS4	THC (2-D)	thc6_w7
W0	Set 1	Mean Low (fixed)	EOS3 (isothermal)	THC (1-D, ambient)	thc6_w0amb
W0	Set 2	Mean Low (fixed)	EOS3 (isothermal)	THC (1-D, ambient)	thc6_w0_q
W0	Set 3	Mean Low (fixed)	EOS3 (isothermal)	THC (1-D, ambient)	thc6_w6_w0_q1

NOTE: [a]   TOUGHREACT V3.0 (LBNL 2002 [161256]) flow modules: EOS3 neglects vapor pressure lowering due to capillary pressure; EOS4 takes this effect into account.
   [b]   A CO_2 molecular diameter of 2.5×10^{-10} m (Section 4.1.6) is used for this run instead of the value of 1×10^{-10} m input in other simulations listed here (see Section 6.8.3).

6.8.5   Simulation Results (Tptpll THC Model REV02)

The model results are presented below in several subsections. First, THC simulations of ambient conditions (non-heating) using different input thermodynamic data sets are discussed (Section 6.8.5.1). These simulations serve as the basis for justifying the use of revised thermodynamic data selected for this study. Results of simulations of thermal loading (TH and THC) are then presented in two parts. Predicted water chemistry trends around the drift are presented first (Section 6.8.5.2), then the effect of water-gas-rock reaction on fracture permeability and flow patterns around the drift is assessed (Section 6.8.5.3). The results are presented in a way that allows comparison with earlier models (Section 6.5 and 6.7) and also allows an assessment of model sensitivity to input water compositions, infiltration rates, water-vapor pressure models, and CO_2 effective diffusivity. All model results were submitted to the technical database under DTNs as listed in Attachment X.

### 6.8.5.1   Simulations of Ambient Conditions (Thermodynamic Data Sensitivity)

Results of simulations of ambient conditions are presented below to illustrate the model sensitivity to thermodynamic data, and to justify the selection of the thermodynamic data used in this study (Attachment VI and Section 4.1.4). These simulations were run with three thermodynamic data sets discussed in Section 6.4.8.2: Set 1 representing the data adopted for this study, and Set 2 and Set 3 representing alternatives (mostly data from the YMP database data0.com.R2) that were considered but not chosen for reasons given below. These simulations were run with the HD-PERM input water composition (Table 6.2-1). For consistency between all runs, the total aluminum concentration of the initial water in runs using all data sets was recomputed for equilibrium with the illite phase from these alternative thermodynamic data sets.

Predicted ambient water composition trends with the three sets of thermodynamic data are shown in Figure 6.8-1 through 6.8-3. Set 2 leads to the least stable predicted compositions, including unrealistic pH fluctuations to near 10, very large depletion of calcium and magnesium, and an increase in sodium concentrations to around 500 mg/L after 100,000 years. On the other hand, the simulation with Set 1 predicts the most stable trends. Using Set 3 (i.e., by incorporating revised zeolite thermodynamic data into Set 2), trend stability improves considerably, but the magnitude of concentration changes over the 100,000-year simulated time period is still quite large for most species. With all three thermodynamic data sets, an unrealistic magnesium depletion in water is predicted to occur, primarily on account of sepiolite precipitation. However, the least predicted magnesium depletion occurs when using Set 1. Note also that simulations using Set 2 and Set 3 predict the total dissolution of calcite initially present in the model (with precipitation of zeolites and clays having calcium). Using Set 1, calcite dissolution is not predicted. For these reasons, Set 1 was deemed a better alternative than either Set 2 or Set 3, because it yields long-term water compositions more consistent with observed data than the other two sets. For these reasons, Set 1 was adopted for the rest of this study. It should be recalled here that most of these thermodynamic data are from the YMP database data0.com.R2, with changes from this database documented under DTN: LB0307THMBDRTM.001 [164434] (and summarized in Section 4.1.4 for major changes).

These simulations illustrate that for any fixed water composition close to equilibrium with a mineral assemblage, a small change in thermodynamic data can reverse the calculated degree of

saturation (i.e., from supersaturation to undersaturation and vice versa) of minerals in that water, and thus reverse the calculated direction of reactions between these phases. In such instances, different water-composition trends can be predicted regardless of the magnitude of reaction rates assumed in the model. In such cases, the reliability of model results can be more affected by thermodynamic data than by kinetic data.

Free energies for minerals such as clays and zeolites may never be known accurately enough such that adjustments within the (sometimes already small) uncertainty in these values will always be necessary for long-term ambient simulations. Whether these adjustment provide values that are better, or not, than the data0.ymp.R2 data depends on the data themselves and their intended use. For clay minerals, because the adjustments were made to better match measured water compositions at YM, these adjustments may in part compensate for other effects not directly modeled such as more complex solid solutions or ion exchange processes. Therefore, these values may not be "better" than those in the data0.ymp.R2 database, but are better suited for long-term reactive transport simulations at Yucca Mountain. For stellerite, the dominant zeolitic mineral in repository units, it would appear that the data used here (Fridriksson et al. 2001 [160460]) may be superior to the R2 data.
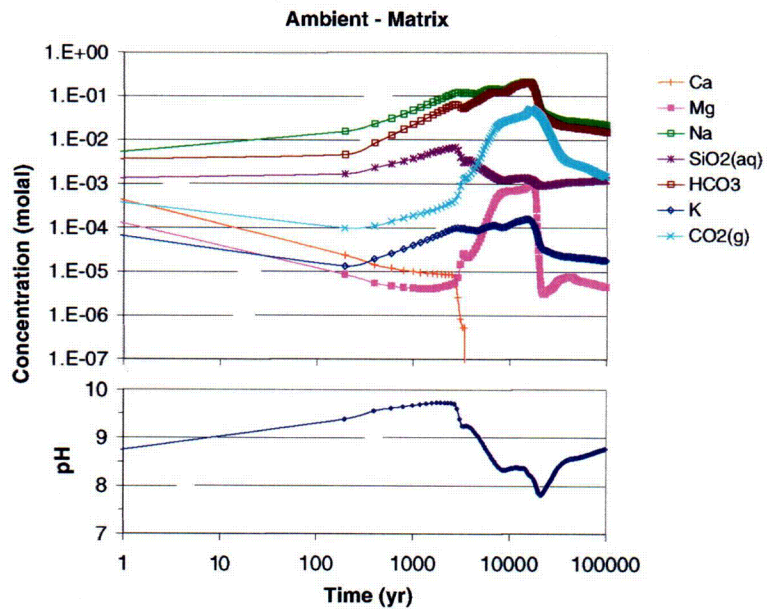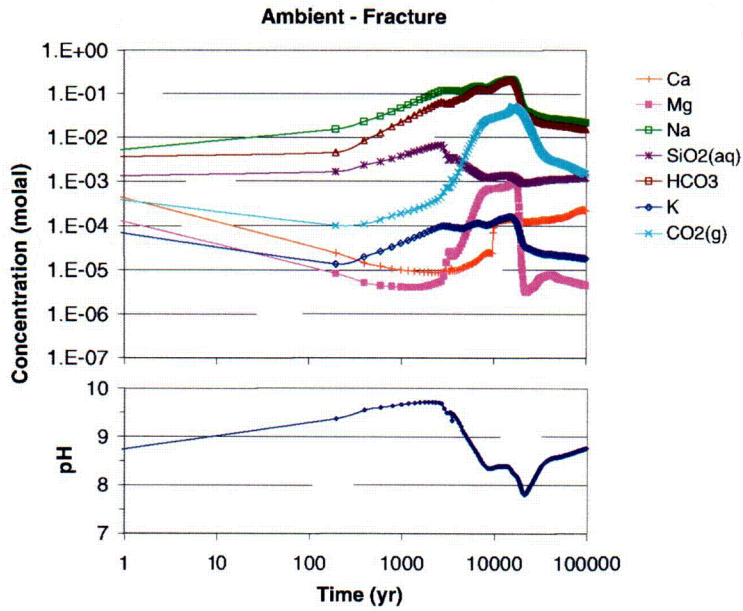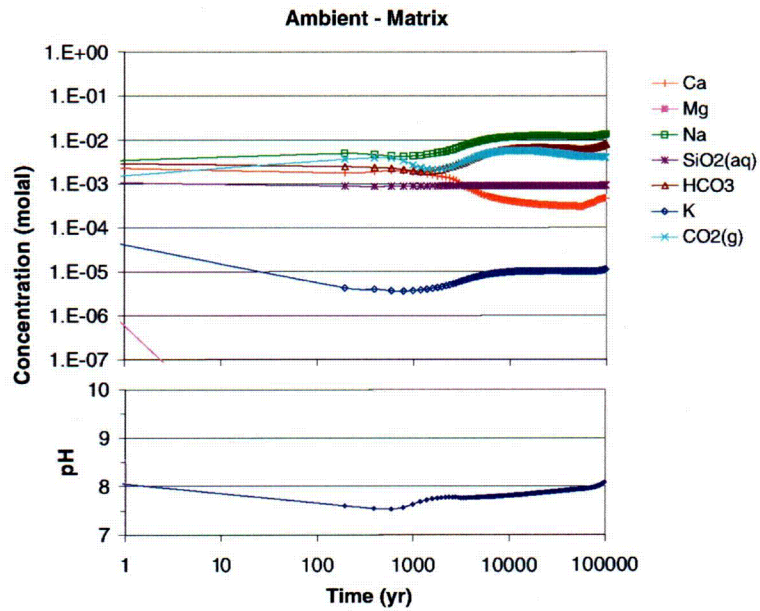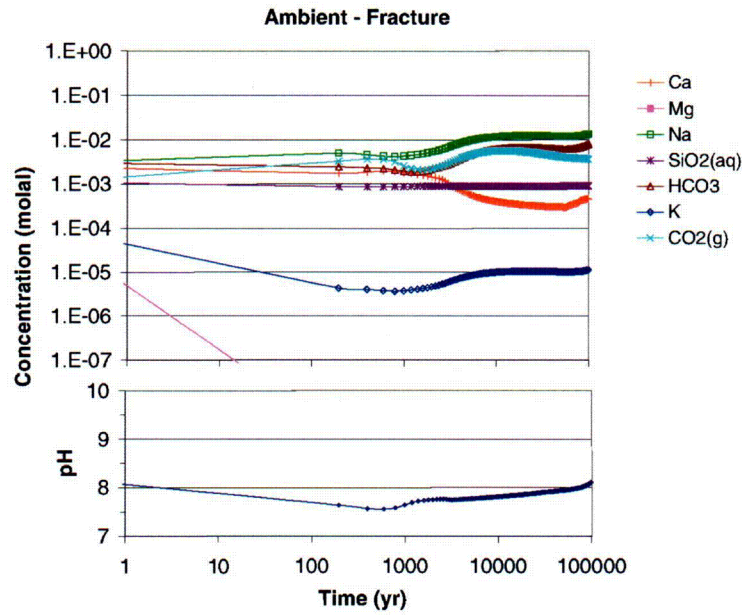
Ambient - Fracture

Ambient - Matrix
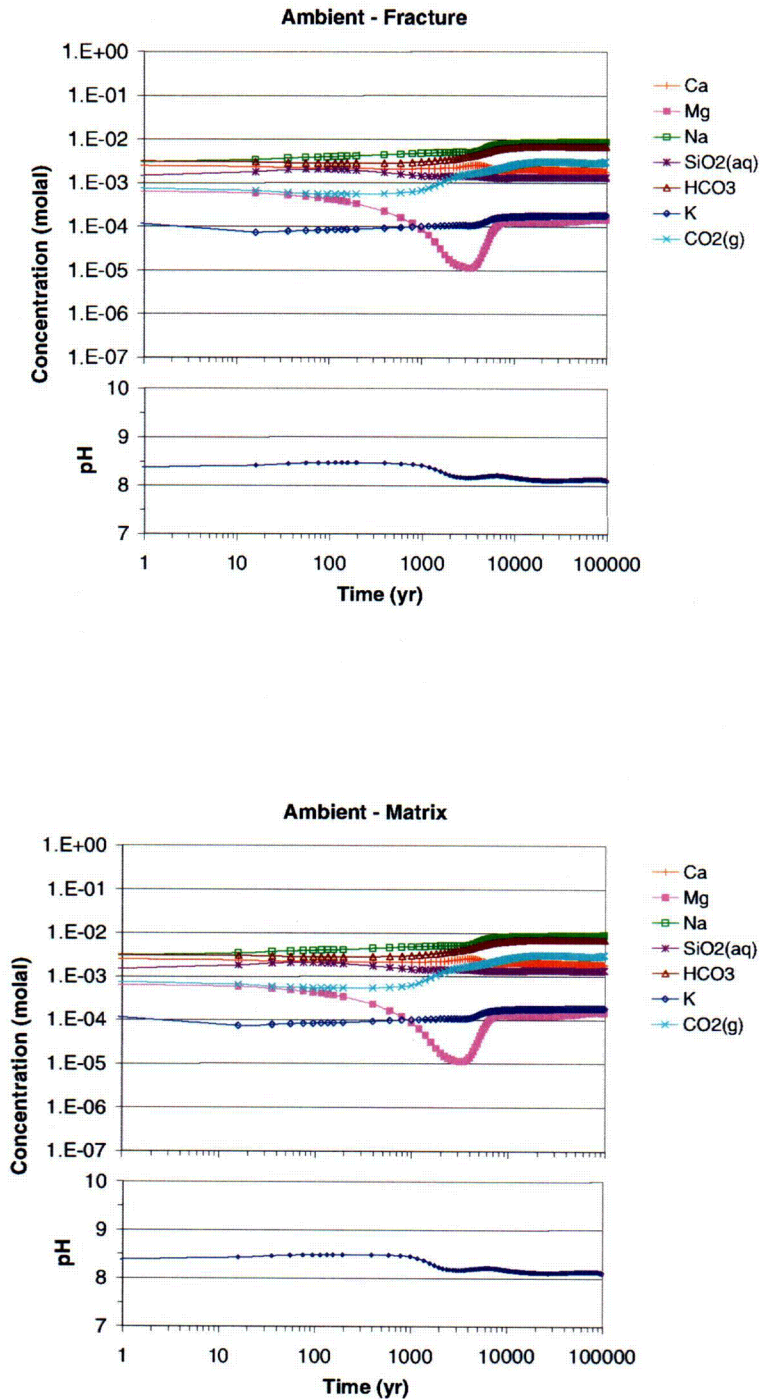
Output-DTN: LB0307DSTTHCR2.001

NOTE: Infiltration is constant at 6 mm/yr.

Figure 6.8-1. Predicted Water Compositions without Thermal Loading (in the Tptpll Lithostratigraphic Unit at the Repository Location) Using the Thermodynamic Data Adopted for This Study (Data Set 1—Attachment VI)

C54

Ambient - Fracture

Ambient - Matrix

Output-DTN: LB0307DSTTHCR2.001

NOTE: Infiltration is constant at 6 mm/yr.

Figure 6.8-2. Predicted Water Compositions without Thermal Loading (in the Tptpll Lithostratigraphic Unit at the Repository Location) Using Thermodynamic Data from Data Set 2 (Section 6.4.8.2)

C55

Ambient - Fracture

Ambient - Matrix

Output-DTN: LB0307DSTTHCR2.001

NOTE: Infiltration is constant at 6 mm/yr.

Figure 6.8-3. Predicted Water Compositions without Thermal Loading (in the Tptpll Lithostratigraphic Unit at the Repository Location) Using Thermodynamic Data from Data Set 3 (Section 6.4.8.2)

6.8.5.2 TH Results (No Chemical Reactions)

The results of TH simulations are shown in Figures 6.8-4 through 6.8-10. This set of figures parallels Figures 6.7-3 through 6.7-9 to facilitate comparison with the results of earlier simulations. It should be recalled that REV01 simulations were run with the EOS3 option of TOUGHREACT V3.0 [161256] (no vapor-pressure lowering caused by capillary pressure), whereas most REV02 simulations were carried out with the EOS4 option of TOUGHREACT V3.0 [161256] (taking this effect into account).

Modeled peak temperatures are approximately 10 degrees lower than in the REV01 model (Figures 6.8-4 and 6.8-5), mostly as a result of updated rock properties, but also because of the vapor-pressure-lowering effect, which was not considered in previous model revisions (see also temperature profiles from THC simulations discussed later). Preclosure temperatures around the drift are up to 30 degrees lower than in REV01 simulations (Figure 6.8-5), primarily because the heat removal rate (86.3%) is larger than what was used previously (70%). The main impact of vapor-pressure lowering is the smaller extent of dryout around the drift in the rock matrix than in fractures, even though temperatures are essentially the same in both media (Figure 6.8-6; also compare with Figure 6.7-4). Consequently, the rock matrix at the drift wall is predicted to rewet earlier (at around 200 to 300 years) than in previous models (1,200 to 1,400 years) (Figure 6.8-8). In fractures, however, the time of rewetting around the drift wall is similar for both model revisions (Figure 6.8-7). Predicted postclosure air mass fractions around the drift also did not change significantly from REV01 (Figure 6.8-9). The predicted vertical water percolation flux at the drift crown is somewhat higher during postclosure than calculated in REV01 (Figure 6.8-10; note that peaks of flux in this figure may not be fully resolved because such peaks are narrow relative to the time intervals specified for data output from the simulations). The predicted ambient water flux in the revised model (Figure 6.8-10) is for a 1-D column without a drift opening. It is larger than the flux calculated for ambient conditions in the REV01 model because it does not take into account the diverting effect of a drift opening (i.e., the diversion of percolating water around the drift capillary barrier). At most times (except around 50 and 1,200 years), the ambient water flux without a drift opening is also larger than the predicted flux above the drift under thermal loading conditions (Figure 6.8-10). Calculated temperatures, liquid saturations, and fluxes shown here are consistent with results of TH simulations presented in BSC (2003 [161530], Section 6.2.3). The vertical flux is further discussed in Section 6.8.5.4.

Note that in all models presented in this report, the drying of the rock caused by drift ventilation (i.e., the physical removal of moisture from wallrock by ventilation) is not considered. This drying could reduce the amount of water available for mobilization by boiling during postclosure. However, sensitivity studies in BSC (2001 [155950], Section 5.3.2.4.4) indicate that inclusion of preclosure dryout due to ventilation has little effect on TH conditions around the drift during the postclosure period, compared to a model that does not account for the influence of preclosure dryout. Therefore, inclusion of preclosure dryout is not expected to have a large effect on thermal seepage. The effect of evaporative concentration on pore water compositions would be more pronounced during preclosure than predicted here. However, the small effect of preclosure dryout on postclosure TH conditions is not expected to significantly affect water compositions during postclosure.
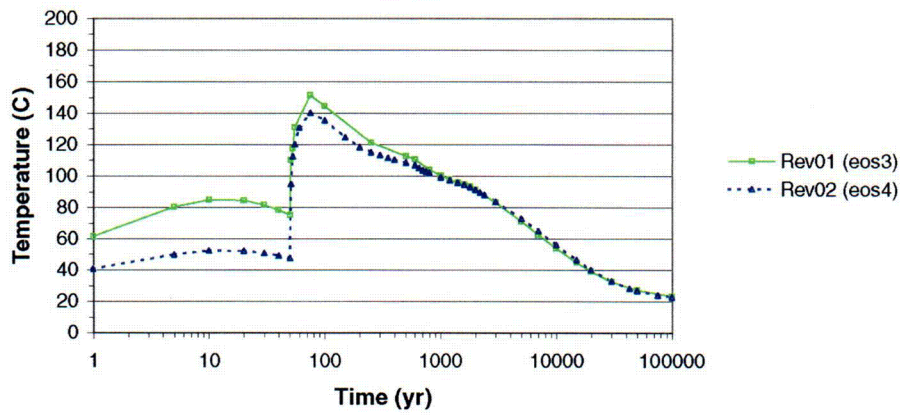
Thermal Only (Tptpll - Rev02)
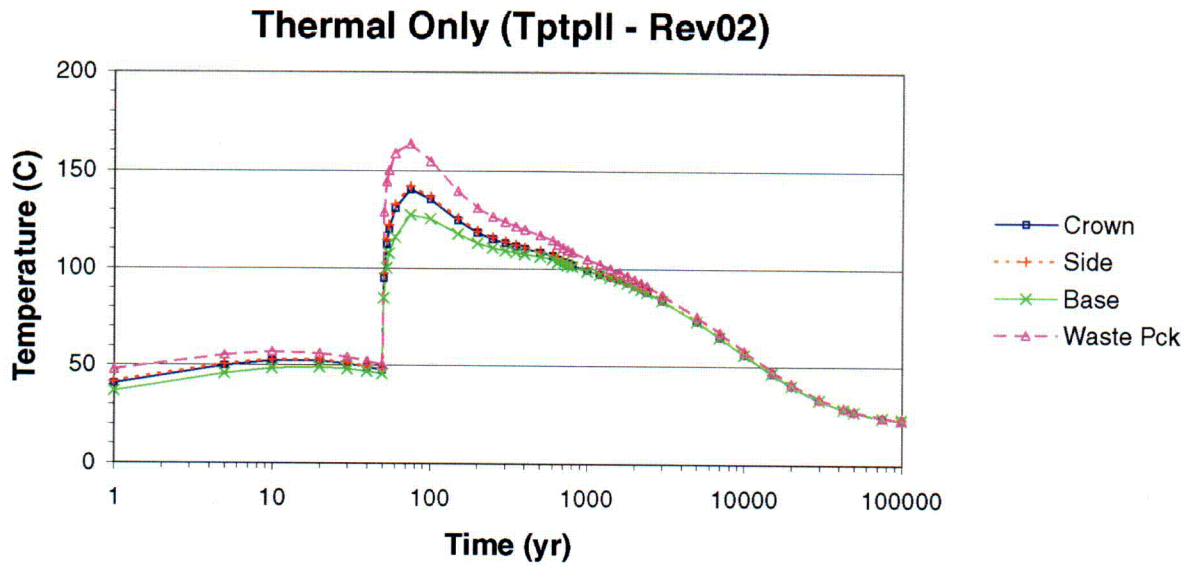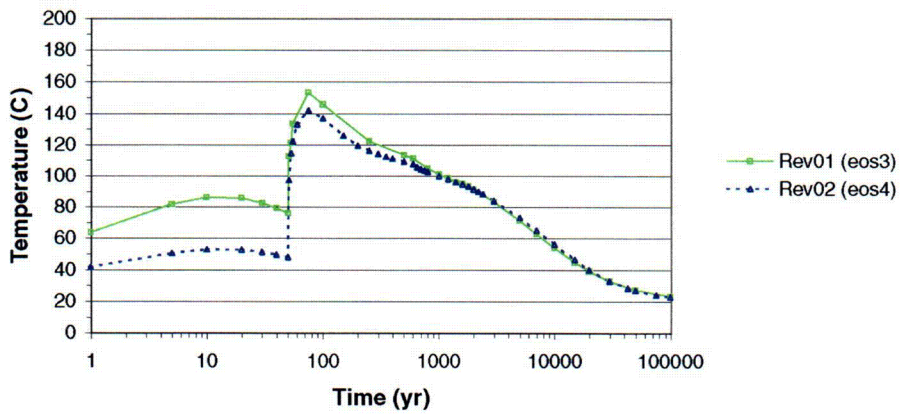

Output-DTN: LB0307DSTTHCR2.002

Figure 6.8-4. TH Simulation (Tptpll, REV02): Time Profiles of Modeled Temperatures in Fractures (Similar in Matrix) at Three Drift-Wall Locations and in the Waste Package
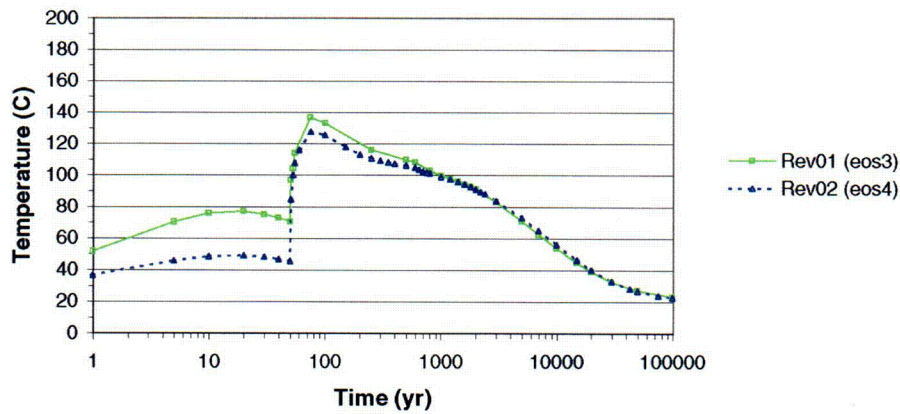
c57

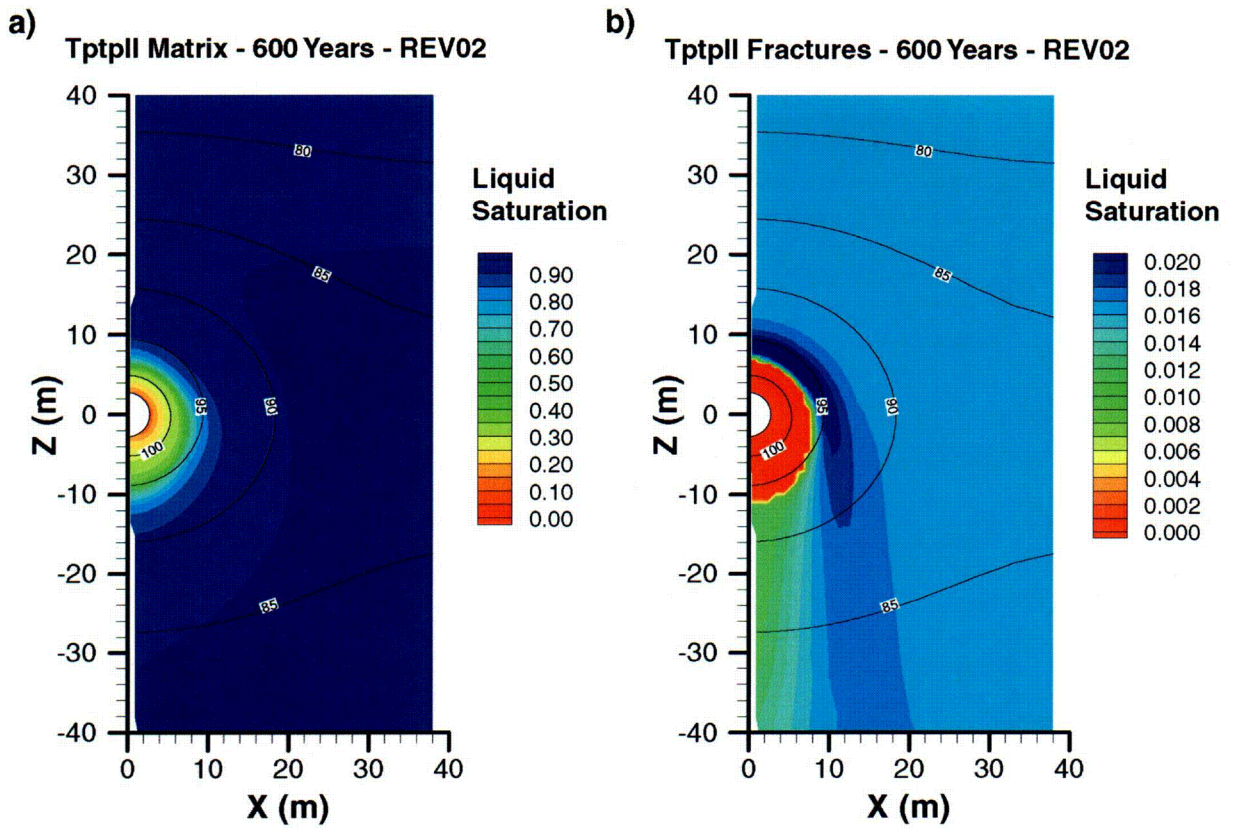## Fractures (Tptpll - Rev01 vs Rev02)

Crown
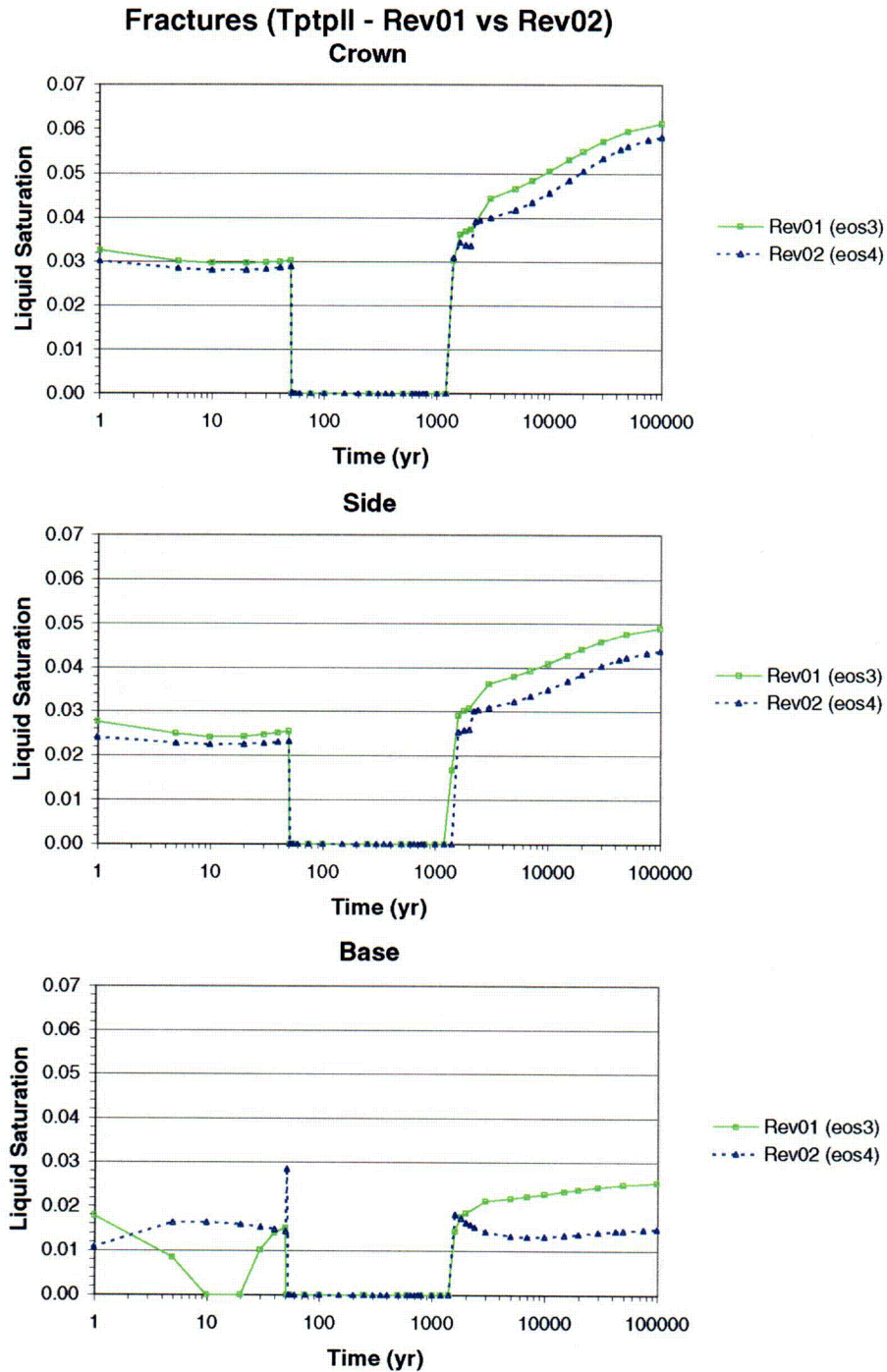

Side

Base

Output-DTN (REV02): LB0307DSTTHCR2.002
DTN (REV01): LB0011DSTTHCR1.001 [154759]

Figure 6.8-5. TH Simulation (Tptpll, REV01 vs. REV02): Time Profiles of Modeled Temperatures in Fractures at Three Drift-Wall Locations

C58

a)

TptpII Matrix - 600 Years - REV02

b)

TptpII Fractures - 600 Years - REV02

Output-DTN: LB0307DSTTHCR2.001

NOTE: Rewetting of the matrix at the drift wall has already occurred (See Figure 6.8-8).

Figure 6.8-6. TH Simulation (TptpII, REV02): Contour Plot of Modeled Temperatures (°C) and Liquid Saturations in the Matrix and Fractures at 600 Years (Near the Time of Maximum Dryout in Fractures)

C59

Fractures (Tptpll - Rev01 vs Rev02)

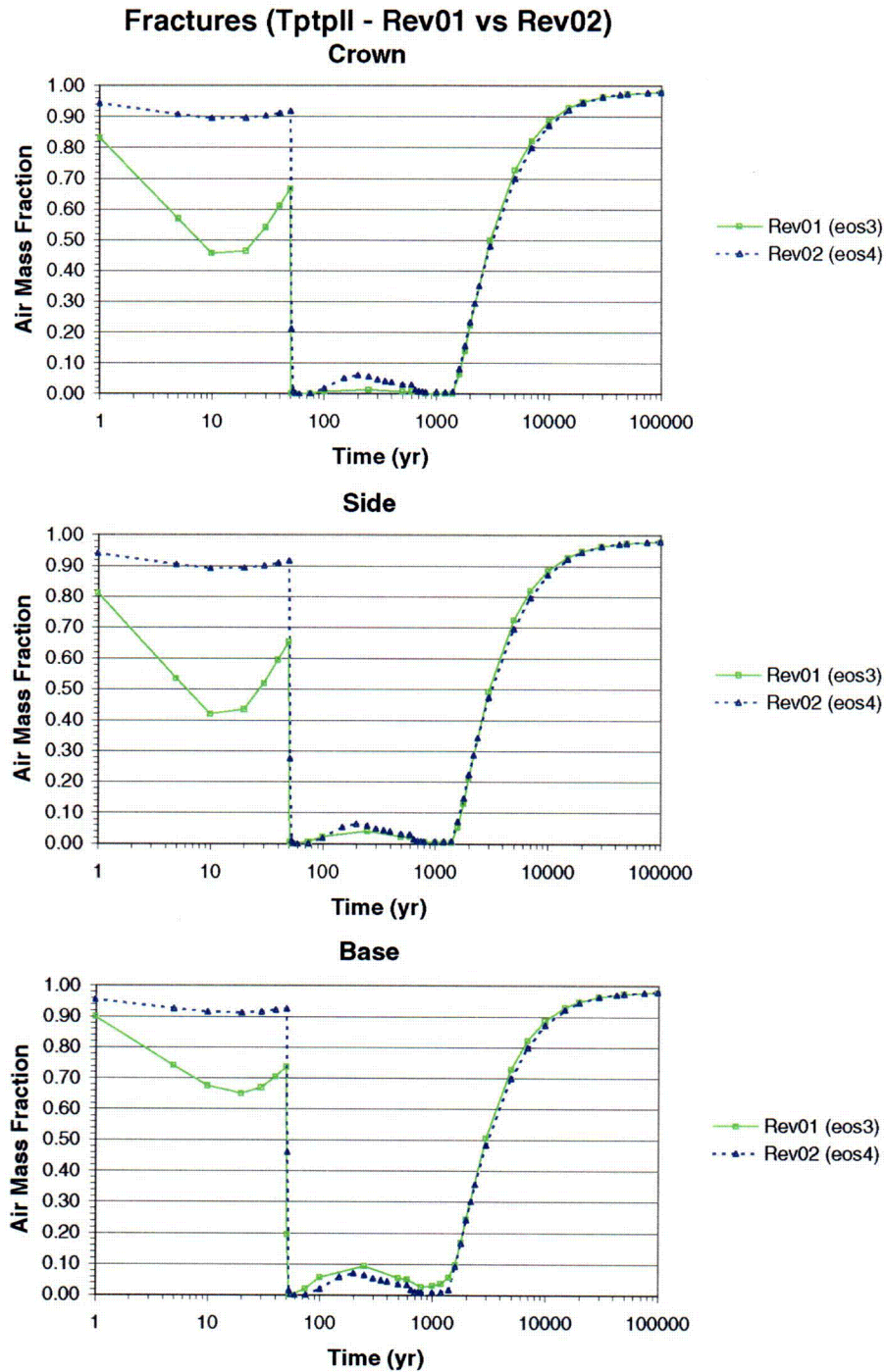Output-DTN (REV02): LB0307DSTTHCR2.002
DTN (REV01): LB0011DSTTHCR1.001 [154759]

Figure 6.8-7. TH Simulation (Tptpll, REV01 vs. REV02): Time Profiles of Modeled Liquid Saturations in Fractures at Three Drift-Wall Locations

c60

Matrix (Tptpll - Rev01 vs Rev02)
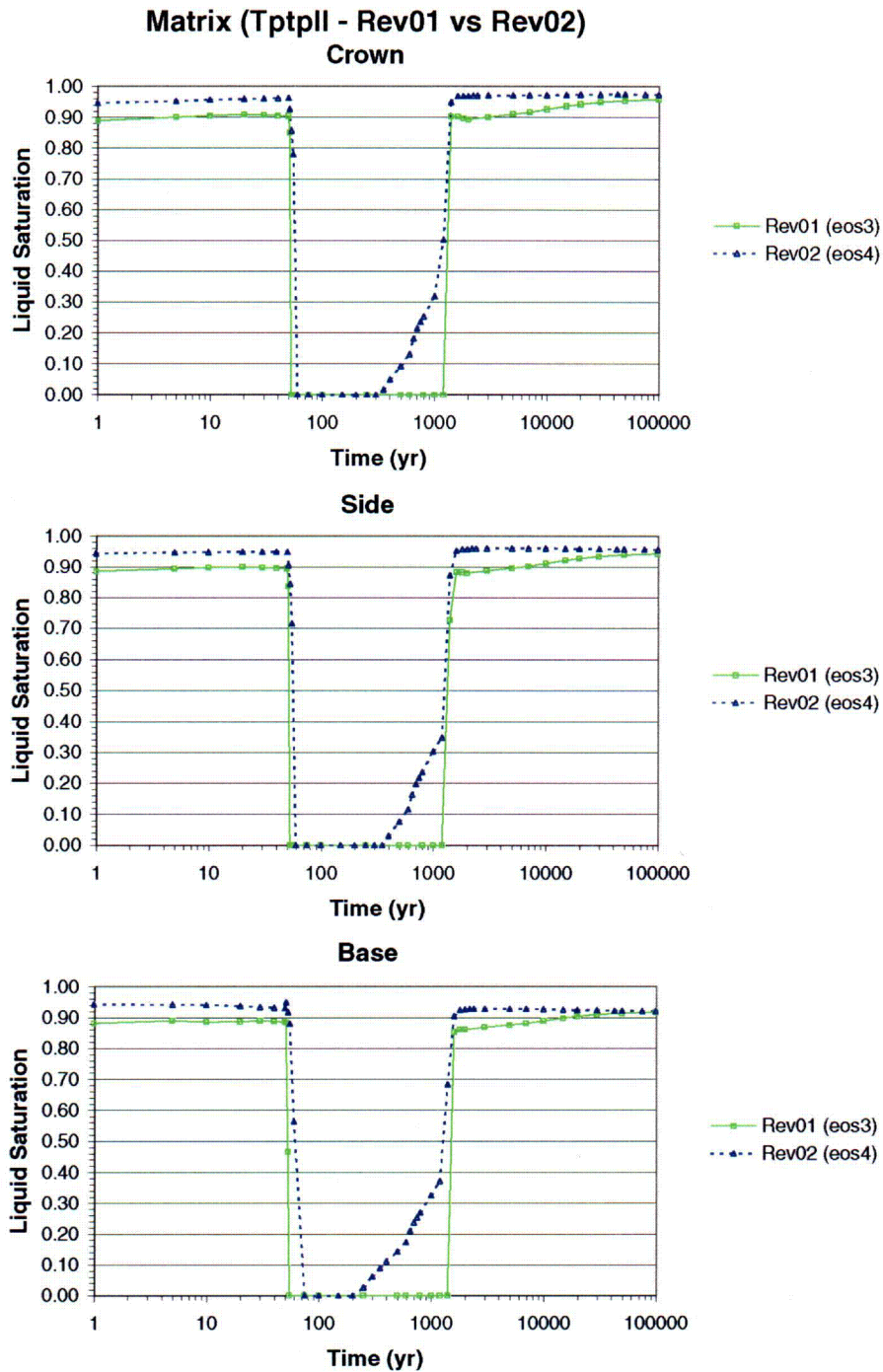
Output-DTN (REV02): LB0307DSTTHCR2.002
DTN (REV01): LB0011DSTTHCR1.001 [154759]

Figure 6.8-8. TH Simulation (Tptpll, REV01 vs. REV02): Time Profiles of Modeled Liquid Saturations in Matrix at Three Drift-Wall Locations

CG1

Figure 6.8-9. TH Simulation (Tptpll, REV01 vs. REV02): Time Profiles of Modeled Air Mass Fractions in the Gas Phase in Fractures at Three Drift-Wall Locations

Fractures (TptplI - REV01 vs REV02)
Crown

Output-DTN (REV02): LB0307DSTTHCR2.002
DTN (REV01): LB0011DSTTHCR1.001 [154759]
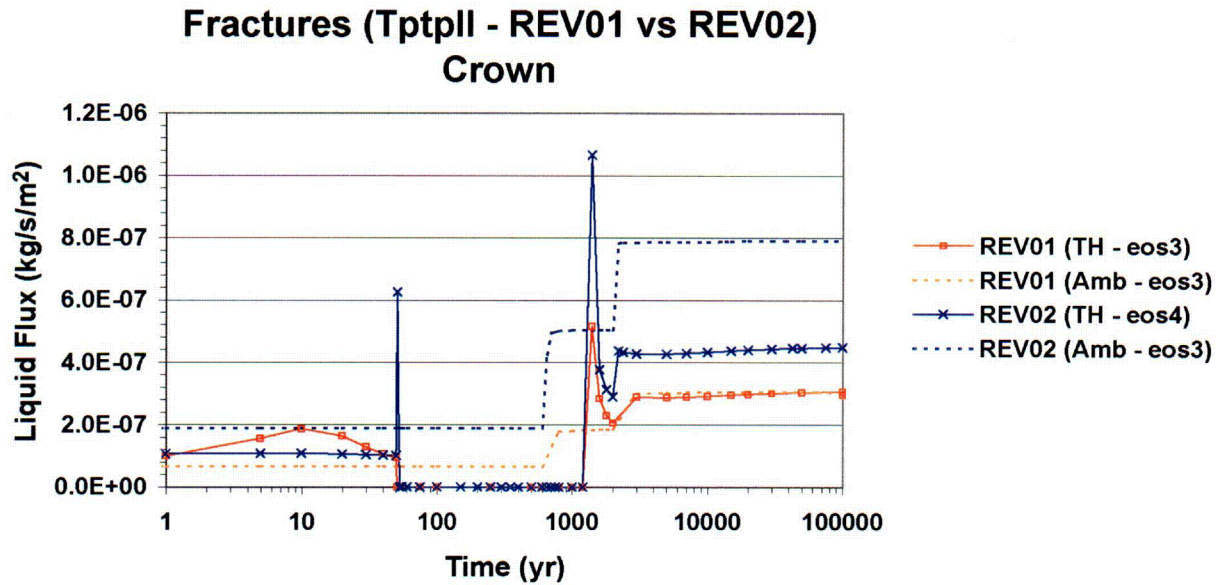
NOTE: Note that REV01 ambient simulations include the drift opening, whereas REV02 ambient simulations do not
        (See text).

Figure 6.8-10.   TH Simulation (TptplI, REV01 vs. REV02): Time Profiles of Modeled Water Flux at the
                 Drift Crown

6.8.5.3   Water Chemistry Trends

6.8.5.3.1   Drift Wall (REV01 versus REV02)

Time profiles similar to those predicted for the REV01 model are discussed below for the same previously selected drift locations: crown (model gridblocks "F 121" and "M 121", side (gridblocks "F 44" and "M 44") and base (gridblocks "F 128" and "M 128") (Figure 6.7-2). As in previous models, these were calculated using the HD-PERM water (W0) as input water composition. The results shown are for an extended-case geochemical system and for cases with and without water vapor pressure lowering caused by capillary pressure (runs referred to as "eos4" and "eos3, respectively). Because these simulations were run with a six-fold increase in the CO_2 diffusion coefficient compared to earlier models (Section 6.8.3), model results are also presented for another eos4 THC simulation considering the same CO_2 diffusion coefficient as earlier runs.

Predicted time profiles of temperature, CO_2 gas concentrations, and aqueous species total concentrations (fracture medium) are shown in Figures 6.8-11 through 6.8-20. They are directly comparable to profiles presented in Section 6.7 for the REV01 model. Predicted trends in fracture gas and water chemistry through time remain generally the same as in REV01. The processes driving these trends are discussed in Sections 6.5.5 and 6.7.5 and are not repeated here.

Postclosure temperature profiles from THC simulations (Figure 6.8-11) are similar for model runs with and without vapor-pressure lowering, but with slightly higher peak temperatures

C63

predicted with the latter. These profiles also indicate that the principal cause for the difference in peak temperatures between the REV01 and REV02 model is not the selected water vapor pressure models, but the change in rock properties from REV01 to REV02.

With respect to predicted water and gas chemistry trends at the drift wall, the most noticeable difference between this model revision and REV01 is the trend of calculated CO_2 concentrations (Figure 6.8-12). Although generally similar, the rise in CO_2 concentrations above ambient values occurs much earlier in the current model (starting at around 600 years instead of 2,000 years in REV01). This earlier rise, as well as subsequently higher predicted CO_2 concentrations, is observed in simulations both with and without vapor pressure lowering (Figure 6.8-12). These effects are attributed mostly to the effect of opening the drift wall to gas advection (the drift was closed to such fluxes in earlier model revisions). The simulation with a lower CO_2 diffusion coefficient consistent with the value used in REV01 also predicts that the CO_2 concentrations will start rising earlier and rising to higher values than in previous models (Figure 6.8-12). The increase in the CO_2 diffusion coefficient (six fold here) causes somewhat higher predicted CO_2 concentrations in the gas phase, although the effect is most noticeable during early stages of the dryout period (Figure 6.8-12). In all cases, the predicted CO_2 concentrations at the drift wall remain below 10,000 ppmv for the entire simulated time period. As noted in earlier models, CO_2 concentrations drop quickly at the onset of dryout, shortly after 50 years, because of displacement by steam. Fluctuations during the dryout period (Figure 6.8-12) appear to result from the competing effect of CO_2 displacement by steam (from the drift outwards), and increased diffusion of CO_2 towards the drift resulting from rising temperatures after all water boils out.

The predicted pH values in fracture water (Figure 6.8-13) are consistent with modeled trends of CO_2 concentrations. Compared to earlier simulations, the lower temperatures during preclosure (due to higher heat removal efficiency) yield lower CO_2 partial pressures and thus higher pH values (generally by less than a half unit). After closure, the higher predicted CO_2 concentrations yield lower pH values (mostly by less than a half unit). The choice of the water-vapor pressure model and the difference in the CO_2 diffusion coefficient have only a small effect on predicted pH values (differences mostly within less than 0.2 pH units; Figure 6.8-13). The predicted pH range of water in fractures at the drift wall for all cases is neutral to slightly alkaline (pH 7 to 8.6) and remains essentially below predicted ambient values (8.2–8.6) for the entire simulated time period. The total carbonate concentrations (shown as HCO_3^- on Figure 6.8-14) are depressed, relative to ambient values, because of the exsolution of CO_2 gas driven by elevated temperatures.

The predicted time profiles for other constituents (Figures 6.8-15 through 6.8-20) do not show much sensitivity to the choice of water-vapor pressure model or the CO_2 diffusion coefficient. In most cases, elevated concentrations are predicted at the time the drift rewets, followed by a steep fall towards ambient values (e.g. Figure 6.8-18). As noted earlier, these temporarily elevated concentrations are caused by the rewetting of areas where evaporative concentration took place during dryout. The precipitation of salts upon complete dryout is accounted for in this model (it was not in previous model revisions), and the dissolution of these salts upon rewetting causes higher concentration peaks of dissolved constituents than predicted previously. Nevertheless, these relatively elevated concentrations are predicted only at small liquid saturations at which no significant fluid flow could occur. The improved treatment of mineral precipitation at the boiling

front also results in the prediction of lower, more realistic aqueous silica concentrations than in earlier models (Figure 6.8-17).

Nitrate is included in the present simulations in contrast to REV01 simulations where it was omitted. Prior to REV02 of this report, other investigators have estimated concentration trends of this anion on the basis of predicted chloride concentration and the NO_3/Cl ratio in the initial water (Figure 6.8-20). Although nitrate is treated as a conservative species, its mass inventory is accounted for upon complete dryout by forming sodium nitrate, using all the available nitrate in solution (without equilibrium calculations; see Section 6.4.5). Upon rewetting, it dissolves faster than chlorides because of its greater solubility, causing a temporary increase in the NO_3/Cl ratio of rewetting waters. However, this effect is barely noticeable (Figure 6.8-21).
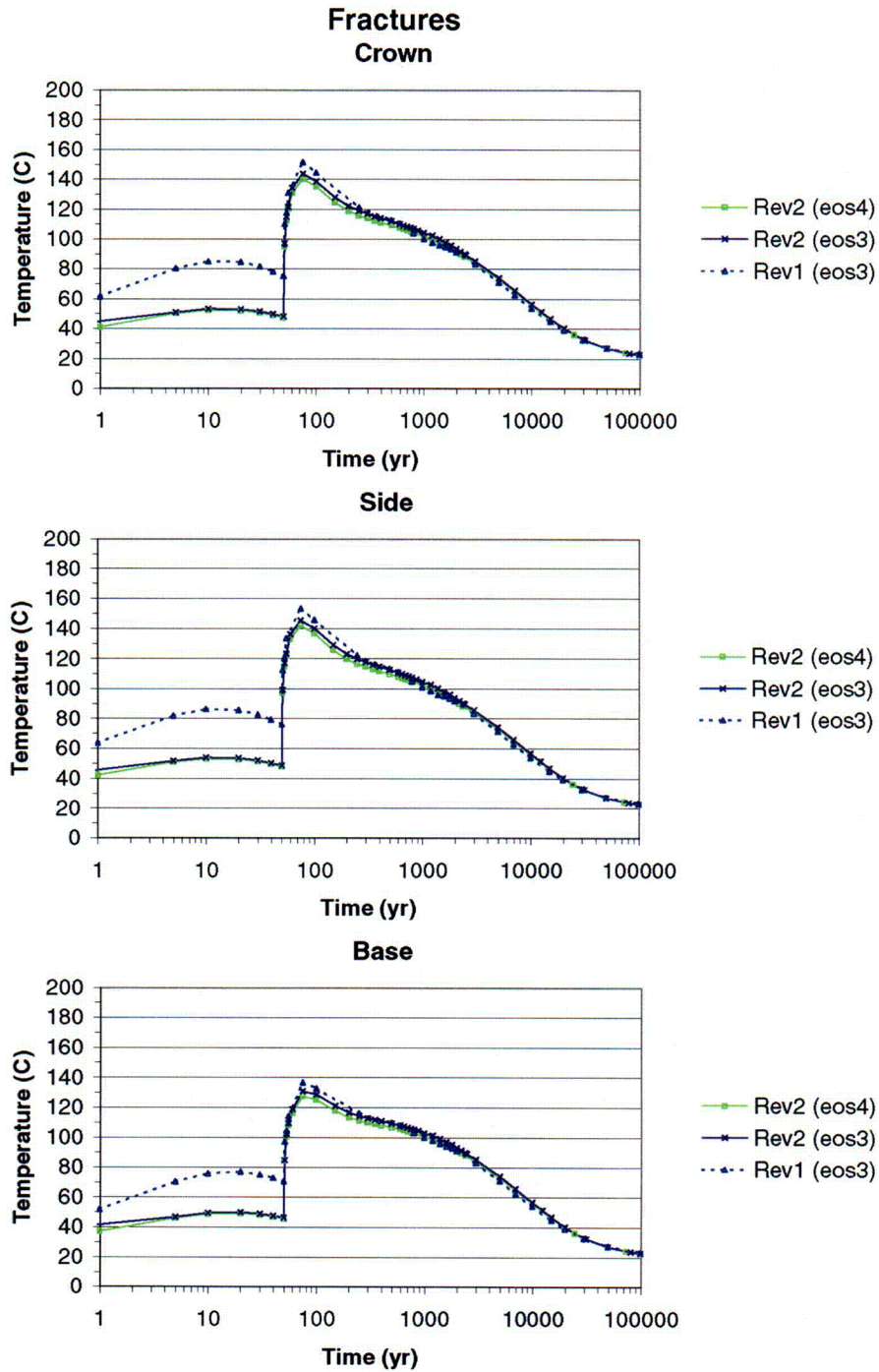
Fractures
Crown

Side

Base

Output-DTNs (REV02): LB0302DSCPTHCS.002, LB0307DSTTHCR2.002
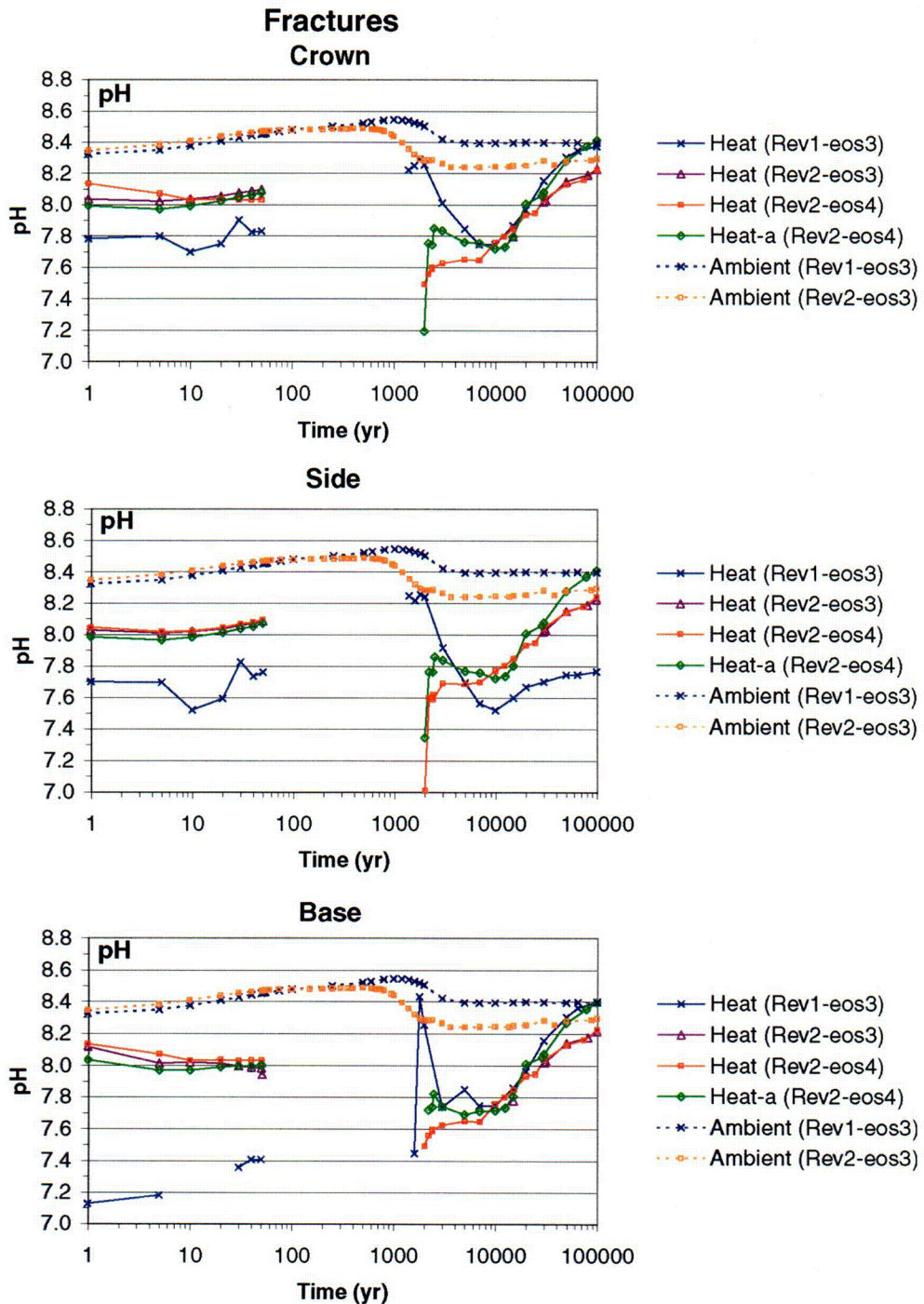DTN (REV01): LB0011DSTTHCR1.001 [154759]

Figure 6.8-11. THC Simulation (Tptpll, REV01 vs. REV02): Time Profiles of Modeled Temperatures at Three Drift-Wall Locations With and Without Water-Vapor-Pressure Lowering (eos4 and eos3, respectively)
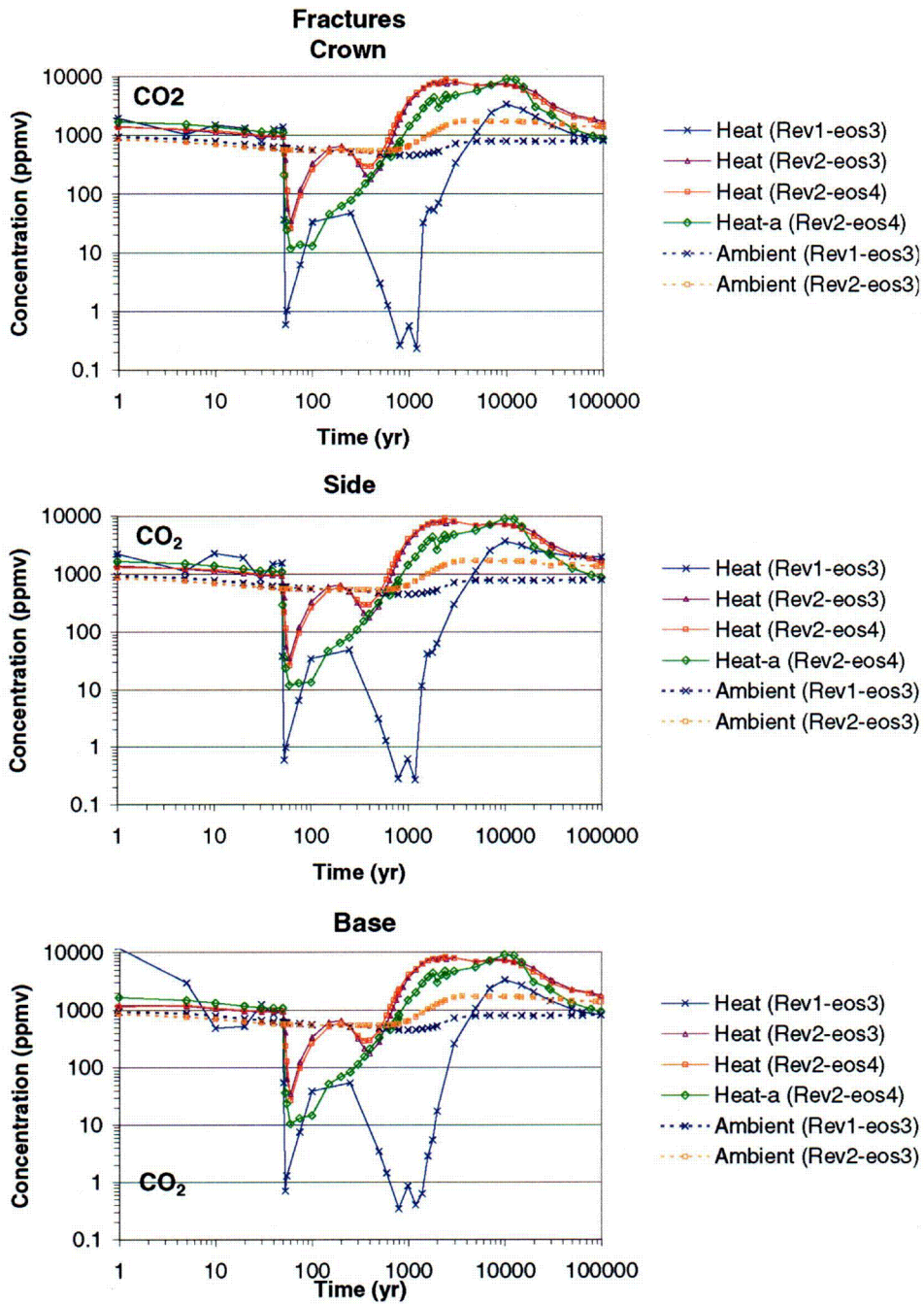
Fractures
Crown

Side

Base

Output-DTNs (REV02): LB0302DSCPTHCS.002, LB0307DSTTHCR2.002
DTN (REV01): LB0011DSTTHCR1.001 [154759]

NOTE: REV01 Simulations and the REV02 Simulation Labeled "Heat-a" were run with the CO_2 diffusion coefficient six times smaller than other simulations (see text).

Figure 6.8-12. THC Simulation (Tptpll, REV01 vs. REV02): Time Profiles of Modeled CO_2 Concentrations in the Gas Phase in Fractures at Three Drift-wall Locations under Heating (Heat) and Non-Heating (Ambient) Conditions, Including (eos4) and Excluding (eos3) Water-Vapor-Pressure Lowering

C65

Fractures

Crown

Side

Base

Output-DTNs (REV02): LB0302DSCPTHCS.002, LB0307DSTTHCR2.002
DTN (REV01): LB0011DSTTHCR1.001 [154759]

NOTE: REV01 Simulations and the REV02 Simulation Labeled "Heat-a" were run with the CO_2 diffusion coefficient six times smaller than other simulations (see text).

Figure 6.8-13. THC Simulation (Tptpll, REV01 vs. REV02): Time Profiles of the Modeled pH of Fracture Water at Three Drift-Wall Locations under Heating (Heat) and Non-Heating (Ambient) Conditions, Including (eos4) and Excluding (eos3) Water-Vapor-Pressure Lowering

CGG
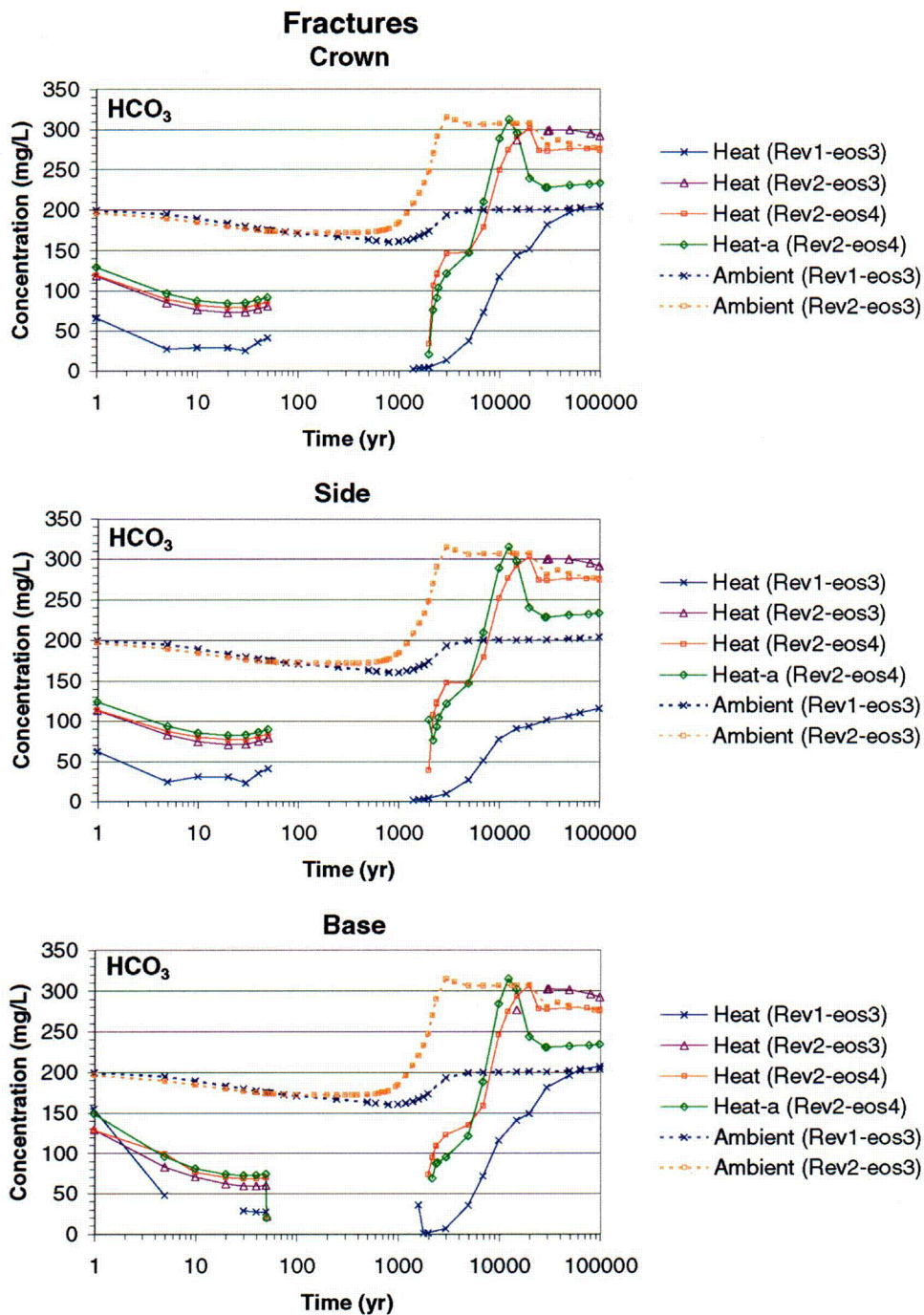
Fractures
Crown

Side

Base

Output-DTNs (REV02): LB0302DSCPTHCS.002, LB0307DSTTHCR2.002
DTN (REV01): LB0011DSTTHCR1.001 [154759]

NOTE: REV01 Simulations and the REV02 Simulation Labeled "Heat-a" were run with the CO_2 diffusion coefficient six times smaller than other simulations (see text).

Figure 6.8-14.   THC Simulation (Tptpll, REV01 vs. REV02): Time Profiles of Modeled Total Aqueous Carbonate Concentrations (as HCO_3^-) in Fracture Water at Three Drift-Wall Locations, under Heating (Heat) and Non-Heating (Ambient) Conditions, Including (eos4) and Excluding (eos3) Water-Vapor-Pressure Lowering

C67

Fractures
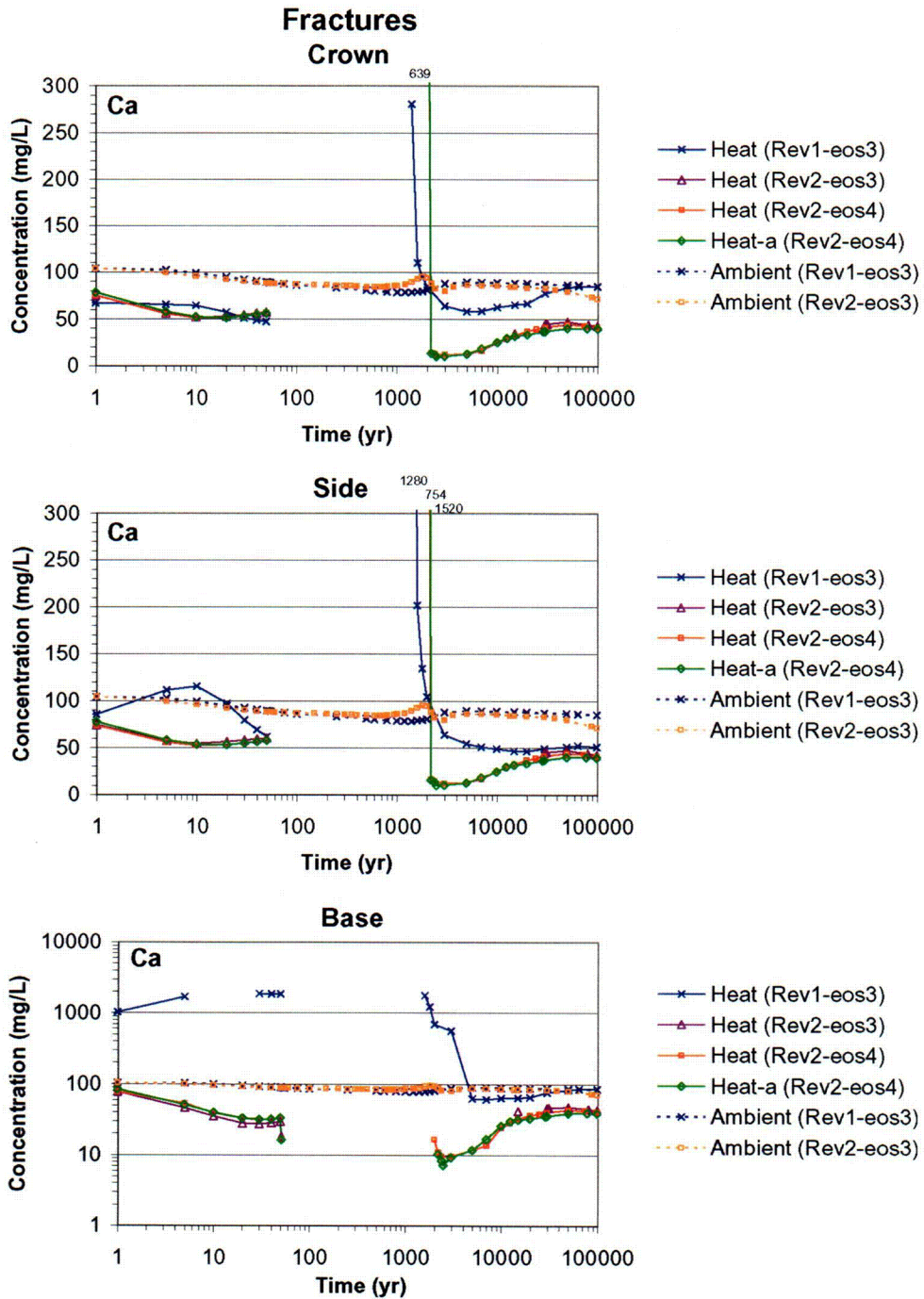
Crown

Side

Base

Output-DTNs (REV02): LB0302DSCPTHCS.002, LB0307DSTTHCR2.002
DTN (REV01): LB0011DSTTHCR1.001 [154759]

NOTE: REV01 Simulations and the REV02 Simulation Labeled "Heat-a" were run with the CO_2 diffusion coefficient six times smaller than other simulations (see text).

Figure 6.8-15.   THC Simulation (Tptpll, REV01 vs. REV02): Time Profiles of Modeled Total Aqueous Calcium Concentrations in Fracture Water at Three Drift-Wall Locations, under Heating (Heat) and Non-Heating (Ambient) Conditions, Including (eos4) and Excluding (eos3) Water-Vapor-Pressure Lowering
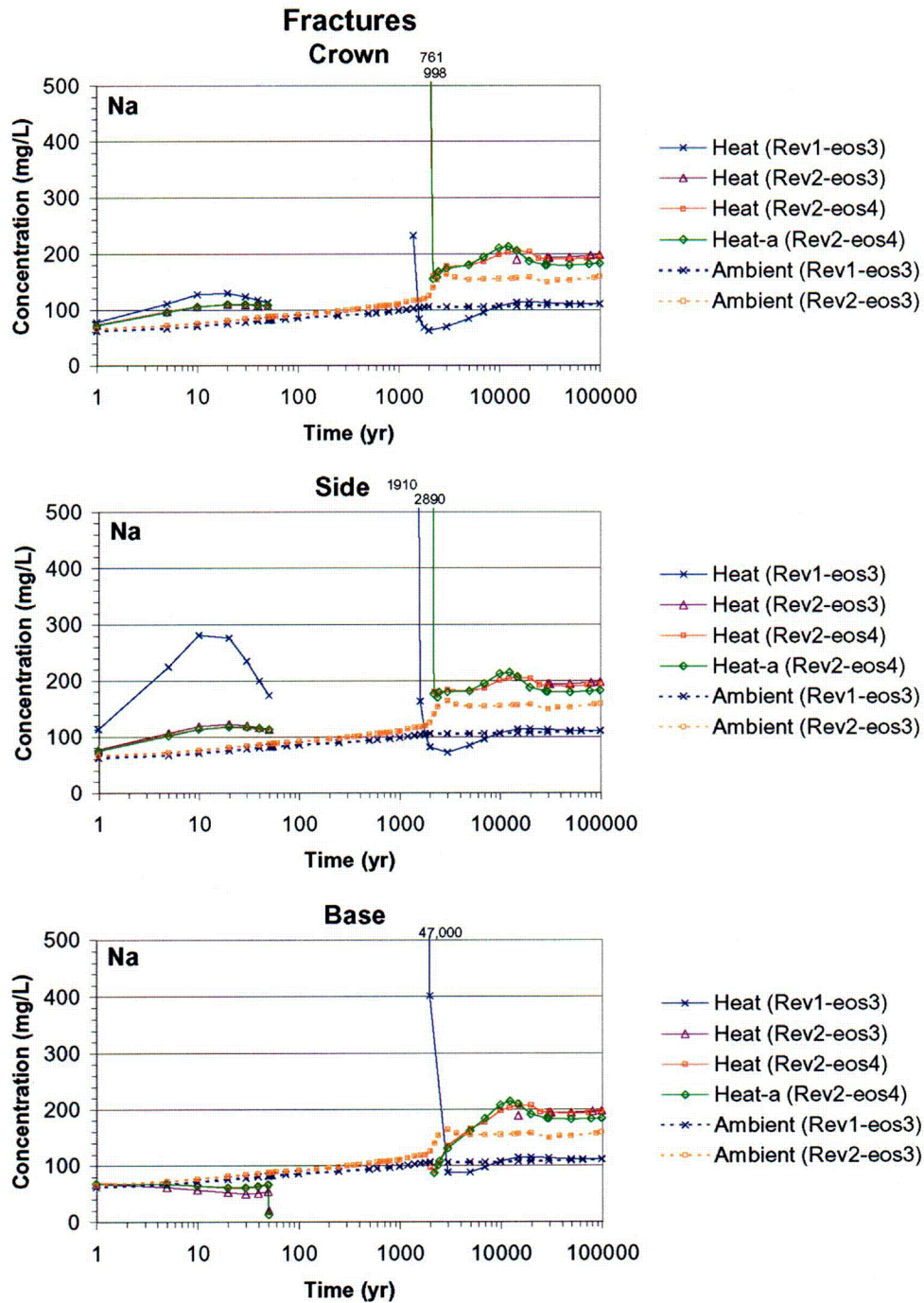
C68

Output-DTNs (REV02): LB0302DSCPTHCS.002, LB0307DSTTHCR2.002
DTN (REV01): LB0011DSTTHCR1.001 [154759]

NOTE: REV01 Simulations and the REV02 Simulation Labeled "Heat-a" were run with the CO_2 diffusion coefficient six times smaller than other simulations (see text).

Figure 6.8-16.   THC Simulation (Tptpll, REV01 vs. REV02): Time Profiles of Modeled Total Aqueous Sodium Concentrations in Fracture Water at Three Drift-Wall Locations, under Heating (Heat) and Non-Heating (Ambient) Conditions, Including (eos4) and Excluding (eos3) Water-Vapor-Pressure Lowering
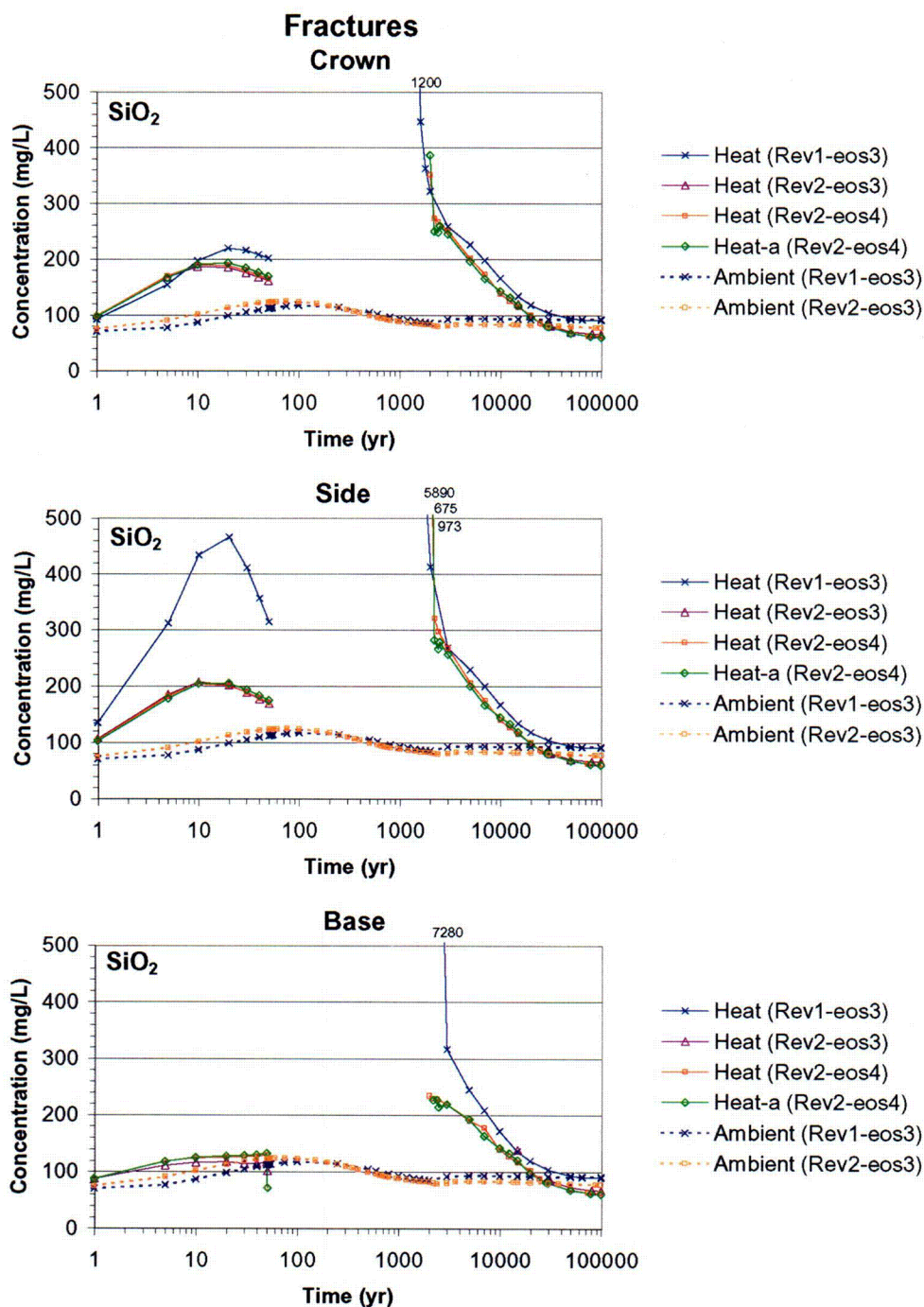
Fractures

Output-DTNs (REV02): LB0302DSCPTHCS.002, LB0307DSTTHCR2.002
DTN (REV01): LB0011DSTTHCR1.001 [154759]

NOTE: REV01 Simulations and the REV02 Simulation Labeled "Heat-a" were run with the CO_2 diffusion coefficient six times smaller than other simulations (see text).

Figure 6.8-17.   THC Simulation (Tptpll, REV01 vs. REV02): Time Profiles of Modeled Total Aqueous Silica Concentrations in Fracture Water at Three Drift-Wall Locations, under Heating (Heat) and Non-Heating (Ambient) Conditions, Including (eos4) and Excluding (eos3) Water-Vapor-Pressure Lowering

C70

Fractures
Crown

Side

Base

Output-DTNs (REV02): LB0302DSCPTHCS.002, LB0307DSTTHCR2.002
DTN (REV01): LB0011DSTTHCR1.001 [154759]

NOTE: REV01 Simulations and the REV02 Simulation Labeled "Heat-a" were run with the CO_2 diffusion coefficient six times smaller than other simulations (see text).
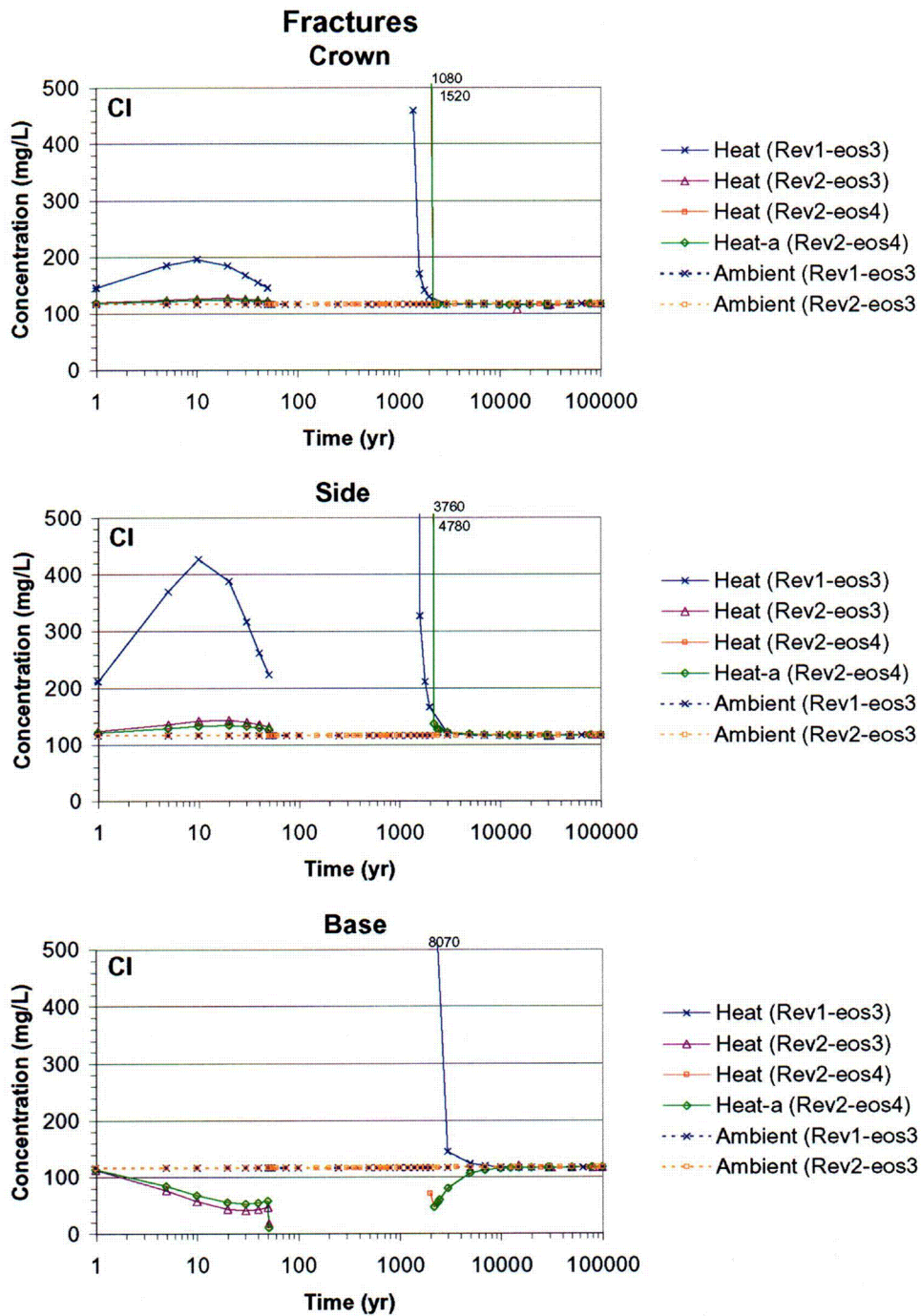
Figure 6.8-18. THC Simulation (Tptpll, REV01 vs. REV02): Time Profiles of Modeled Total Aqueous Chloride Concentrations in Fracture Water at Three Drift-Wall Locations, under Heating (Heat) and Non-Heating (Ambient) Conditions, Including (eos4) and Excluding (eos3) Water-Vapor-Pressure Lowering

Fractures
Crown
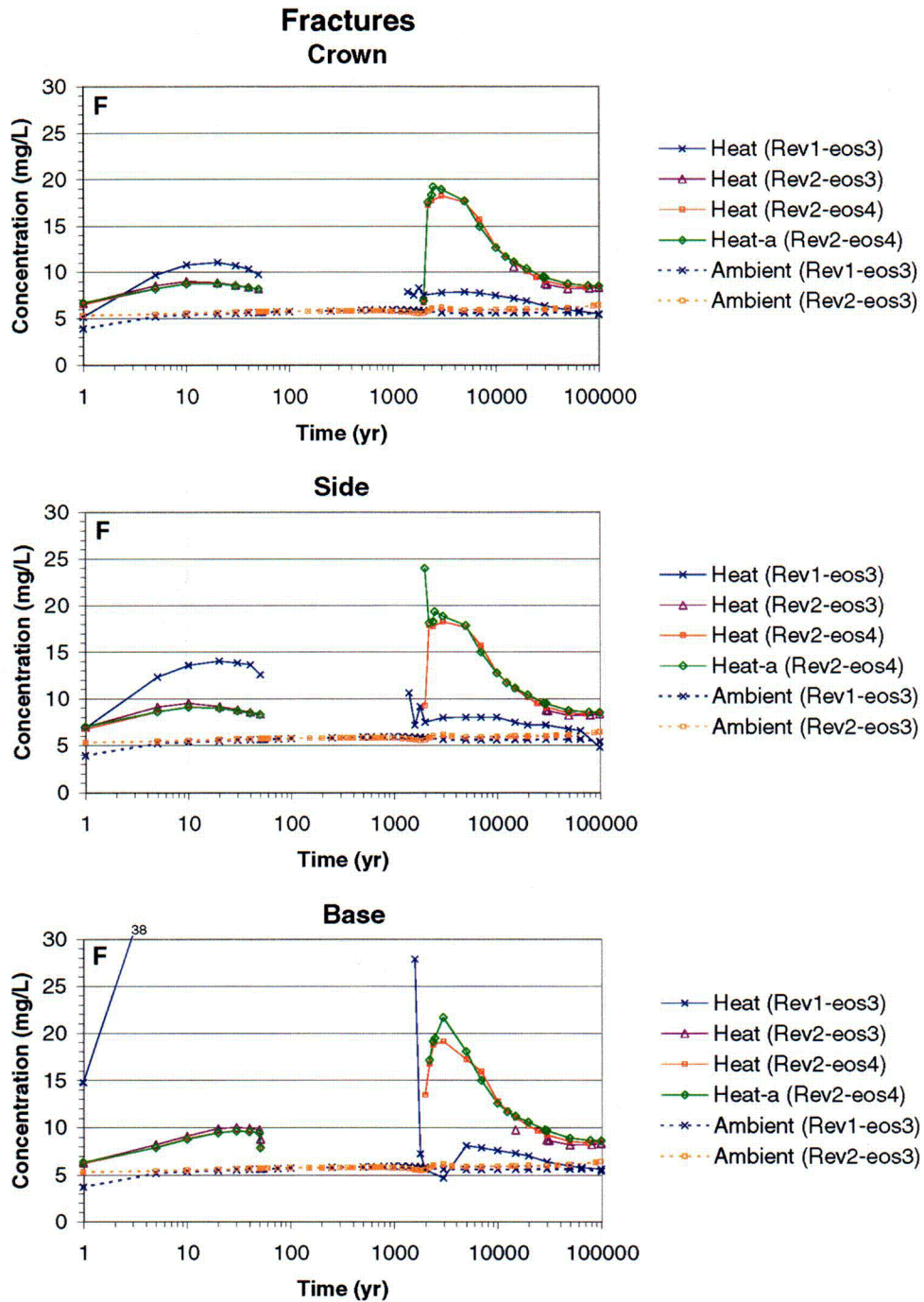

Side

Base

Output-DTNs (REV02): LB0302DSCPTHCS.002, LB0307DSTTHCR2.002
DTN (REV01): LB0011DSTTHCR1.001 [154759]

NOTE: REV01 Simulations and the REV02 Simulation Labeled "Heat-a" were run with the CO_2 diffusion coefficient six times smaller than other simulations (see text).

Figure 6.8-19.   THC Simulation (Tptpll, REV01 vs. REV02): Time Profiles of Modeled Total Fluoride Concentrations in Fracture Water at Three Drift-Wall Locations, under Heating (Heat) and Non-Heating (Ambient) Conditions, Including (eos4) and Excluding (eos3) Water-Vapor-Pressure Lowering

C72

Fractures
Crown
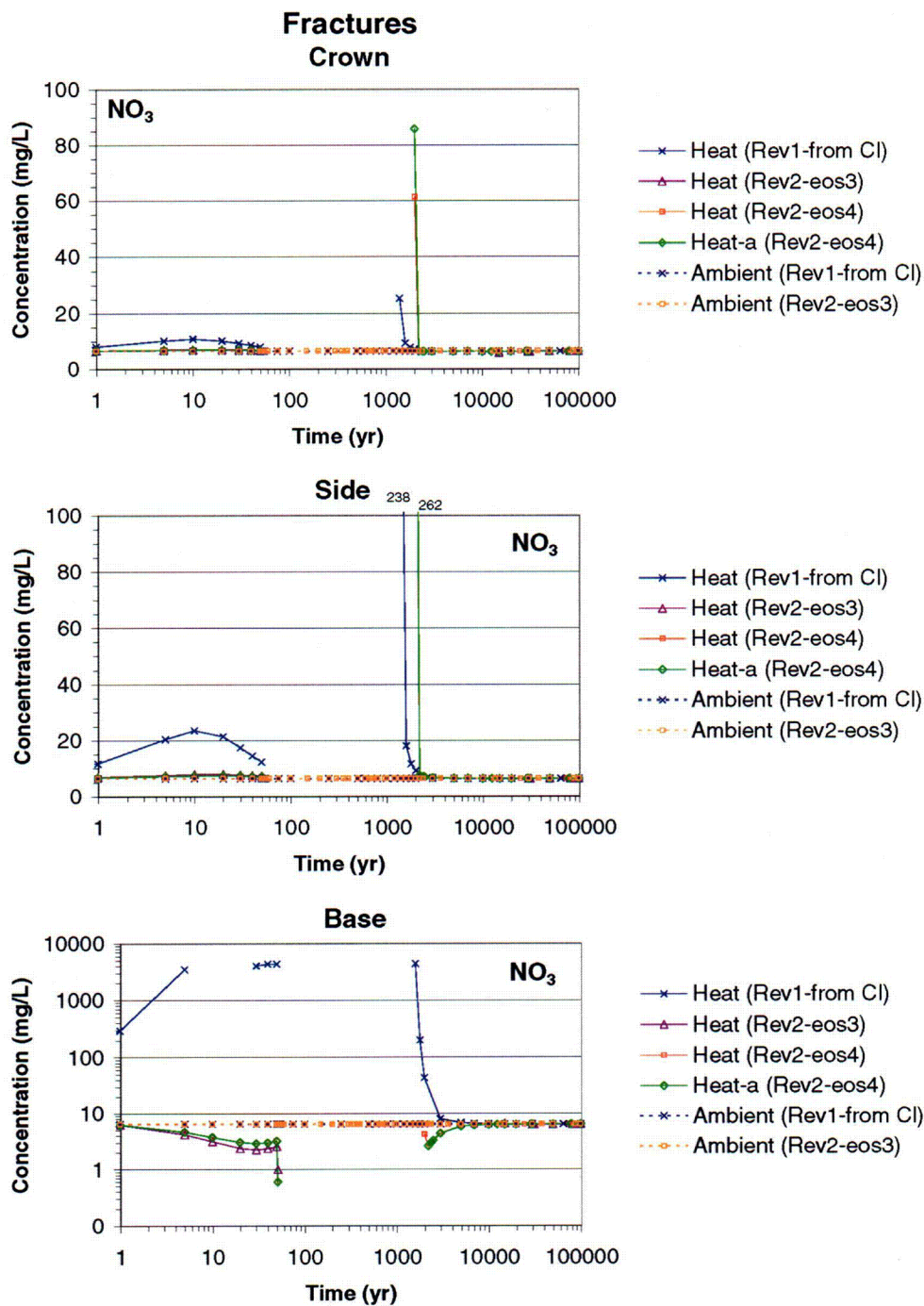

Side

Base

Output-DTNs (REV02): LB0302DSCPTHCS.002, LB0307DSTTHCR2.002
DTN (REV01): LB0011DSTTHCR1.001 [154759]

NOTE: REV01 Simulations and the REV02 Simulation Labeled "Heat-a" were run with the CO_2 diffusion coefficient six times smaller than other simulations (see text).

Figure 6.8-20.   THC Simulation (Tptpll, REV01 vs. REV02): Time Profiles of Modeled Total Nitrate Concentrations in Fracture Water at Three Drift-Wall Locations, under Heating (Heat) and Non-Heating (Ambient) Conditions, Including (eos4) and Excluding (eos3) Water-Vapor-Pressure Lowering

Fractures
Crown

Side

Base

Output-DTNs (REV01): LB0302DSCPTHCS.002, LB0307DSTTHCR2.002
DTN (REV01): LB0011DSTTHCR1.001 [154759]

NOTE: REV01 Simulations and the REV02 Simulation Labeled "Heat-a" were run with the CO_2 diffusion coefficient six times smaller than other simulations (see text).
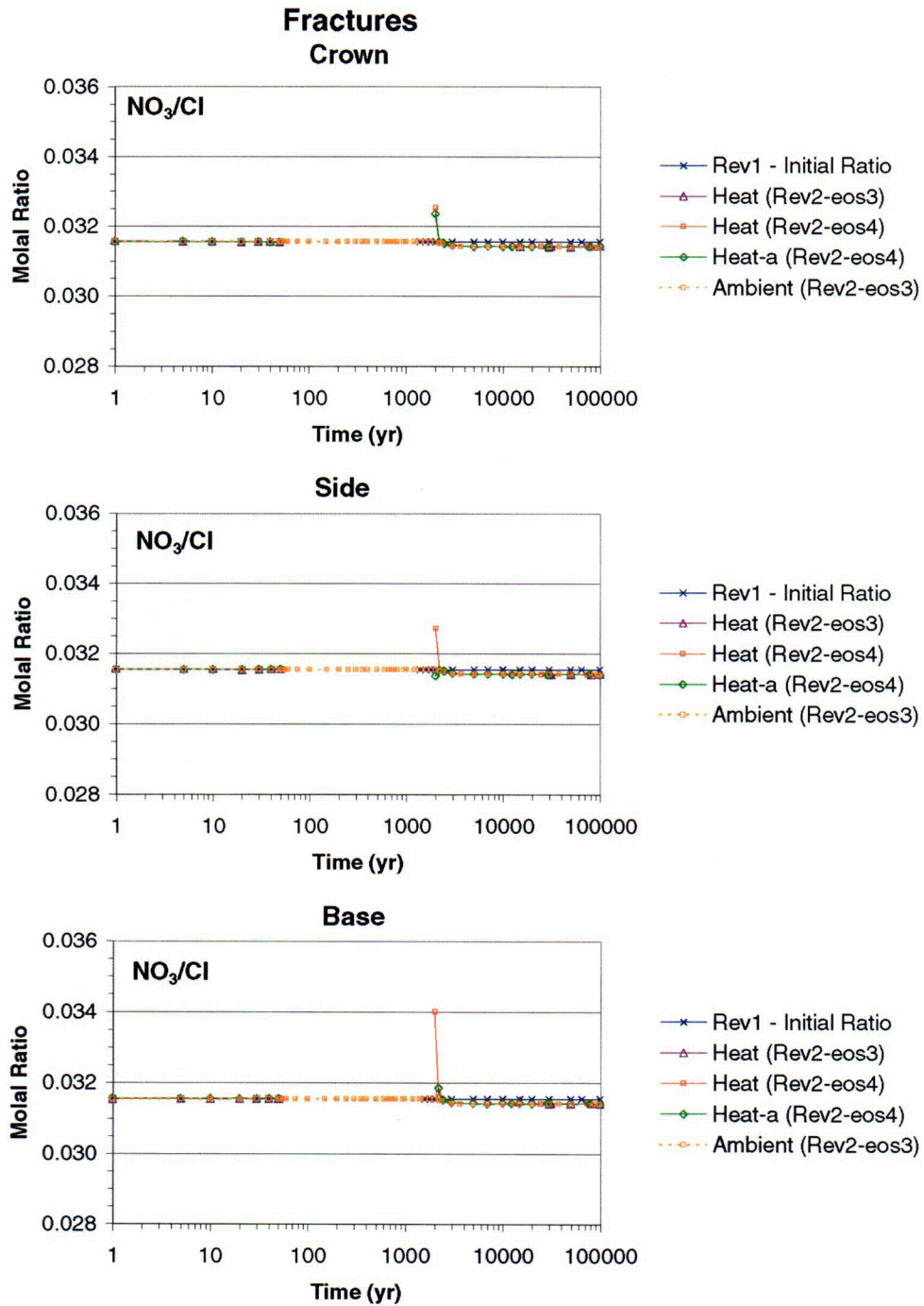
Figure 6.8-21. THC Simulation (Tptpll, REV01 vs. REV02): Time Profiles of Modeled Total Nitrate to Chloride Ratio at Three Drift-Wall Locations, under Heating (Heat) and Non-Heating (Ambient) Conditions, Including (eos4) and Excluding (eos3) Water-Vapor-Pressure Lowering

C74

6.8.5.3.2 "High"-Liquid Saturation Zone Above Drift Crown (Tptpll REV02)

As reported in previous sections of this report, predicted concentration profiles at fixed model gridblocks at the crown, side, and base of the drift provide only limited information on the chemistry of waters that could seep into drifts. Such profiles do not fully capture the spatial variability of model results around the drift and, more importantly, cannot show water compositions as long as the selected model gridblocks remain dry. To complement results shown in previous sections and to better capture spatial variability, as well as predicted water compositions during the dryout period, concentration time-profiles were also generated for dynamic zones following the expanding, then receding, boiling and condensation fronts around the drift. Most of the model results extracted in this way (using CUTCHEM V1.0 (LBNL 2002 [161127])) will be presented in the upcoming revision of *Abstraction of Drift-Scale Coupled Processes* (CRWMS M&O 2000 [123916]). Here, some of these results are presented for gridblocks with highest liquid saturation above the drift in fractures. More specifically, data were extracted for model gridblocks located within a 45-degree arc from the drift crown down, and for the first six of such gridblocks having the highest liquid saturation in fractures, within 25 m from drift centerline.

Various time profiles are shown below for data extracted in this manner (thus, data for six gridblocks are plotted per point in time for each run). To assess the model sensitivity to initial water compositions and other alternative conceptualizations, time profiles were generated for simulations considering:

- The five different input initial water compositions described in Section 6.2.2.1: W0, the composition used so far (HD-PERM), and alternative compositions W4 through W7

- Three different infiltration scenarios (using the HD-PERM input water composition): stepwise increase from 6 to 25 mm/yr, fixed 6 mm/yr, and fixed 25 mm/yr (Table 6.8-2)

- The two different water vapor-pressure models implemented in TOUGHREACT V3.0 (LBNL 2002 [161256] modules EOS4 and EOS3 (using the HD-PERM input water composition): with and without vapor-pressure lowering due to capillary pressure.

Therefore, time profiles generated in this way capture a spread of concentrations related to (1) the natural variability of input water compositions, (2) alternative model conceptualizations, and (3) for each model run at any given time, the spatial variability of model results for gridblocks of highest liquid saturation above the drift crown. In addition to this spread, fluctuations of computed concentrations with time arising from THC effects (as discussed below) are also captured.

The distance from drift center, temperature, and liquid saturation in model gridblocks having the highest liquid saturation (above the drift) picked up by the extraction procedure (using CUTCHEM V1.0 (LBNL 2002 [161127]) are shown in Figures 6.8-22, 6.8-23, and 6.8-24, respectively (these figures exclude a few points extracted at times around 50 years and located approximately 24 m away from the drift center). These data provide a context for the chemistry profiles discussed below. For simulated times up to 50 years, all data are from zones directly above, and adjacent to, the drift crown (i.e., at a distance approximately 2.8 m from drift center)

(Figure 6.8.22). From the onset of boiling at approximately 50 years, high-liquid-saturation gridblocks are all from the condensation (reflux) zone above the drift. Later, after the collapse of the boiling front, gridblocks with the highest liquid saturation are located either directly adjacent to the drift crown (e.g., some of the W0 data on Figure 6.8-22) or further away, adjacent to zones of reduced permeability formed by prior mineral deposition at the boiling front. These zones are discussed in Section 6.8.5.4.

After the onset of boiling, starting at approximately 50 years, the temperature in the most highly liquid-saturated gridblocks remains nearly constant (near 96°C, the boiling point for the modeled elevation), as would be expected in the zone of condensation and reflux (Figure 6.8-23). For most runs, the boiling temperature in these gridblocks is maintained until around 1,000 years. The boiling front is predicted to collapse a few hundred years earlier for the case with the higher constant infiltration rate of 25 mm/yr (Figure 6.8-23). This period of time, during which temperatures are maintained at the boiling point of water, is hereafter referred to as the "boiling period." Temperature profiles predicted with the various runs are quite similar, except for the shorter boiling period at higher infiltration. The greatest predicted temperature difference between simulations (around 5°C) is also caused by differences in infiltration rate.

For a given run, and at a given time, predicted liquid saturations in the first six gridblocks with highest liquid saturation (above the drift) are fairly uniform (Figure 6.8-24), because these data represent areas of highest liquid saturation in a laterally homogenous model. Consequently, corresponding concentration time-profiles (Figures 6.8-25 through 6.8-38), for each run at any given time, also show less spatial variability than would evaporated waters from gridblocks with much smaller and variable liquid saturations (such as at the boiling front). Therefore, examining the variability of predicted water compositions in zones of highest liquid saturation provides a better means of evaluating the model sensitivity to various input data or model conceptualizations than would examination of predicted water compositions directly at the boiling front. This is the main reason for focusing on zones of highest liquid saturation. However, when evaluating the compositional variability of waters that could seep into a drift during the boiling period (by somehow penetrating the dryout zone), the predicted water composition at the boiling front should also be considered. This variability will be assessed in the upcoming revision of *Abstraction of Drift-Scale Coupled Processes* (CRWMS M&O 2000 [123916]).

Predicted profiles of concentration versus time for CO_2 gas and aqueous species of interest are shown in Figures 6.8-25 through 6.8-38. Three observations are particularly significant:

(1) In general, these figures indicate that the different input water compositions (i.e., natural variability) produce a larger relative spread in predicted water and gas compositions than the range of infiltration rates considered or the selected water-vapor pressure module;

(2) At any one point, the relative spread of predicted concentrations for the various modeled alternatives (at those gridblocks with highest liquid saturation above the drift crown) generally does not exceed an order of magnitude and is often much less (see Section 6.9-2; details will also be provided in upcoming revision of *Abstraction of Drift-Scale Coupled Processes* (CRWMS M&O 2000 [123916]));

(3) Finally, for all simulations shown, the predicted general concentration trends are quite similar.

The modeled CO_2 concentrations in zones of condensation and reflux (Figure 6.8-25) are initially higher than at drift wall locations shown previously, because heat mobilizes CO_2 outwards from the drift wall (see also Section 7.1). However, CO_2 concentrations eventually also decrease in the reflux/condensation zone because of continued depletion of aqueous carbonate (Figure 6.8-27) from CO_2 exsolution and calcite precipitation (see below). The subsequent trend of rising CO_2 concentration (from approximately 600 to 2,000 years) (Figure 6.8-25) was also noted earlier for locations at the drift wall (Figure 6.8-12). Note that during this time period, when the CO_2 concentrations are rising (from approximately 600 to 2000 years), the spread of these concentrations is sharply reduced compared to the spread during other simulated time intervals (Figure 6.8-25a). This appears to be caused by the arrival of percolating water with a significantly higher dissolved CO_2 content than the locally decarbonated water. This temporarily higher dissolved CO_2 content in percolation water results from prior mobilization of CO_2 gas from matrix water into fractures, further up the stratigraphic column. The case with a decrease in CO_2 diffusion coefficient (Figure 6.8-25b) shows a similar rise but occurring at a somewhat delayed time, due to the decreased diffusive mobility. The decreasing pH values from approximately 600 to 2000 years (Figure 6.8-26) is also consistent with the arrival of more carbonated water from prior CO_2 gas mobilization. After approximately 2000 years, the spread in concentrations increases again as these concentrations become less driven by the mobilization of CO_2 and more by water-rock interactions that are more sensitive to the composition of infiltration water (even though all waters are set with the same CO_2 partial pressure at the top model boundary). Also, the increase in infiltration rate at 2000 years exacerbates this effect. The profiles of total aqueous carbonate concentrations (Figure 6.8-27) are consistent with this trend, showing a significant decrease in relative spread when concentrations increase after approximately 600 years until about 2000 years, then spreading wider again after that time.

After the rise in CO_2 concentrations, the simulation using a constant 6 mm/yr infiltration rate predicts an earlier decrease in these concentrations than other simulations (all using 25 mm/yr in this time period) (Figure 6.8-25b). In the 25 mm/yr cases, CO_2 concentrations diminish at later times because more CO_2 was mobilized (exsolved from incoming water) prior to the collapse of the boiling front. Note that in the 6 mm/yr case, CO_2 concentrations rise again somewhat after 15,000 years because of a second small pulse of slightly more carbonated water percolating downwards (related to the various degrees of water-rock interaction in the different stratigraphic units further above the drift).

The predicted range of pH values covered by all simulations (Figure 6.8-26) is from approximately 7.2 to 8.4. This range is fairly small and is similar to the range predicted previously for locations directly adjacent to the drift wall. After long periods of time (> 10,000 years), predicted pH values for runs using the different input water compositions tend to converge towards similar ambient values (in the 8.2–8.4 range after 100,000 years). Values of pH rise towards these ambient values after a decrease (from approximately 600 to 2,000 years) caused by the percolation of more carbonated and thus slightly more acidic waters as discussed above. For some of the waters considered, these long-term ambient values are slightly higher than initial values (in the ~8–8.3 range, see Table 6.2-1) because the long-term alteration of rock-forming minerals (e.g., Equations. 6.5-1 and 6.5-2) tends to drive the pH up.

The concentration profiles of conservative species such as chloride (Figure 6.8-28) (and also nitrate in simulations presented here; Figure 6.8-29) are useful in evaluating the degree of dilution and evaporative concentration in the areas for which predicted water compositions are shown. Dilution from condensation initially occurs (within a factor of around 10) after the onset of boiling. However, later in the boiling period, evaporative concentration takes over (also within a factor of around 10, compared to initial values). Comparing the chloride concentration profiles (Figure 6.8-28) with profiles showing the distance from drift center at which these concentrations occur (Figure 6.8-22) helps in distinguishing the following successive stages in the evolution of water composition in the condensation zone:

1. A dilution stage occurs when the dryout zone is expanding, roughly from 50 to around 100-150 years. It is caused by steam originating from water boiling in the rock matrix then migrating and condensing into fractures (Section 6.2.1.1).

2. An evaporative concentration stage takes place while the high liquid saturation zone remains essentially stationary. The water in fractures is concentrated by boiling the percolating water, with no or little additional influx of condensation water derived from boiling matrix water. This stage lasts approximately from 150 years to 600 years for most waters, but is shorter by several hundred years under the higher infiltration rate (Figure 6.8-28).

3. A "back-to-ambient" stage starts while boiling is still occurring, after approximately 600 years (and earlier at higher infiltration rates), then continuing after the collapse of the boiling front. During this stage, the dilution by percolating waters overcomes the effect of evaporative concentration and brings concentrations back to their ambient values.

The effects of these three distinct stages are visible on the predicted concentration trends of most constituents. In the case of chloride, looking at the results of all simulations, concentrations drop to as low as around 1 ppm (with Water W6) during the dilution stage and rise to as high as approximately 1,500 ppm (with Water W0) during the evaporative concentration stage (Figure 6.8-28).

The trends of most other aqueous species can be evaluated in terms of the degree of dilution, concentration, and mineral reaction taking place. By dividing aqueous species concentrations by chloride concentrations, the relative degree of mineral dissolution or precipitation can be evaluated. However, the variations of these ratios do not necessarily indicate that reactions are taking place in the gridblocks where the ratios are evaluated. Reactions in the rock matrix could also affect these ratios in fracture water if significant diffusion were to occur between fractures and matrix. Reactions above areas being investigated could also affect these ratios. In the present simulations, in zones of highest liquid saturation above the drift crown, predicted increases in Ca/Cl in fractures during the dilution stage (after the onset of boiling and steam condensation) (Figure 6.8-31) result from calcite dissolution in fractures. This dissolution is enhanced by the somewhat lower pH of condensation waters caused by CO_2 dissolution (see also Section 7.1). After this time, when evaporative concentration takes over, Ca/Cl ratios decrease through precipitation of calcite and, to a lesser extent, of stellerite. The trends of Ca/Cl ratios in logarithmic form (Figure 6.8-31) are similar and somewhat parallel for all simulations,

suggesting that the degree of reaction involving calcium minerals is similar in all cases considered.

The Na/Cl ratios in fracture water also increase initially during the dilution stage (Figure 6.8-33), but much less than Ca/Cl ratios. The increase in this case results from albite dissolution (accompanied by stellerite precipitation, e.g., Equations 6.5-1 and 6.5-2), which occurs at a much slower rate than calcite dissolution. After the dilution stage, the Na/Cl ratios decrease significantly, even though albite is still dissolving in fractures. The Na/Cl decrease in this case appears to result from sodium diffusion into the rock matrix where albite precipitation is taking place (not shown here). This trend is eventually reversed by the continued alteration of albite to stellerite in fractures, which becomes even more pronounced as the evaporative stage ends. Like the Ca/Cl ratios, the similar and somewhat parallel trends of Na/Cl ratios (in logarithmic form) would suggest that all waters react to a similar degree with sodium phases.

As discussed in Section 6.2.2.1, the ratio of calcium to total aqueous carbonate concentration (expressed here as Ca/HCO_3) gives some indication of the likelihood for a water to evolve towards a potentially deleterious calcium chloride brine upon continued evaporation. These brines are more likely to form in initial waters with a Ca/HCO_3 molal ratio greater than 0.5 (or, in equivalents, a ratio greater than 1). These values are exceeded during the evaporative concentration stage for all considered initial water compositions (Figure 6.8-34). However, Waters W0 and W7 display Ca/HCO_3 ratios significantly higher than the other waters. Water W4 shows the lowest ratios.

Ratios of nitrate to chloride (Figure 6.8-35) remain essentially constant. This is expected because redox processes are not considered in these simulations, and solid nitrate and chloride phases are formed only upon complete dryout (Section 6.4.5). The redissolution of nitrate and chloride salts formed during dryout has a short-lived, hardly noticeable effect in zones with the highest liquid saturations.

The predicted magnesium concentrations (Figure 6.8-36) reflect the effects of the dilutive and evaporative concentration stages discussed earlier, but remain significantly depressed below ambient values after the boiling period. The magnesium depletion is caused by the precipitation of sepiolite early in the simulations. This depletion is also observed in the simulations of ambient conditions (Section 6.8.5.1) and is not consistent with observed water compositions at Yucca Mountain. One reason may be that sepiolite is either too stable or that it does not belong in the set of selected potential secondary minerals. REV01 simulations (ambient and thermal pulse) without sepiolite in the geochemical system did not predict such magnesium depletion. Another reason for underestimating magnesium concentrations could be the lack of primary magnesium-bearing minerals in simulations (e.g., biotite). These minerals, however, occur in small amounts in the repository host units. Younger calcite at Yucca Mountain has been reported to contain up to around 1% (by weight) magnesium (Wilson et al. 2000 [154279]). Therefore, taking this into account in simulations would also have an effect on predicted magnesium concentrations. This would contribute more magnesium in solution during calcite dissolution, but could also result in magnesium depletion upon calcite precipitation (under both thermal loading and ambient conditions).

Predicted dissolved silica concentration profiles (Figure 6.8-37) show the same effects of dilution and evaporative concentration as most other species. Profiles of SiO_2/Cl ratios (not shown here) have the same general shape as the Ca/Cl profiles (Figure 6.8-31) and indicate significant silica dissolution during the dilution stage, as would be expected. Later, continued reflux and boiling lead to an increase in concentrations. Predicted concentrations eventually reached values greater than the solubility of amorphous silica (around 350 ppm at 95°C). This is because at this point, the calculated precipitation rate of amorphous silica, although quite fast, cannot keep up with the boiling rate. In the natural system, these elevated concentrations (up to around 1,200 ppm) may not be reached.

Predicted fluoride concentrations (Figure 6.8-38) follow a trend similar to the trend of silica and other aqueous species. The host rock is modeled with a small, ubiquitous amount of primary fluorite. As noted earlier, because the reaction rate of fluorite is fast, waters generally reach saturation with respect to this mineral. During the boiling and refluxing stage, concentrations up to around 40 ppm are predicted, which are much larger than the concentration (~ 1.4 ppm) calculated by equilibrating fluorite with the solution, using the maximum calcium concentrations (around 0.02 molal, see Figure 6.8-30) predicted during that time period. In this case also, the precipitation rate of fluorite cannot keep up with the boiling rate. Eventually, concentrations come back to values dictated by equilibrium of ambient waters with fluorite (typically in the 4–8 ppm range).
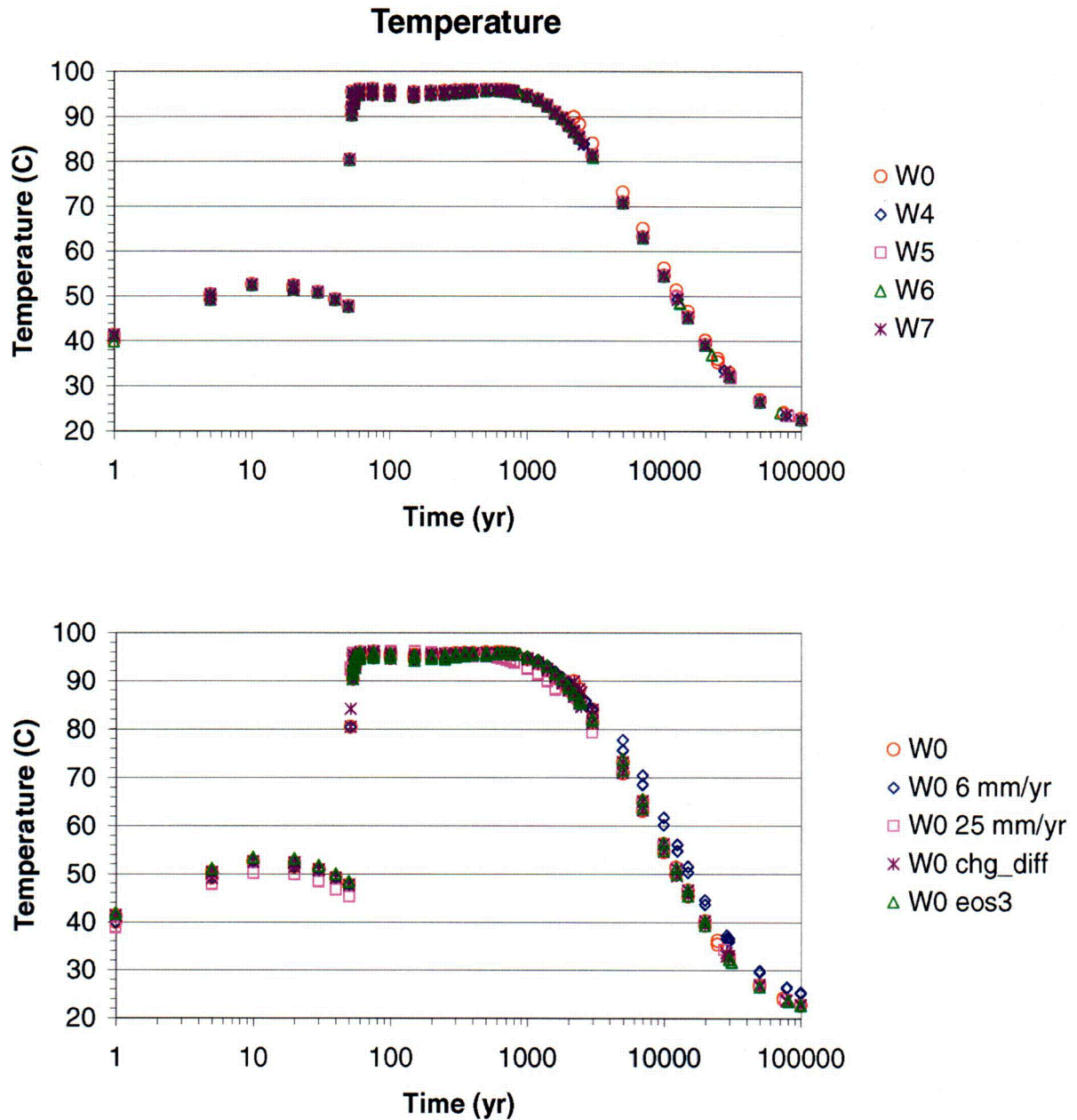
Location of High-Liquid Saturation Nodes
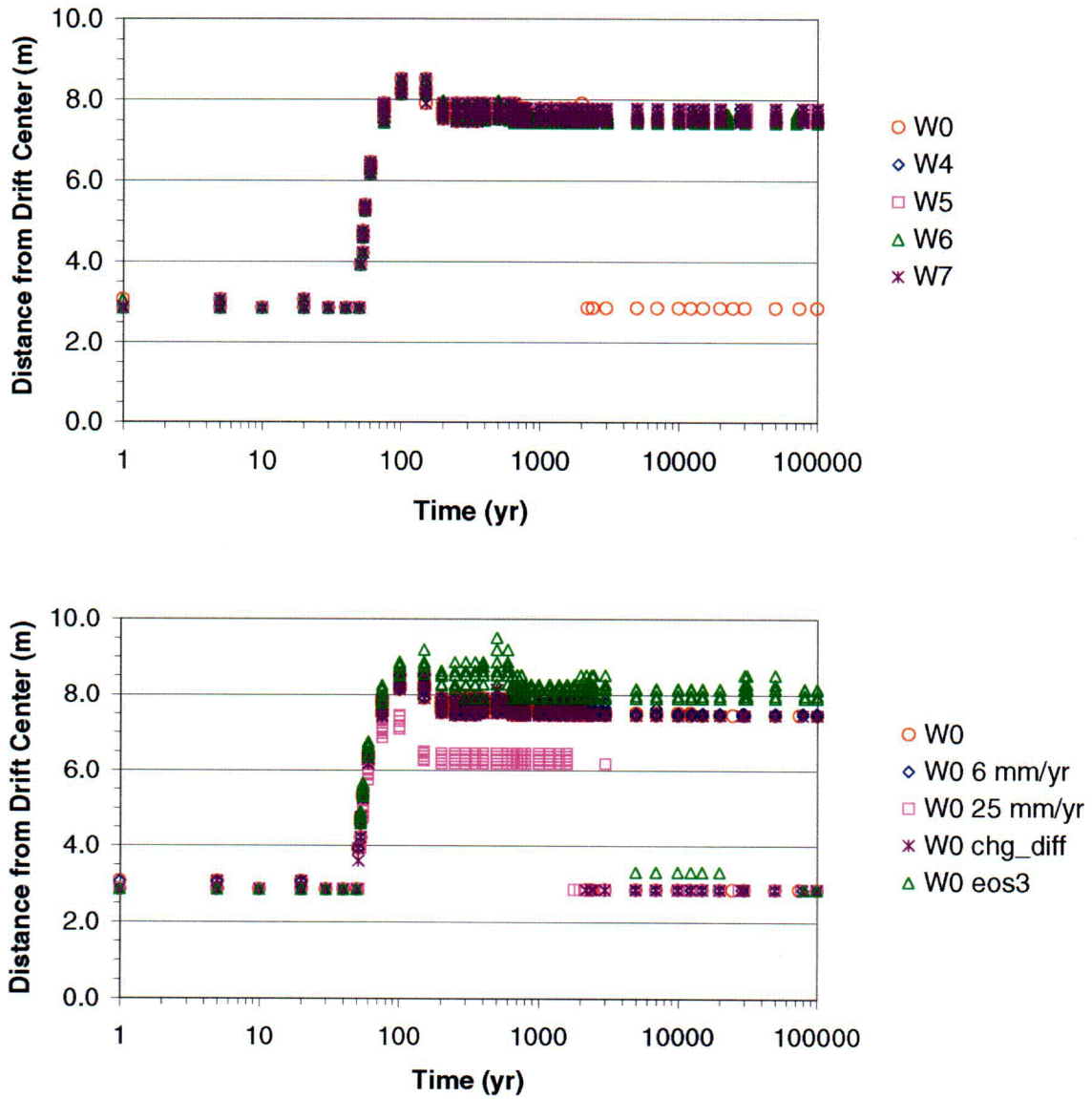
Output-DTNs: LB0302DSCPTHCS.002, LB0307DSTTHCR2.002

NOTE: Gridblocks are those with highest liquid saturation in fractures within a 25 m radius from drift center and a 45° arc from the drift crown. Data are shown for simulations using different initial water compositions (W0 – W7). Except as noted below, all simulations were run using a stepwise-increasing infiltration rate (6, 16, and 25 mm/y) and with vapor pressure lowering. Alternatives using Water W0 include simulations without vapor pressure lowering (W0 - eos3), and with fixed 25 and 6 mm/y infiltration rates (W0 - 6 mm/y and W0 - 25 mm/y, respectively).

Figure 6.8-22.   THC Simulations (Tptpll Model REV02): Location of Model Gridblocks for Data Shown on Figures 6.8-23–6.8-38, for Each Time When Model Output Is Produced
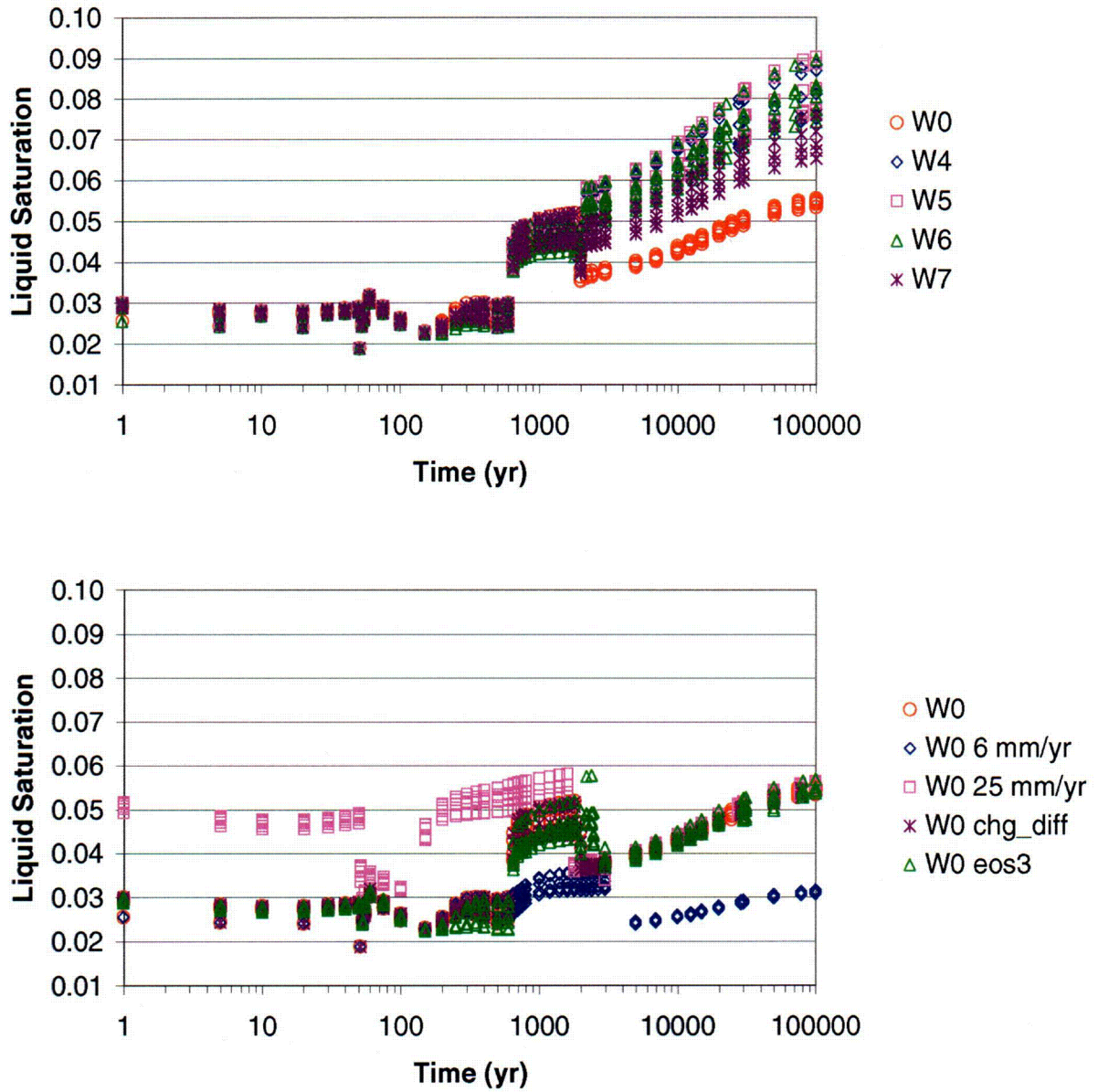
C75

Temperature

Output-DTNs: LB0302DSCPTHCS.002, LB0307DSTTHCR2.002

NOTE: Gridblocks are those with highest liquid saturation in fractures within a 25 m radius from drift center and a 45° arc from the drift crown. Data are shown for simulations using different initial water compositions (W0 – W7). Except as noted below, all simulations were run using a stepwise-increasing infiltration rate (6, 16, and 25 mm/y) and with vapor pressure lowering. Alternatives using Water W0 include simulations without vapor pressure lowering (W0 - eos3), and with fixed 25 and 6 mm/y infiltration rates (W0 - 6 mm/y and W0 - 25 mm/y, respectively).

Figure 6.8-23. THC Simulations (Tptpll Model REV02): Time Profiles of Modeled Temperatures in Fracture Water, in Areas of Highest Liquid Saturation above the Drift Crown

Liquid Saturation - Fractures

Output-DTNs: LB0302DSCPTHCS.002, LB0307DSTTHCR2.002

NOTE: Gridblocks are those with highest liquid saturation in fractures within a 25 m radius from drift center
and a 45° arc from the drift crown. Data are shown for simulations using different initial water
compositions (W0 – W7). Except as noted below, all simulations were run using a stepwise-
increasing infiltration rate (6, 16, and 25 mm/y) and with vapor pressure lowering. Alternatives using
Water W0 include simulations without vapor pressure lowering (W0 - eos3), and with fixed 25 and 6
mm/y infiltration rates (W0 - 6 mm/y and W0 - 25 mm/y, respectively).

Figure 6.8-24.   THC Simulations (Tptpll Model REV02): Time Profiles of Modeled Liquid Saturations in
Fracture Water, in Areas of Highest Liquid Saturation above the Drift Crown
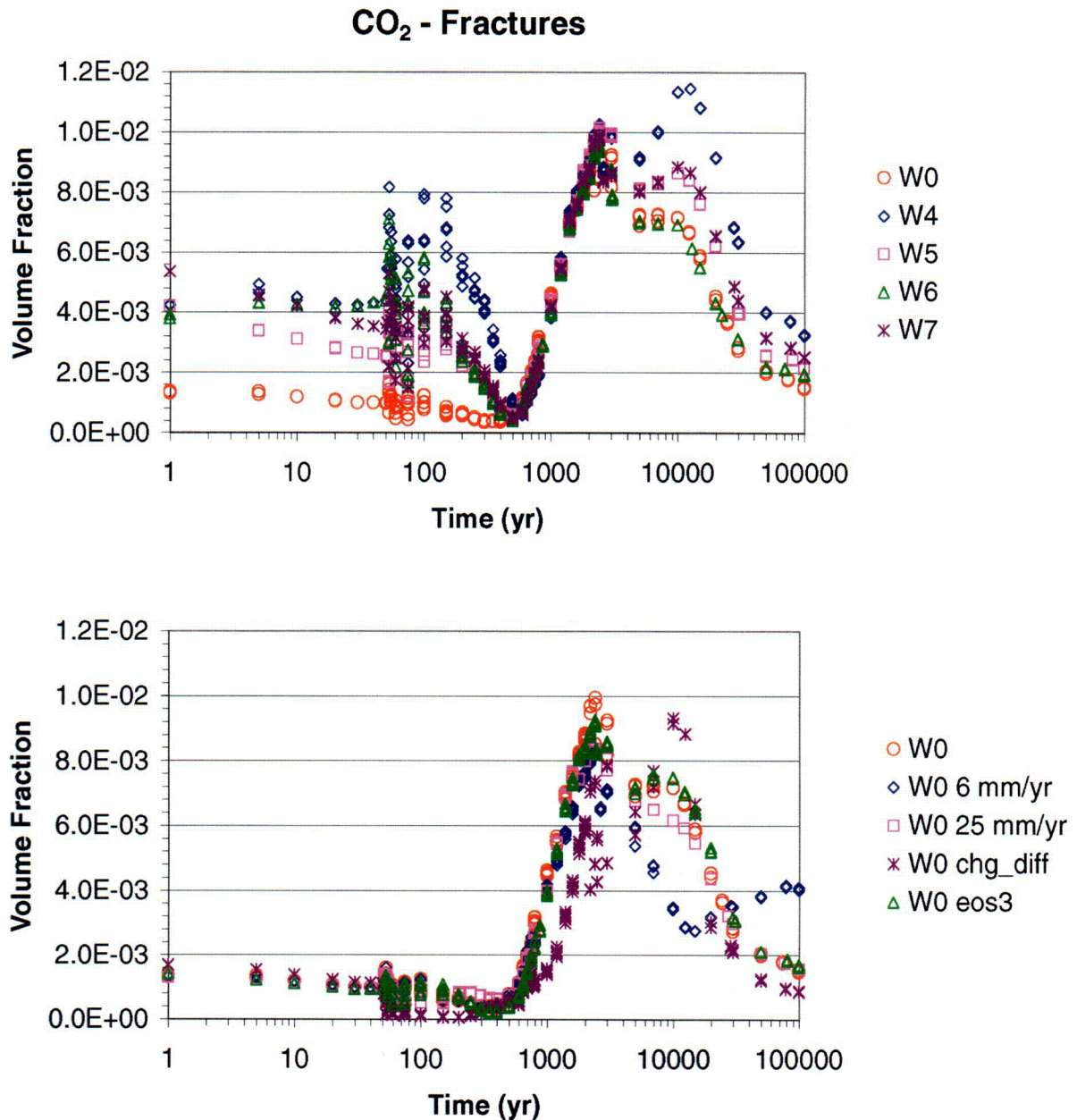
C77

CO_2 - Fractures

Output-DTNs: LB0302DSCPTHCS.002, LB0307DSTTHCR2.002

NOTE: Gridblocks are those with highest liquid saturation in fractures within a 25 m radius from drift center
        and a 45° arc from the drift crown. Data are shown for simulations using different initial water
        compositions (W0 – W7). Except as noted below, all simulations were run using a stepwise-
        increasing infiltration rate (6, 16, and 25 mm/y) and with vapor pressure lowering. Alternatives using
        Water W0 include simulations without vapor pressure lowering (W0 - eos3), and with fixed 25 and 6
        mm/y infiltration rates (W0 - 6 mm/y and W0 - 25 mm/y, respectively).

Figure 6.8-25.   THC Simulations (Tptpll Model REV02): Time Profiles of Modeled CO_2 Gas
                 Concentrations in Fracture Water, in Areas of Highest Liquid Saturation above the Drift
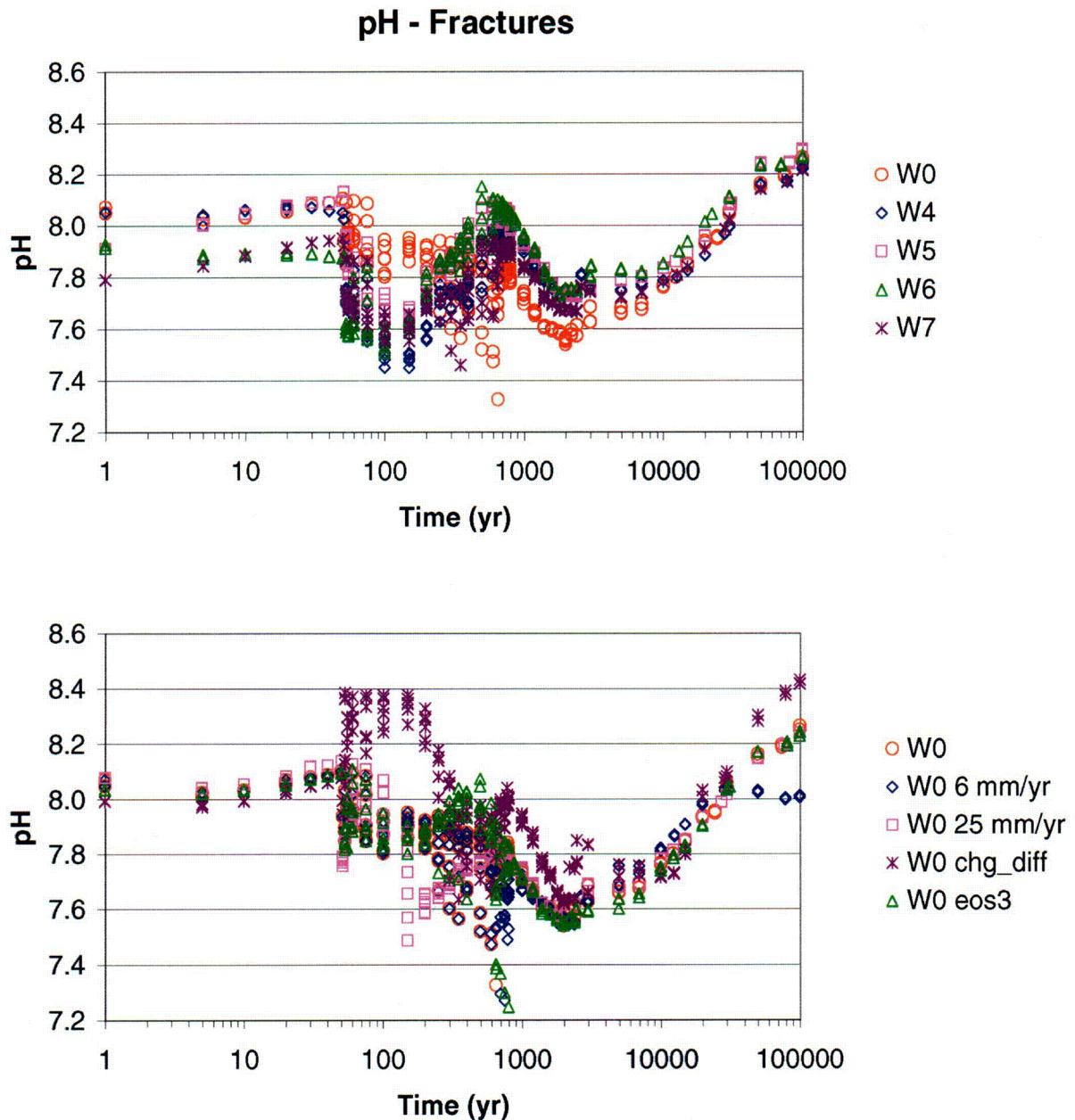   Crown

C78

pH - Fractures

Output-DTNs: LB0302DSCPTHCS.002, LB0307DSTTHCR2.002

NOTE: Gridblocks are those with highest liquid saturation in fractures within a 25 m radius from drift center and a 45° arc from the drift crown. Data are shown for simulations using different initial water compositions (W0 – W7). Except as noted below, all simulations were run using a stepwise-increasing infiltration rate (6, 16, and 25 mm/y) and with vapor pressure lowering. Alternatives using Water W0 include simulations without vapor pressure lowering (W0 - eos3), and with fixed 25 and 6 mm/y infiltration rates (W0 - 6 mm/y and W0 - 25 mm/y, respectively).

Figure 6.8-26. THC Simulations (Tptpll Model REV02): Time Profiles of Modeled pH in Fracture Water, in Areas of Highest Liquid Saturation above the Drift Crown
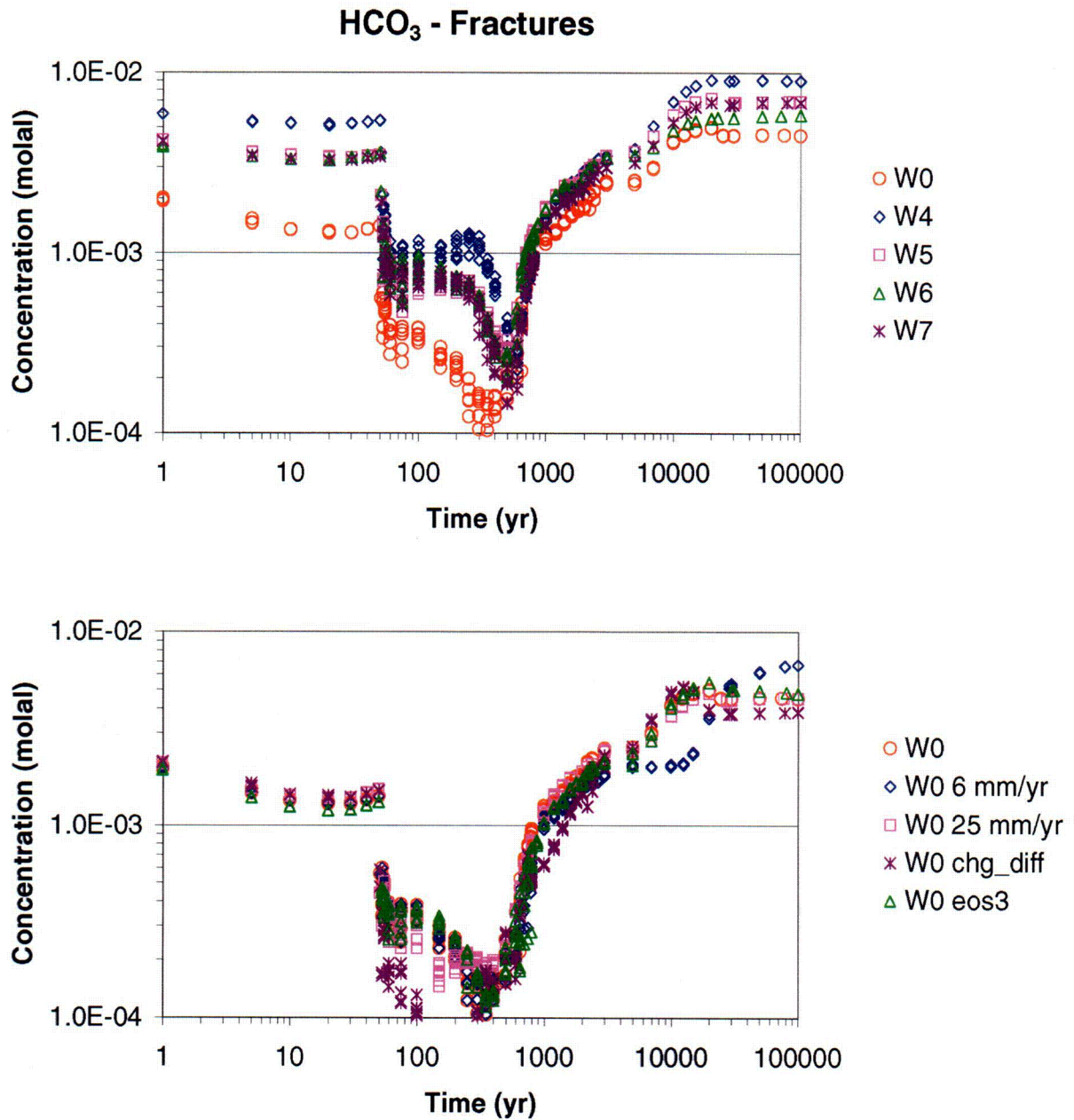
HCO₃ - Fractures

Output-DTNs: LB0302DSCPTHCS.002, LB0307DSTTHCR2.002

NOTE: Gridblocks are those with highest liquid saturation in fractures within a 25 m radius from drift center and a 45° arc from the drift crown. Data are shown for simulations using different initial water compositions (W0 – W7). Except as noted below, all simulations were run using a stepwise-increasing infiltration rate (6, 16, and 25 mm/y) and with vapor pressure lowering. Alternatives using Water W0 include simulations without vapor pressure lowering (W0 - eos3), and with fixed 25 and 6 mm/y infiltration rates (W0 - 6 mm/y and W0 - 25 mm/y, respectively).

Figure 6.8-27.   THC Simulations (Tptpll Model REV02): Time Profiles of Modeled Total Aqueous Carbonate Concentrations (as HCO₃) in Fracture Water, in Areas of Highest Liquid Saturation above the Drift Crown
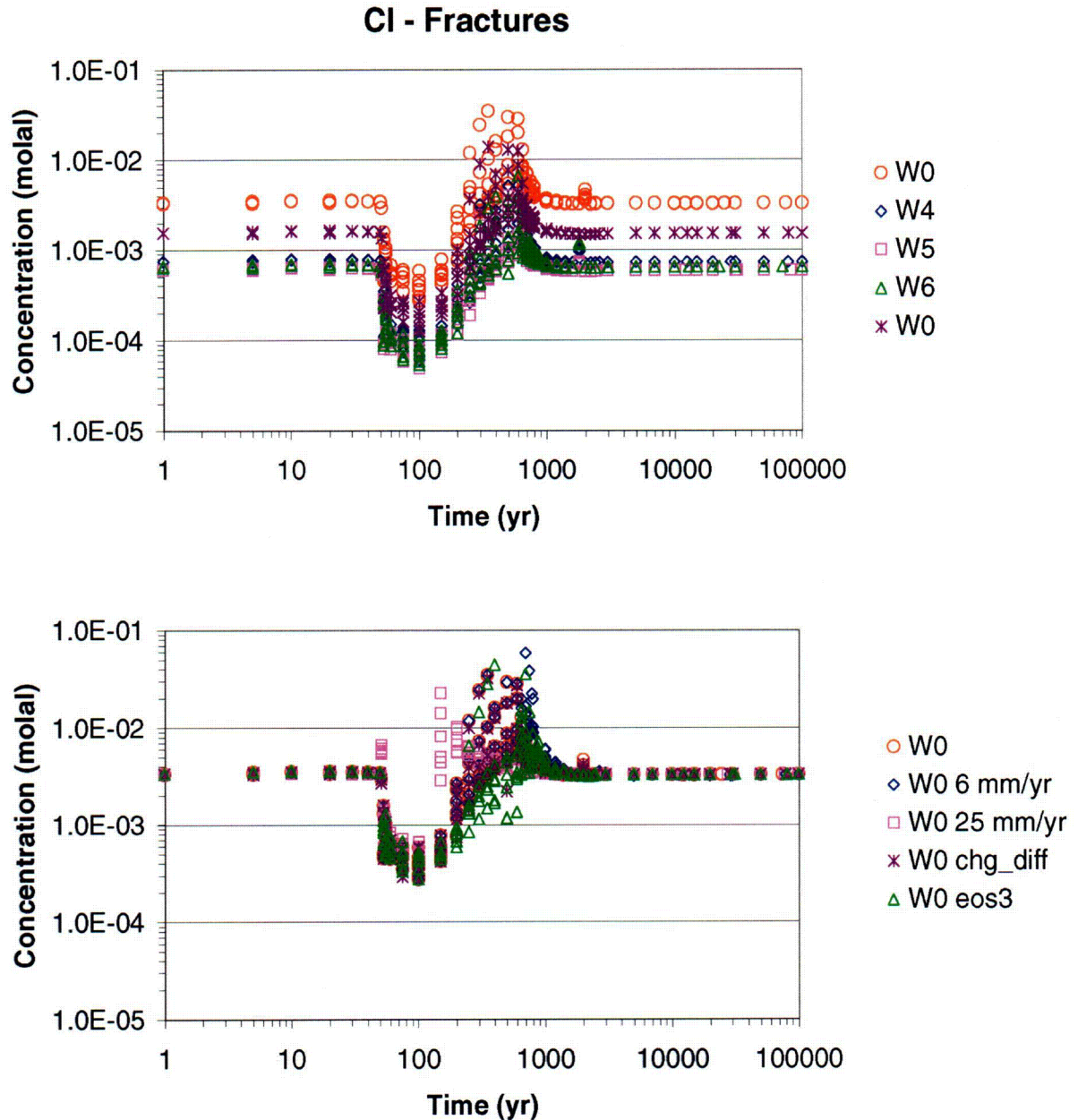
Cl - Fractures

Output-DTNs: LB0302DSCPTHCS.002, LB0307DSTTHCR2.002

NOTE: Gridblocks are those with highest liquid saturation in fractures within a 25 m radius from drift center
         and a 45° arc from the drift crown. Data are shown for simulations using different initial water
         compositions (W0 – W7). Except as noted below, all simulations were run using a stepwise-
         increasing infiltration rate (6, 16, and 25 mm/y) and with vapor pressure lowering. Alternatives using
         Water W0 include simulations without vapor pressure lowering (W0 - eos3), and with fixed 25 and 6
         mm/y infiltration rates (W0 - 6 mm/y and W0 - 25 mm/y, respectively).

Figure 6.8-28.   THC Simulations (Tptpll Model REV02): Time Profiles of Modeled Total Aqueous
                  Chloride Concentrations in Fracture Water, in Areas of Highest Liquid Saturation above
                  the Drift Crown
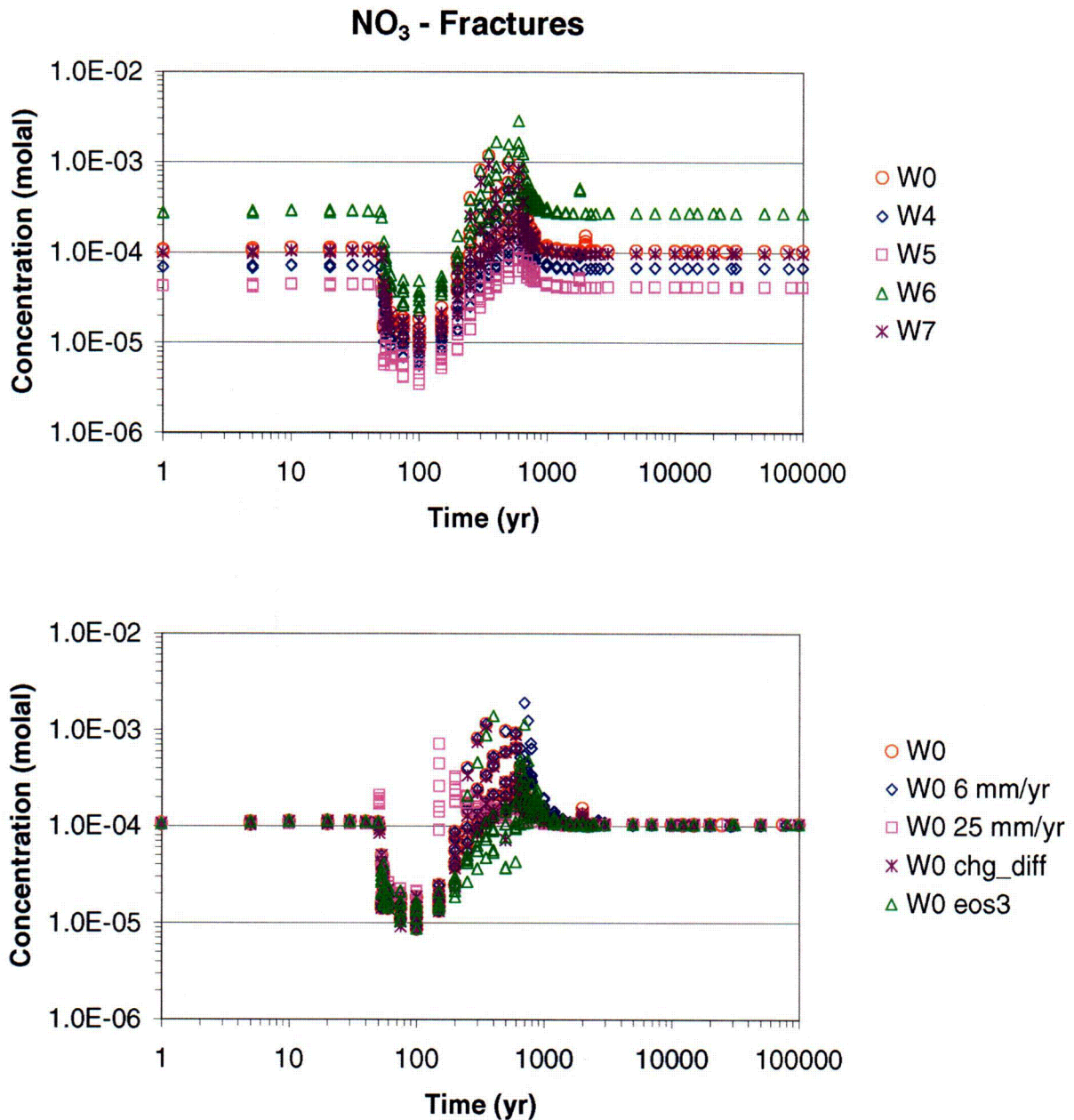
c81

NO$_3$ - Fractures

Output-DTNs: LB0302DSCPTHCS.002, LB0307DSTTHCR2.002

NOTE: Gridblocks are those with highest liquid saturation in fractures within a 25 m radius from drift center and a 45° arc from the drift crown. Data are shown for simulations using different initial water compositions (W0 – W7). Except as noted below, all simulations were run using a stepwise-increasing infiltration rate (6, 16, and 25 mm/y) and with vapor pressure lowering. Alternatives using Water W0 include simulations without vapor pressure lowering (W0 - eos3), and with fixed 25 and 6 mm/y infiltration rates (W0 - 6 mm/y and W0 - 25 mm/y, respectively).

Figure 6.8-29.   THC Simulations (Tptpll Model REV02): Time Profiles of Modeled Total Aqueous Nitrate Concentrations in Fracture Water, in Areas of Highest Liquid Saturation above the Drift Crown
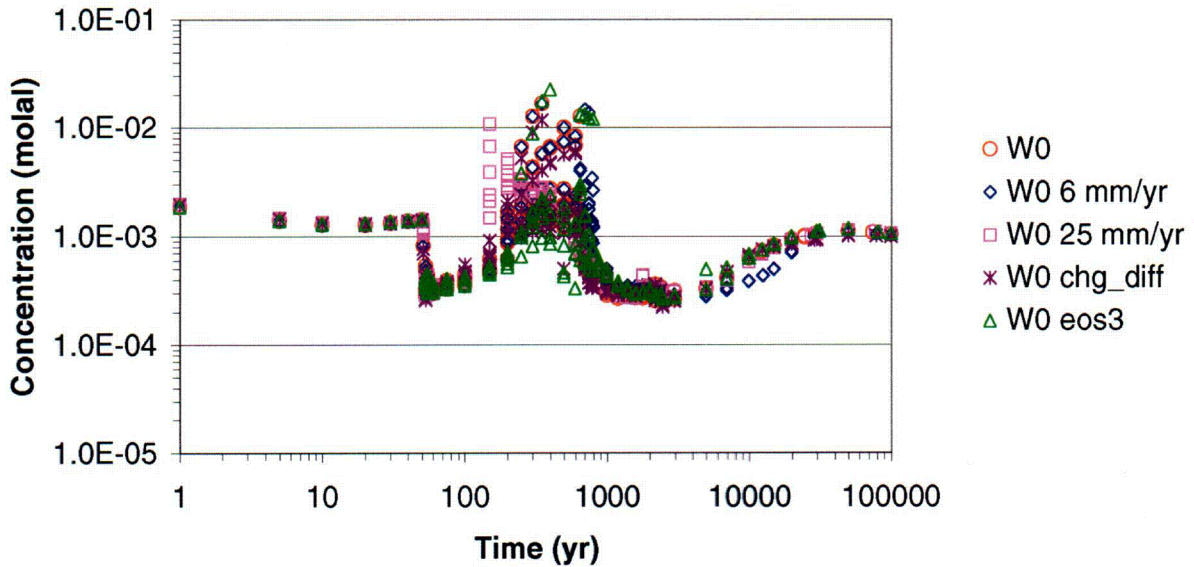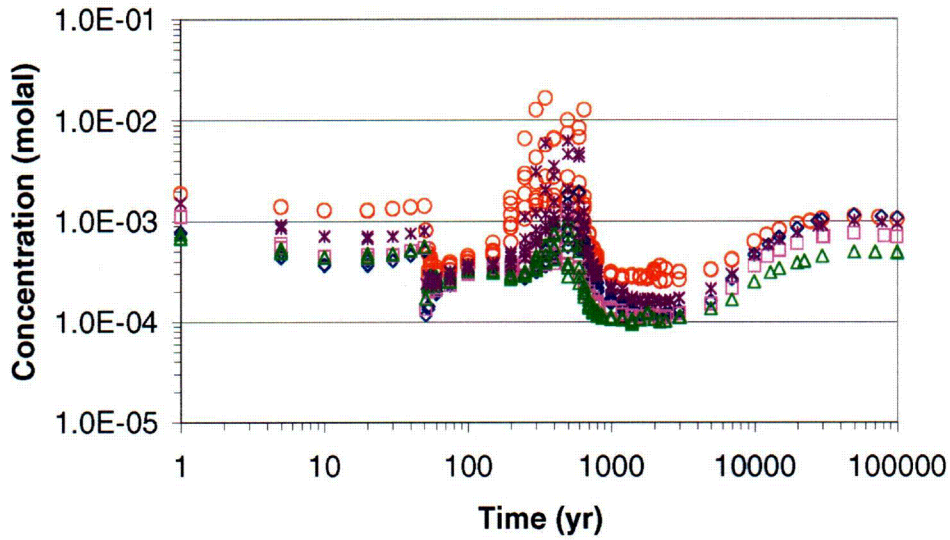
C82

Ca - Fractures

Output-DTNs: LB0302DSCPTHCS.002, LB0307DSTTHCR2.002

NOTE: Gridblocks are those with highest liquid saturation in fractures within a 25 m radius from drift center and a 45° arc from the drift crown. Data are shown for simulations using different initial water compositions (W0 – W7). Except as noted below, all simulations were run using a stepwise-increasing infiltration rate (6, 16, and 25 mm/y) and with vapor pressure lowering. Alternatives using Water W0 include simulations without vapor pressure lowering (W0 - eos3), and with fixed 25 and 6 mm/y infiltration rates (W0 - 6 mm/y and W0 - 25 mm/y, respectively).

Figure 6.8-30.   THC Simulations (Tptpll Model REV02): Time Profiles of Modeled Total Aqueous Calcium Concentrations in Fracture Water, in Areas of Highest Liquid Saturation above the Drift Crown
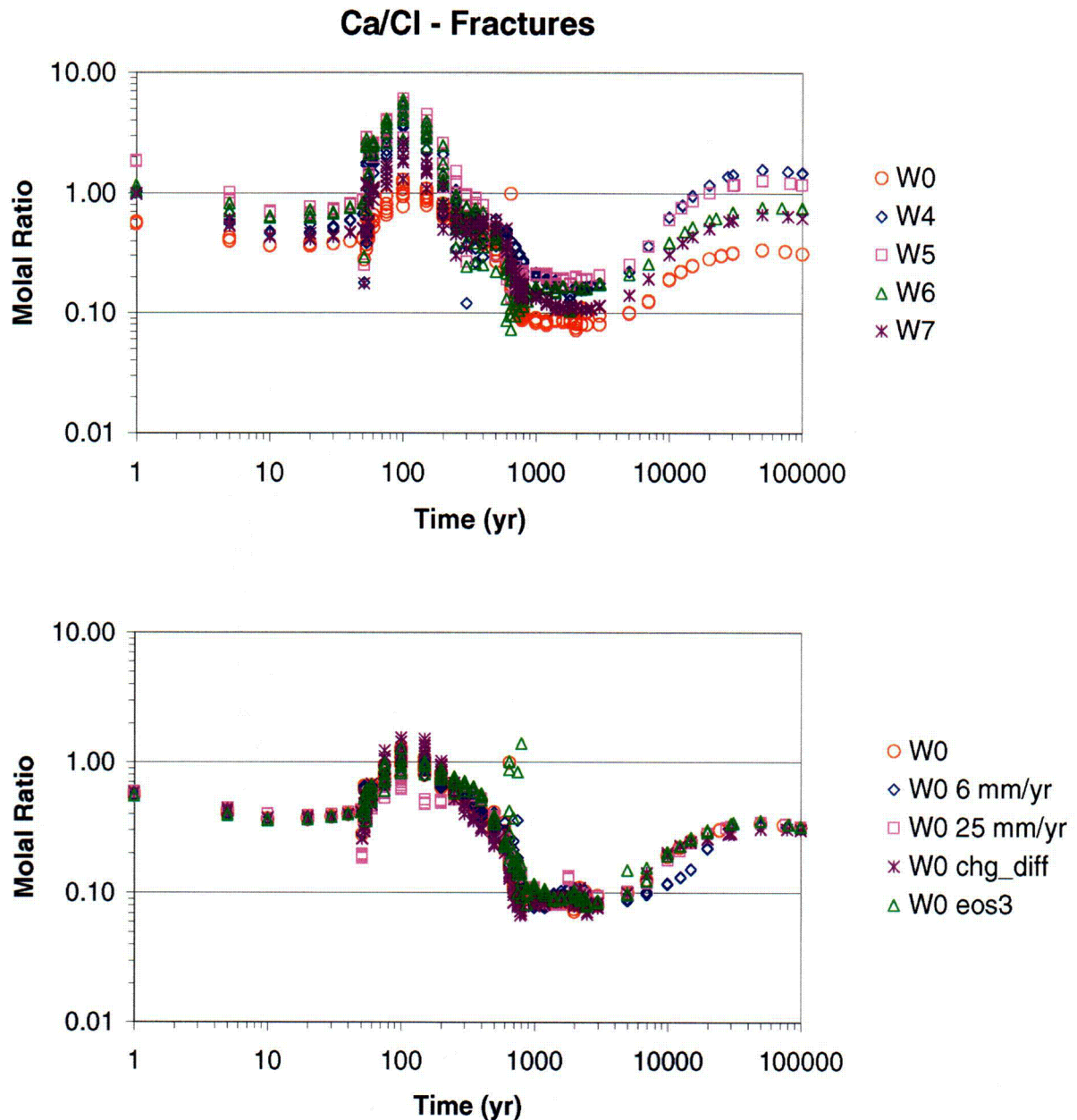
C83

Ca/Cl - Fractures

Output-DTNs: LB0302DSCPTHCS.002, LB0307DSTTHCR2.002

NOTE: Gridblocks are those with highest liquid saturation in fractures within a 25 m radius from drift center
        and a 45° arc from the drift crown. Data are shown for simulations using different initial water
        compositions (W0 – W7). Except as noted below, all simulations were run using a stepwise-
        increasing infiltration rate (6, 16, and 25 mm/y) and with vapor pressure lowering. Alternatives using
        Water W0 include simulations without vapor pressure lowering (W0 - eos3), and with fixed 25 and 6
        mm/y infiltration rates (W0 - 6 mm/y and W0 - 25 mm/y, respectively).

Figure 6.8-31.   THC Simulations (Tptpll Model REV02): Time Profiles of Modeled Total Aqueous Calcium
                 to Chloride Ratios in Fracture Water, in Areas of Highest Liquid Saturation above the Drift
                 Crown
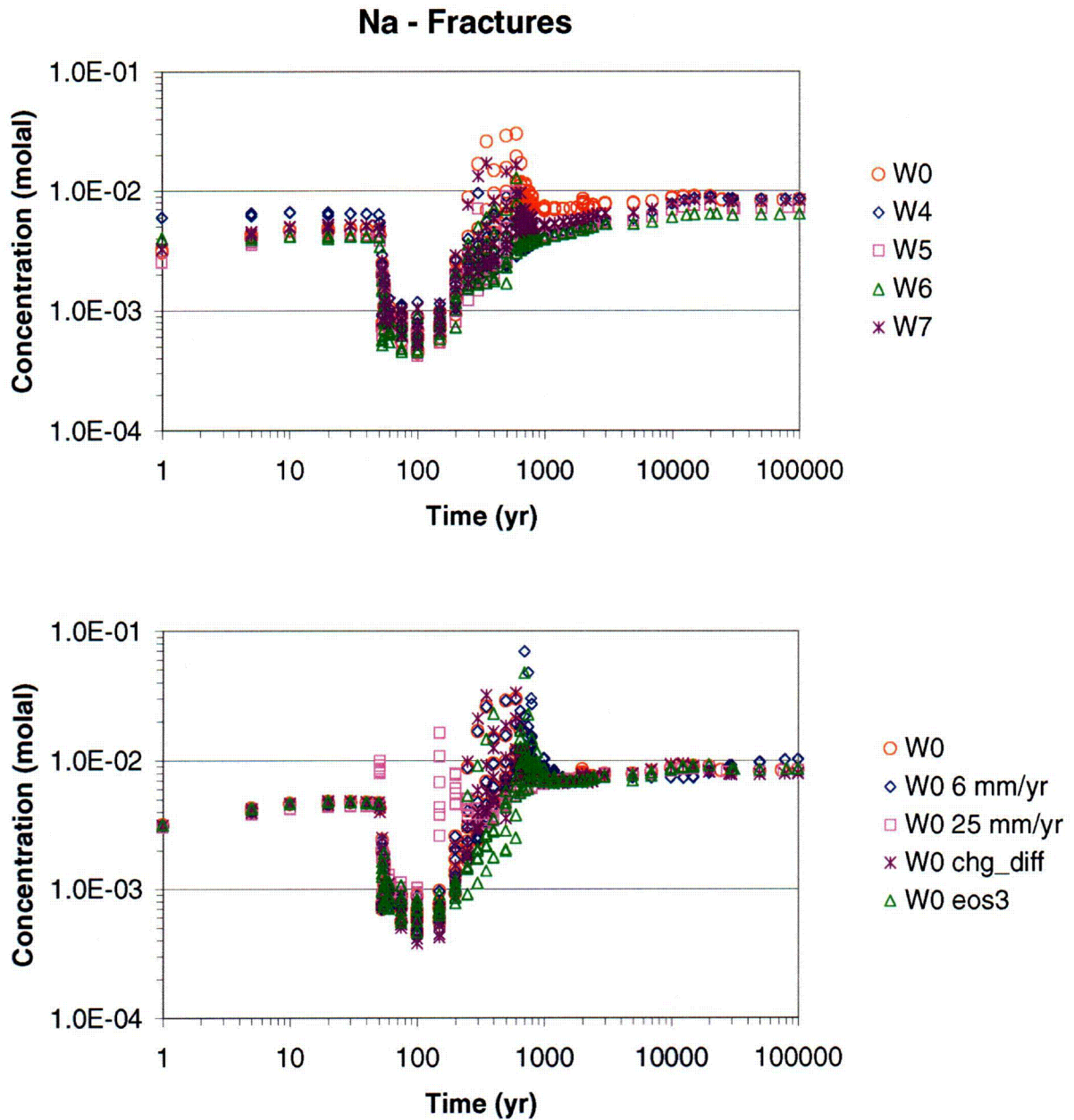
C84

Na - Fractures

Output-DTNs: LB0302DSCPTHCS.002, LB0307DSTTHCR2.002

NOTE: Gridblocks are those with highest liquid saturation in fractures within a 25 m radius from drift center and a 45° arc from the drift crown. Data are shown for simulations using different initial water compositions (W0 – W7). Except as noted below, all simulations were run using a stepwise-increasing infiltration rate (6, 16, and 25 mm/y) and with vapor pressure lowering. Alternatives using Water W0 include simulations without vapor pressure lowering (W0 - eos3), and with fixed 25 and 6 mm/y infiltration rates (W0 - 6 mm/y and W0 - 25 mm/y, respectively).

Figure 6.8-32.   THC Simulations (Tptpll Model REV02): Time Profiles of Modeled Total Aqueous Sodium Concentrations in Fracture Water, in Areas of Highest Liquid Saturation above the Drift Crown
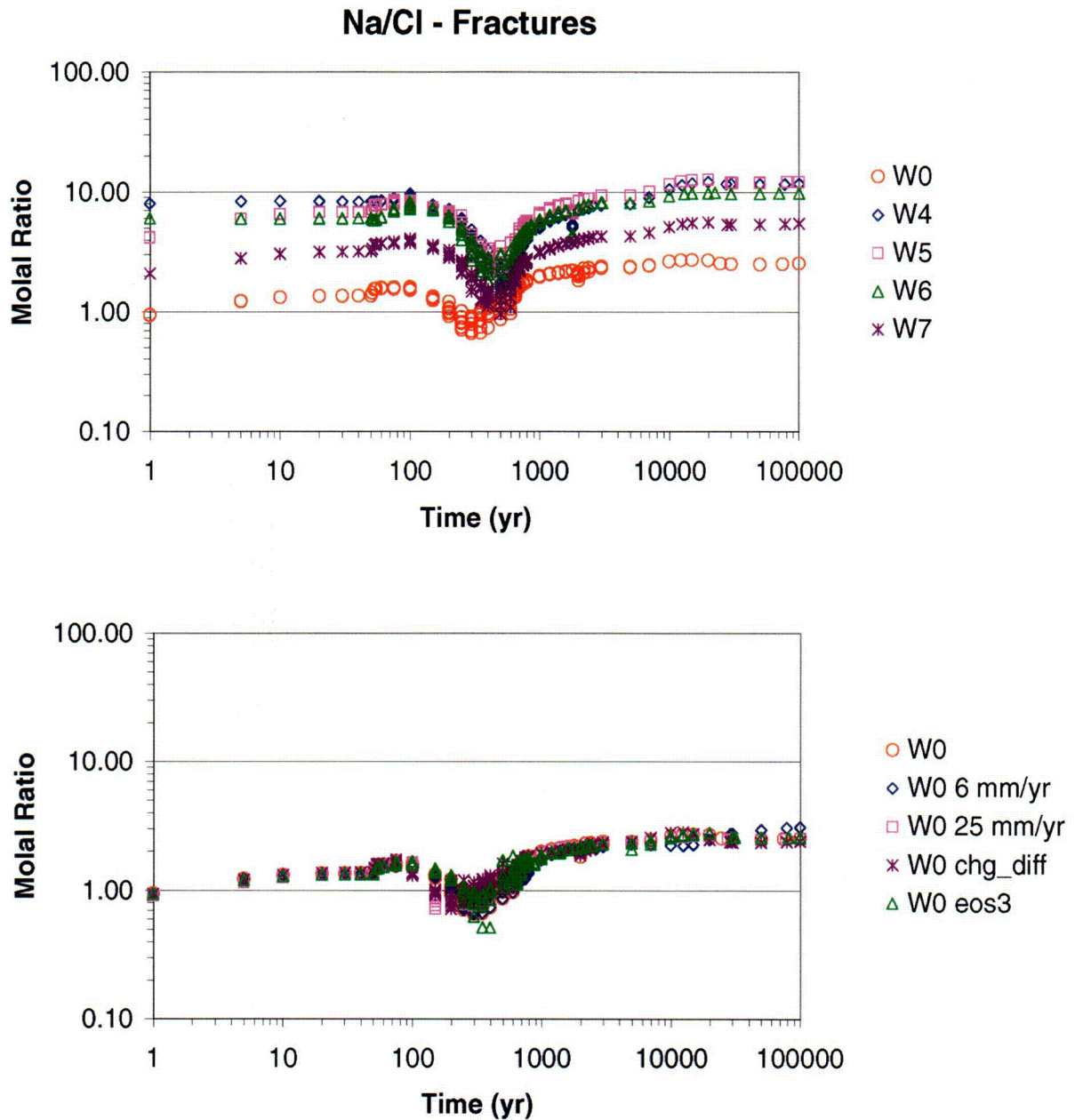
C85

Na/Cl - Fractures

Output-DTNs: LB0302DSCPTHCS.002, LB0307DSTTHCR2.002

NOTE: Gridblocks are those with highest liquid saturation in fractures within a 25 m radius from drift center and a 45° arc from the drift crown. Data are shown for simulations using different initial water compositions (W0 – W7). Except as noted below, all simulations were run using a stepwise-increasing infiltration rate (6, 16, and 25 mm/y) and with vapor pressure lowering. Alternatives using Water W0 include simulations without vapor pressure lowering (W0 - eos3), and with fixed 25 and 6 mm/y infiltration rates (W0 - 6 mm/y and W0 - 25 mm/y, respectively).

Figure 6.8-33. THC Simulations (Tptpll Model REV02): Time Profiles of Modeled Total Aqueous Sodium to Chloride Ratios in Fracture Water, in Areas of Highest Liquid Saturation above the Drift Crown
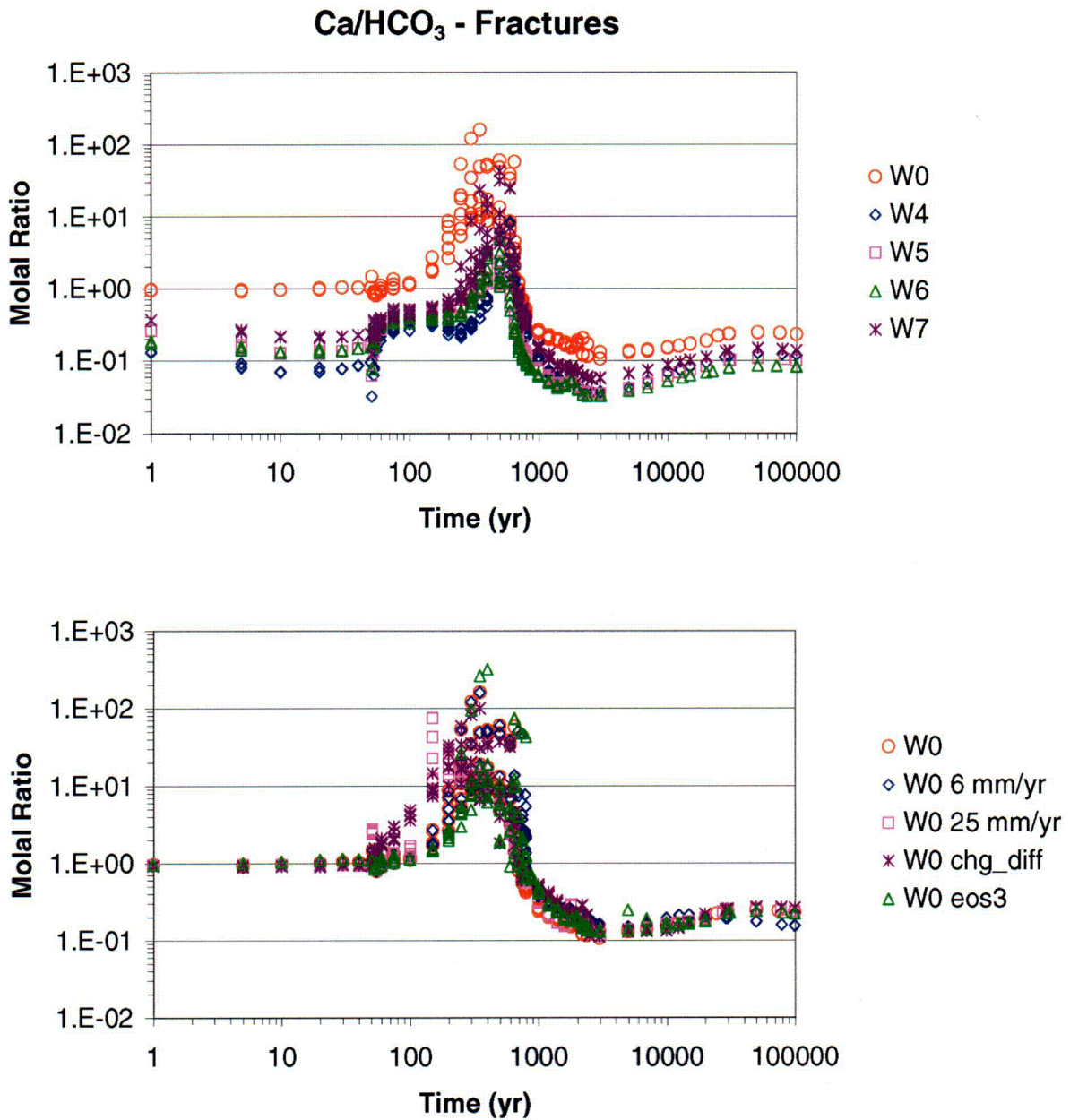
C86

Ca/HCO$_3$ - Fractures

Output-DTNs: LB0302DSCPTHCS.002, LB0307DSTTHCR2.002

NOTE: Gridblocks are those with highest liquid saturation in fractures within a 25 m radius from drift center and a 45° arc from the drift crown. Data are shown for simulations using different initial water compositions (W0 – W7). Except as noted below, all simulations were run using a stepwise-increasing infiltration rate (6, 16, and 25 mm/y) and with vapor pressure lowering. Alternatives using Water W0 include simulations without vapor pressure lowering (W0 - eos3), and with fixed 25 and 6 mm/y infiltration rates (W0 - 6 mm/y and W0 - 25 mm/y, respectively).

Figure 6.8-34. THC Simulations (Tptpll Model REV02): Time Profiles of Modeled Total Aqueous Calcium to Carbonate Ratios in Fracture Water, in Areas of Highest Liquid Saturation above the Drift Crown
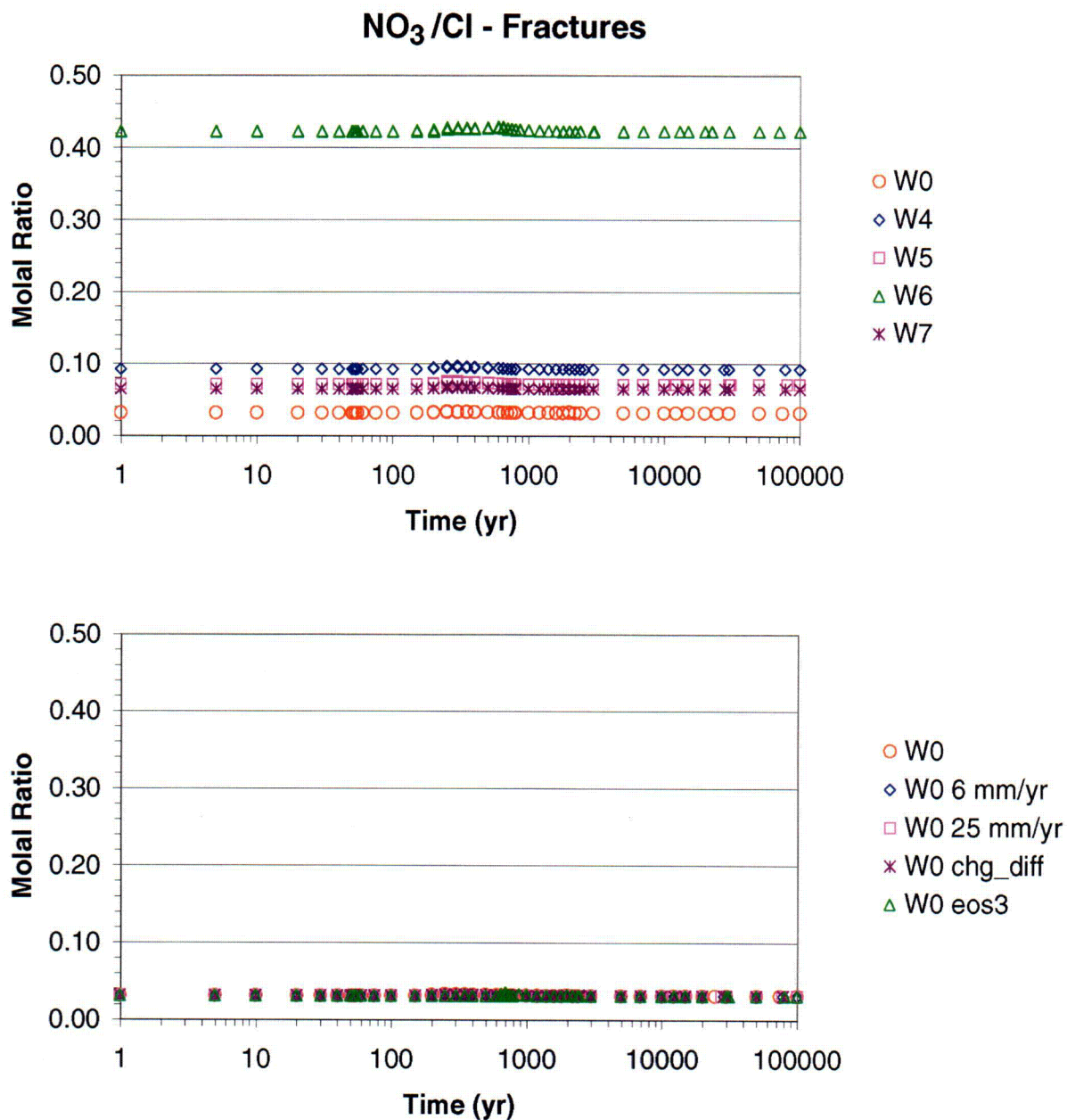
C87

NO_3/Cl - Fractures

Output-DTNs: LB0302DSCPTHCS.002, LB0307DSTTHCR2.002

NOTE: Gridblocks are those with highest liquid saturation in fractures within a 25 m radius from drift center and a 45° arc from the drift crown. Data are shown for simulations using different initial water compositions (W0 – W7). Except as noted below, all simulations were run using a stepwise-increasing infiltration rate (6, 16, and 25 mm/y) and with vapor pressure lowering. Alternatives using Water W0 include simulations without vapor pressure lowering (W0 - eos3), and with fixed 25 and 6 mm/y infiltration rates (W0 - 6 mm/y and W0 - 25 mm/y, respectively).

Figure 6.8-35. THC Simulations (Tptpll Model REV02): Time Profiles of Modeled Total Aqueous Nitrate to Chloride Ratios in Fracture Water, in Areas of Highest Liquid Saturation above the Drift Crown

C88

Mg - Fractures

Output-DTNs: LB0302DSCPTHCS.002, LB0307DSTTHCR2.002

NOTE: Gridblocks are those with highest liquid saturation in fractures within a 25 m radius from drift center and a 45° arc from the drift crown. Data are shown for simulations using different initial water compositions (W0 – W7). Except as noted below, all simulations were run using a stepwise-increasing infiltration rate (6, 16, and 25 mm/y) and with vapor pressure lowering. Alternatives using Water W0 include simulations without vapor pressure lowering (W0 - eos3), and with fixed 25 and 6 mm/y infiltration rates (W0 - 6 mm/y and W0 - 25 mm/y, respectively).

Figure 6.8-36.   THC Simulations (Tptpll Model REV02): Time Profiles of Modeled Total Aqueous Magnesium Concentrations in Fracture Water, in Areas of Highest Liquid Saturation above the Drift Crown
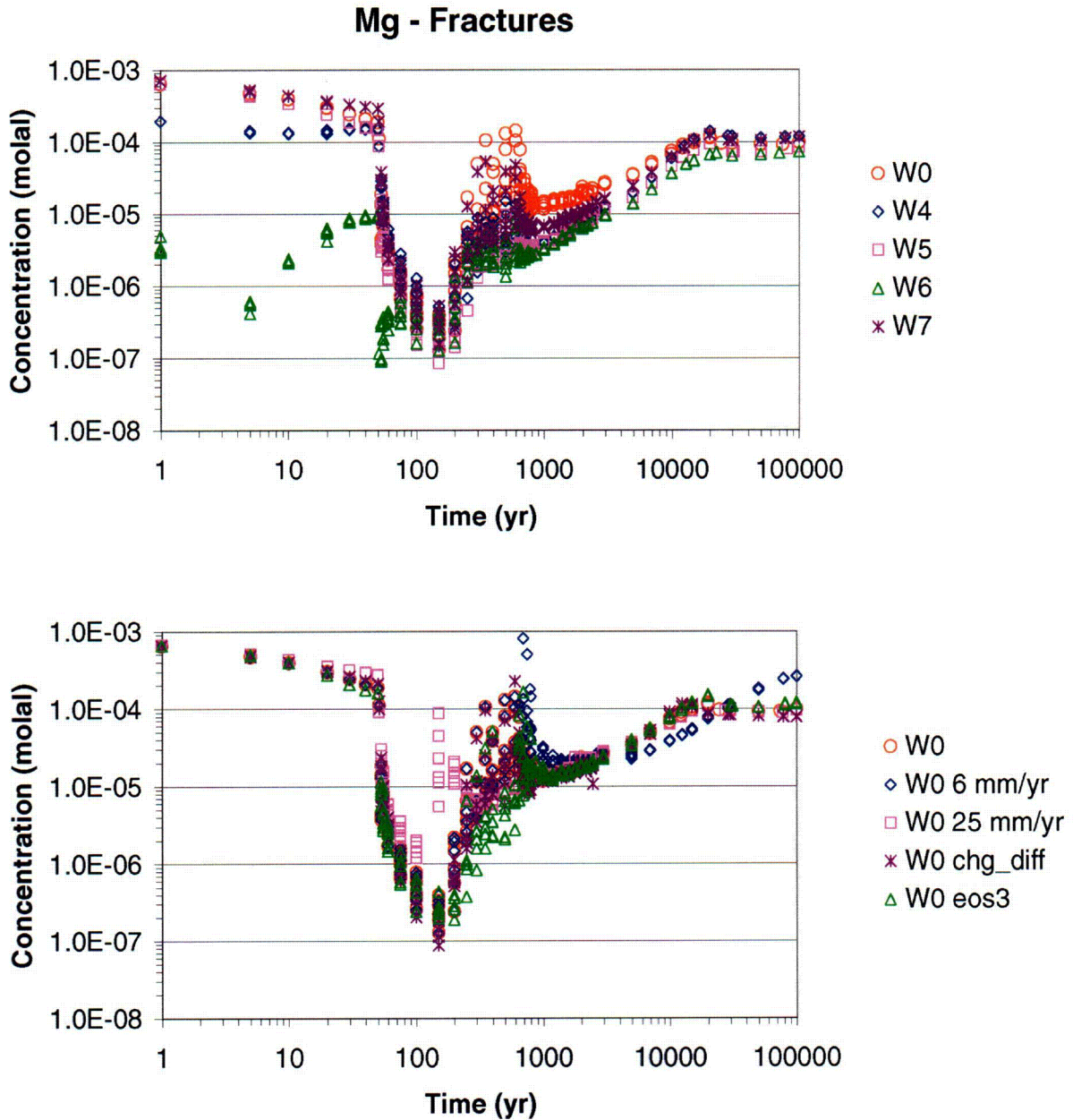
c89

SiO$_2$ - Fractures

Output-DTNs: LB0302DSCPTHCS.002, LB0307DSTTHCR2.002

NOTE: Gridblocks are those with highest liquid saturation in fractures within a 25 m radius from drift center and a 45° arc from the drift crown. Data are shown for simulations using different initial water compositions (W0 – W7). Except as noted below, all simulations were run using a stepwise-increasing infiltration rate (6, 16, and 25 mm/y) and with vapor pressure lowering. Alternatives using Water W0 include simulations without vapor pressure lowering (W0 - eos3), and with fixed 25 and 6 mm/y infiltration rates (W0 - 6 mm/y and W0 - 25 mm/y, respectively).

Figure 6.8-37. THC Simulations (Tptpll Model REV02): Time Profiles of Modeled Total Aqueous Silica Concentrations in Fracture Water, in Areas of Highest Liquid Saturation above the Drift Crown
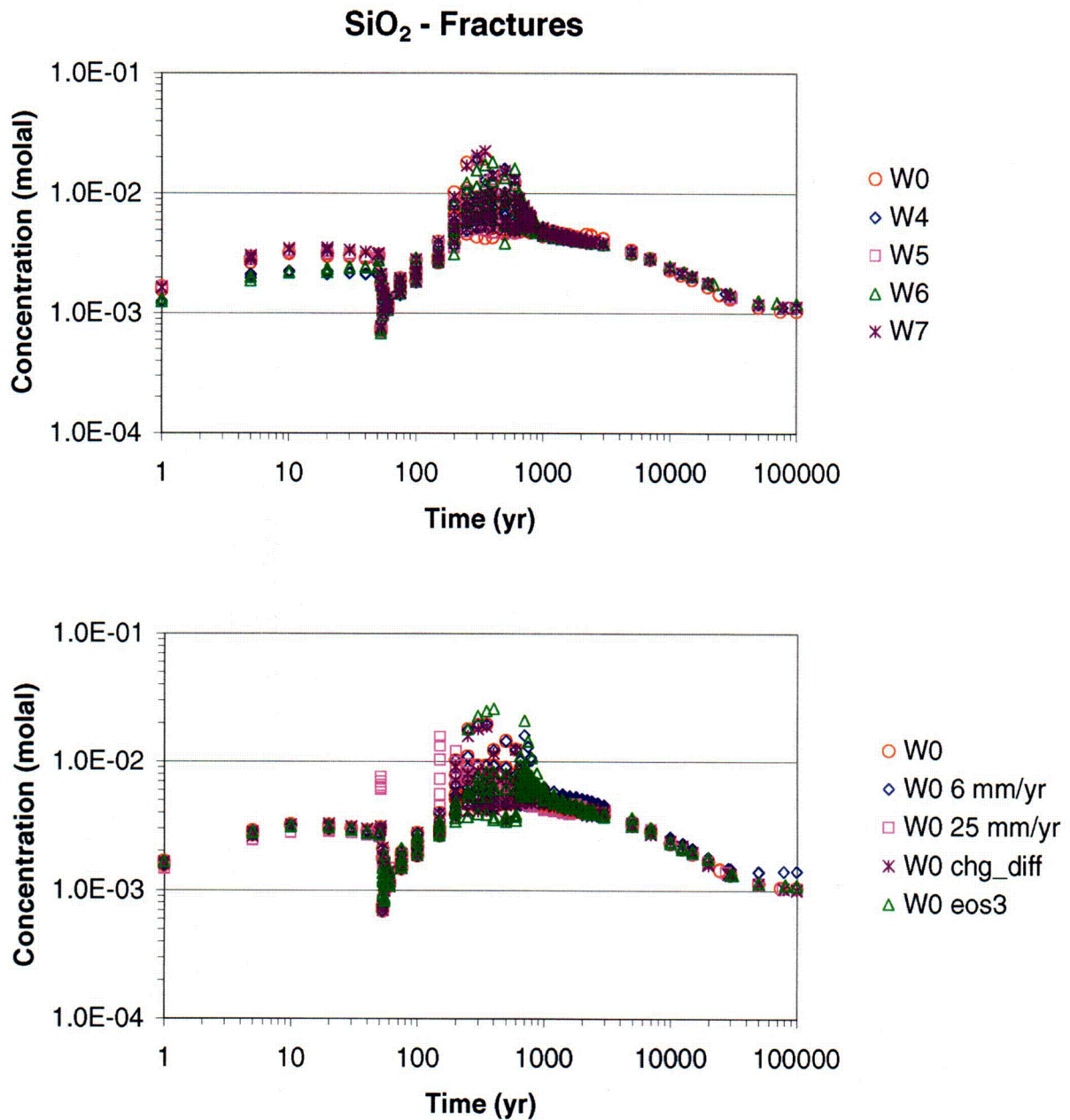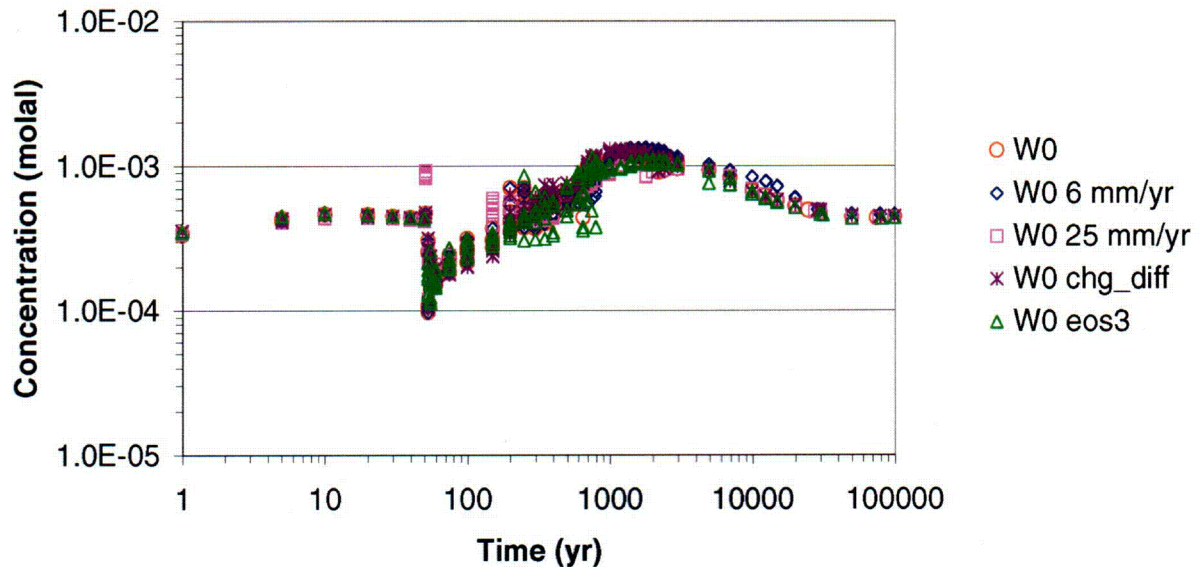
C90

F - Fractures

Output-DTNs: LB0302DSCPTHCS.002, LB0307DSTTHCR2.002

NOTE: Gridblocks are those with highest liquid saturation in fractures within a 25 m radius from drift center and a 45° arc from the drift crown. Data are shown for simulations using different initial water compositions (W0 – W7). Except as noted below, all simulations were run using a stepwise-increasing infiltration rate (6, 16, and 25 mm/y) and with vapor pressure lowering. Alternatives using Water W0 include simulations without vapor pressure lowering (W0 - eos3), and with fixed 25 and 6 mm/y infiltration rates (W0 - 6 mm/y and W0 - 25 mm/y, respectively).

Figure 6.8-38. THC Simulations (Tptpll Model REV02): Time Profiles of Modeled Total Aqueous Fluoride Concentrations in Fracture Water, in Areas of Highest Liquid Saturation above the Drift Crown
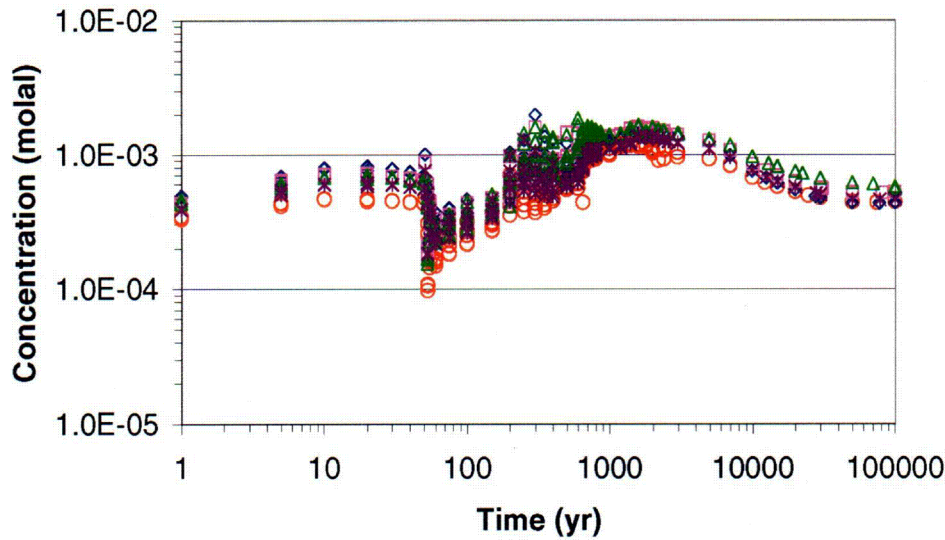
c91

6.8.5.4   Mineral Alteration and Porosity/Permeability Changes (Tptpll REV02)

The predicted effect of water-rock-gas interactions on flow patterns around the drift is much more noticeable in this model revision than in REV01. This is because simulations (using TOUGHREACT V3.0 (LBNL 2002 [161256])) make use of a better treatment of mineral precipitation at the boiling front than previously. In addition, the REV02 fracture porosity is approximately half the value used in REV01 simulations.

To provide a baseline for evaluating the effect of mineral precipitation and dissolution on flow, results of a TH simulation are evaluated first. A contour plot of predicted liquid saturations for the simulation (Figure 6.8-39) shows that at 2,400 years, well after the end of the boiling phase, the predicted liquid saturations in the vicinity of the drift reflect the capillary barrier effect of the drift. Ambient water percolation is deflected around the drift (even at much higher infiltration rates than considered here). As a result, liquid saturations in fractures are somewhat increased above the drift crown, relative to ambient values, and significantly decreased below the drift ("shadow" zone).

In contrast, a similar contour map of liquid saturations predicted with Water W0 using a THC simulation (Figure 6.8-40a) shows that after the same simulated time period, a zone of higher liquid saturation has formed 7–8 meters above the drift, reflecting partial deflection of flow at this location. This kind of "umbrella" effect results from a thin region of significantly lower permeability (Figure 6.8-40b) created by prior mineral deposition at the boiling front. In this case, the permeability has decreased by a factor of about 10 in this area. As a result, the shadow zone extends somewhat deeper below the drift, and liquid saturations at the drift crown are somewhat reduced, compared to the TH prediction. Similar figures for results using Water W5 as input initial composition show a more pronounced "umbrella" effect (Figures 6.8-41a), with the permeability decreasing by two to three orders of magnitude (Figure 6.8-41b) in the thin region of mineral precipitation. The results using the other waters are very similar. Consequently, the shadow zone below the drift is extended significantly. The time of fracture rewetting around the drift is delayed, and the vertical flux at the drift crown is reduced by up to a factor of 10 compared to the ambient flux without drift opening (Figure 6.8-42a).

Other THC simulations using Water W0 and the two fixed infiltration rates (6 and 25 mm/y), as well as the simulation neglecting water-vapor-pressure lowering, also predict to various degrees an umbrella effect above the drift (Figure 6.8-42b). The effect is most noticeable with the simulation without vapor-pressure lowering, which predicts that the rewetting of fractures at the drift crown is delayed until approximately 20,000 years and around 12,000 years in the matrix. However, in this case, this stronger effect could be unrealistic because some amount of water-vapor-pressure lowering is expected to occur in the natural system. By retaining more water in the matrix, fracture rewetting would be facilitated, because less imbibition of fracture water would occur into the matrix. It should also be noted that the revised rock properties used in this model, with a significant decrease in matrix permeability but also a decrease in capillary suction compared to REV01 properties (Table 6.4-1), make it more difficult for the rock to rewet after dryout.

The vertical flux predicted at the drift crown at 2,000 years (Figure 6.8-42a or b), without considering THC processes, can be compared with the vertical flux value shown in BSC (2003

[161530], Figure 6.2.3.1-3) for the same time period. Both values are consistent (2.9 × 10^{-7} kg m^{-2} s^{-1}, which yields approximately 9.5 mm/yr using the water density at the corresponding temperature [960 kg m^{-3}]). The flux peak on Figure 6.8-42 (a or b) at 1400 years (1.07 × 10^{-6} kg m^{-2} s^{-1}) corresponds to approximately 35 mm/year, consistent with values predicted a few meters above the drift at 1000 years in BSC (2003 [161530], Figure 6.2.3.1-3). As already mentioned in Sections 6.7.5.1 and 6.8.5.2, these peaks may not be fully resolved. However, these are much smaller than the percolation rate required for seepage to occur (250 mm/yr in BSC 2003 [161530], Section 6.2.3.2.3). When THC processes are taken into account, as discussed earlier, percolation rates at the drift crown are even smaller because percolating water is partly diverted by the zone of lower permeability created by mineral precipitation above the drift. However, the model considers a homogeneous fracture permeability and therefore cannot capture potential flow focussing through this zone of lower permeability. Because this zone is very thin and located several meters above the drift crown (Figure 6.8-41b), the focussing of flow locally through this zone is not anticipated to increase vertical fluxes at the drift crown much beyond what is predicted without considering THC processes.

In all simulations, the permeability decrease results primarily from the precipitation of amorphous silica and, to a lesser extent, calcite (Figures 6.8-43 through 6.8-46). The fracture porosity is predicted to decrease by approximately 4–7%, depending on the simulation. The maximum porosity decrease is predicted to occur in a thin zone during refluxing at the edge of the dryout zone, before the collapse of this zone around the drift. During that time, salt and gypsum precipitation account for up to around 15% of the volume of precipitated minerals (Figure 6.8-45). Gypsum precipitation is noticeable only with Waters W0 and W7, as expected, because these waters initially contain a higher proportion of calcium. Both salts and gypsum quickly redissolve when the fractures rewet. By 2,400 years, with all simulations except that without vapor-pressure lowering, fractures have rewetted, and the amount of precipitated solids (Figure 6.8-46) is predicted to remain essentially unchanged for the remainder of the entire simulated time period. For a long period of time in the simulation without vapor-pressure lowering, any water entering fractures immediately evaporates. This causes further salt deposition until well after 2,400 years, most notably directly above the drift crown (Figure 6.8-43), even though temperatures are well below boiling by this time. Increasing the infiltration rate from a fixed rate of 6 to 25 mm/year does not significantly alter the amount of precipitated solids, but shifts the mineral deposition zone towards the drift by approximately 1 m (Figure 6.8-44).

Other minerals besides amorphous silica, calcite, gypsum, and salts form or dissolve in small amounts. Some albite dissolution accompanied by stellerite precipitation is predicted to occur in fractures (typically 0.1% of the porosity or less). Illite and stellerite are predicted to be the most significant minerals precipitating in the rock matrix, with maximum amounts around 1% of the matrix porosity.

Tptpll Fractures - 2,400 Years (TH)
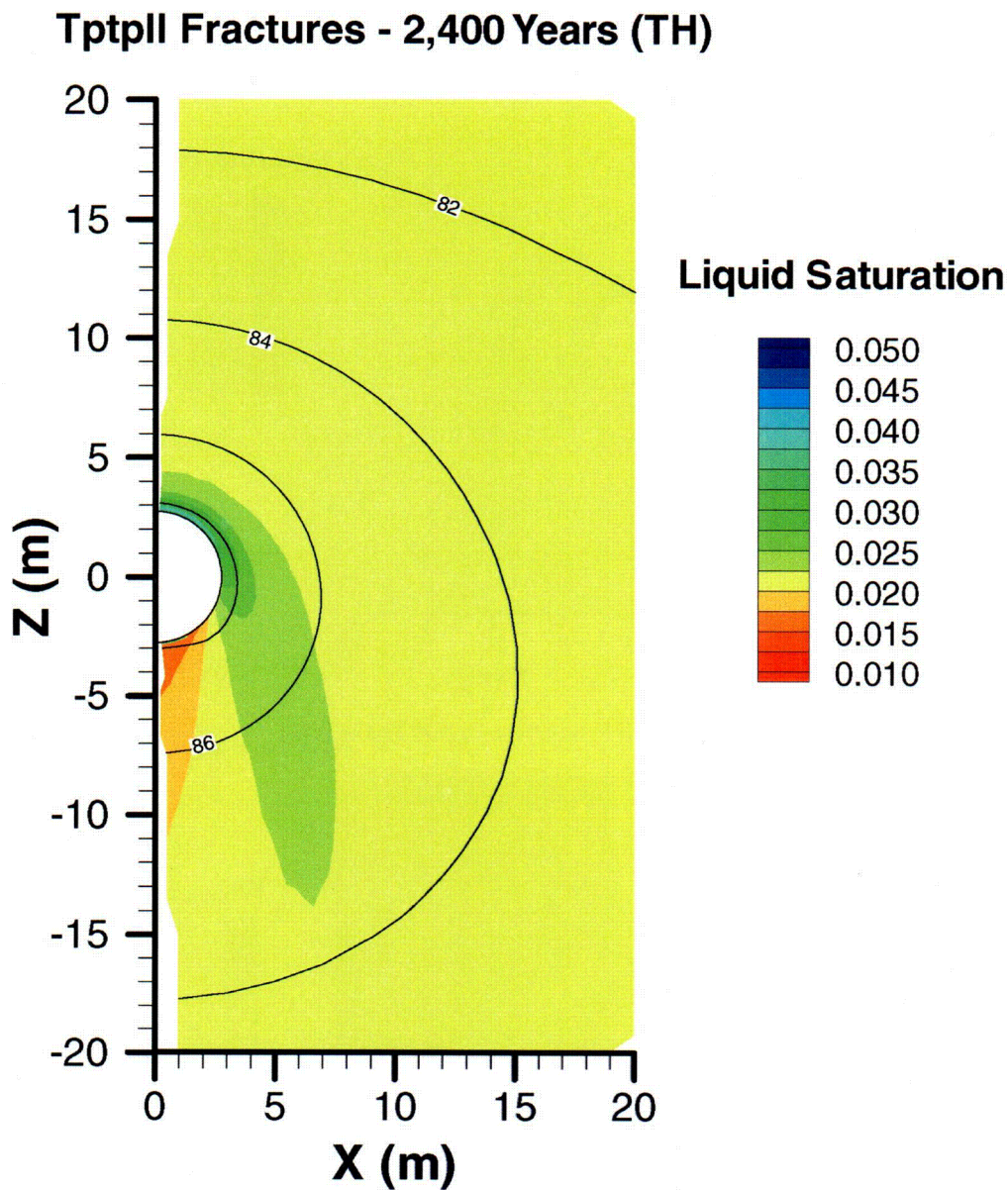
Output-DTN: LB0307DSTTHCR2.001

Figure 6.8-39.   TH Simulation (Tptpll): Contour Plot of Modeled Liquid Saturation and Temperature Contours (°C) in Fractures at 2,400 Years (No Chemical Reactions)

c9z

Tptpll Fractures - 2,400 Years (W0)

(a)

Tptpll Fractures - 2,400 Years (W0)

(b)
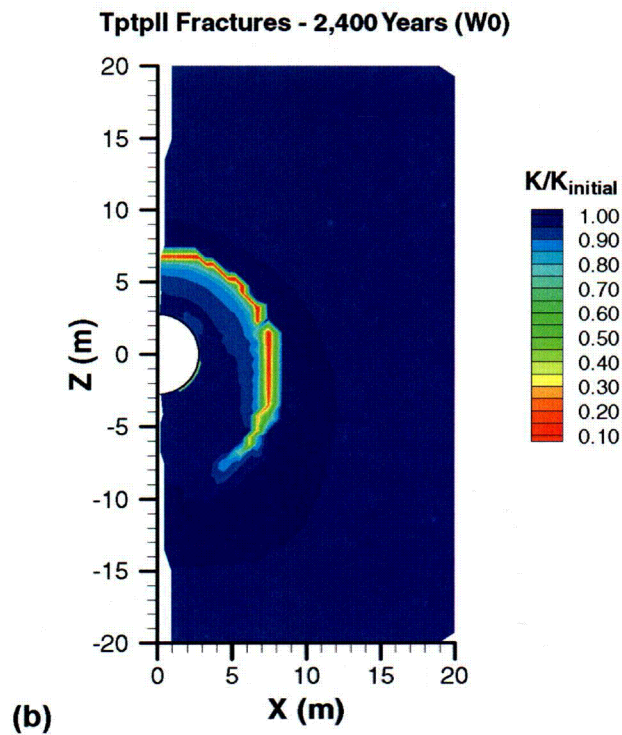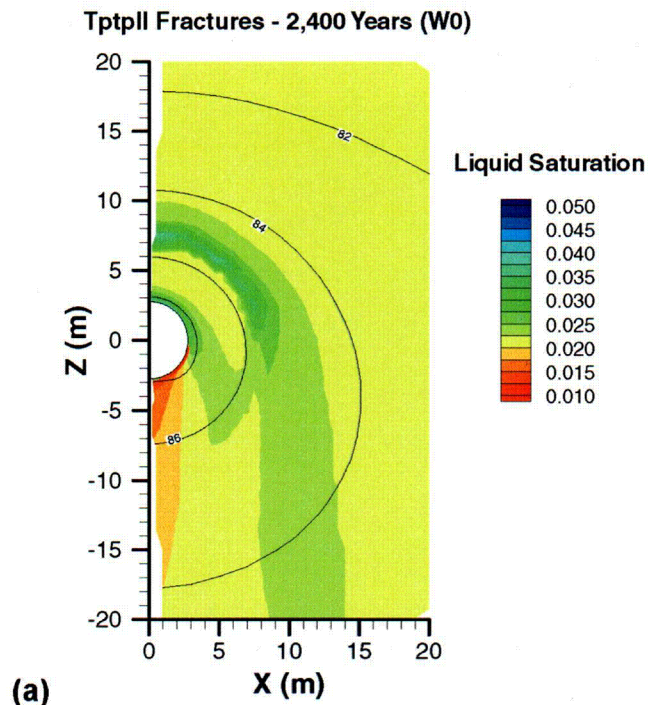
Output-DTN: LB0302DSCPTHCS.001

Figure 6.8-40.   THC Simulation (Tptpll—Water W0): Contour Plot of Modeled (a) Liquid Saturation and Temperature Contours (°C) and (b) Permeability Change in Fractures at 2,400 Years

Tptpll Fractures - 2,400 Years (W5)

Tptpll Fractures - 2,400 Years (W5)
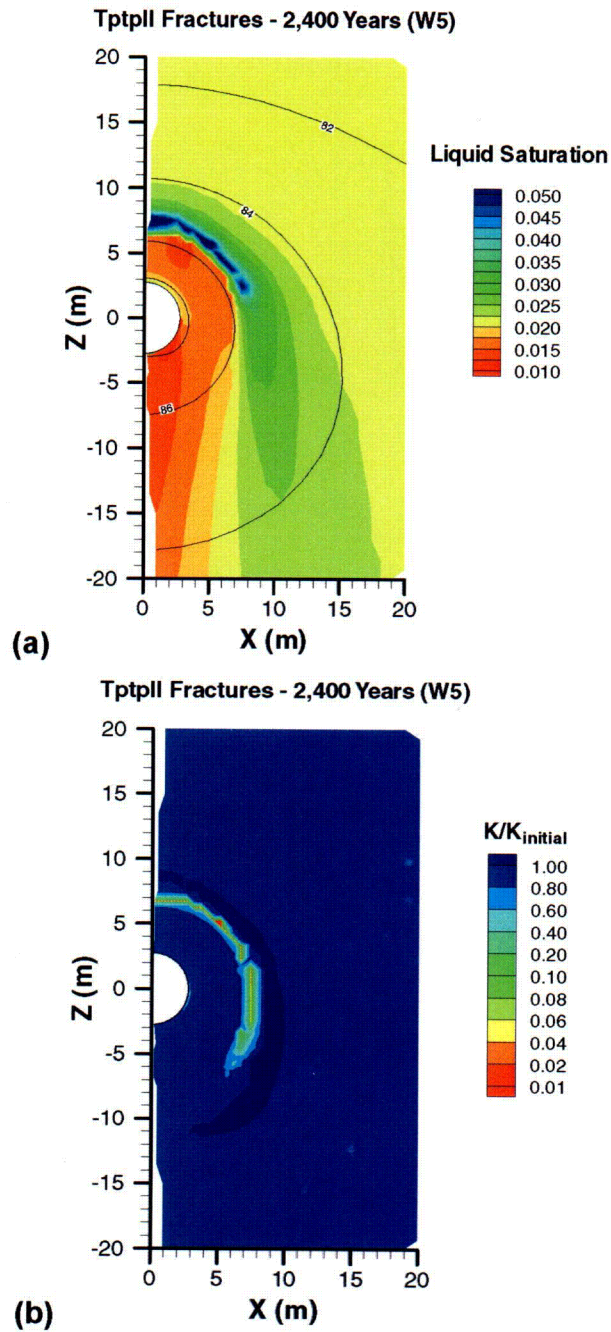
Output-DTN: LB0302DSCPTHCS.001

Figure 6.8-41. THC Simulation (Tptpll—Water W5): Contour Plot of Modeled (a) Liquid Saturation and Temperature Contours (°C) and (b) Permeability Change in Fractures at 2,400 Years

Fractures
Crown

Fractures
Crown

Output-DTNs: LB0302DSCPTHCS.002, LB0307DSTTHCR2.002
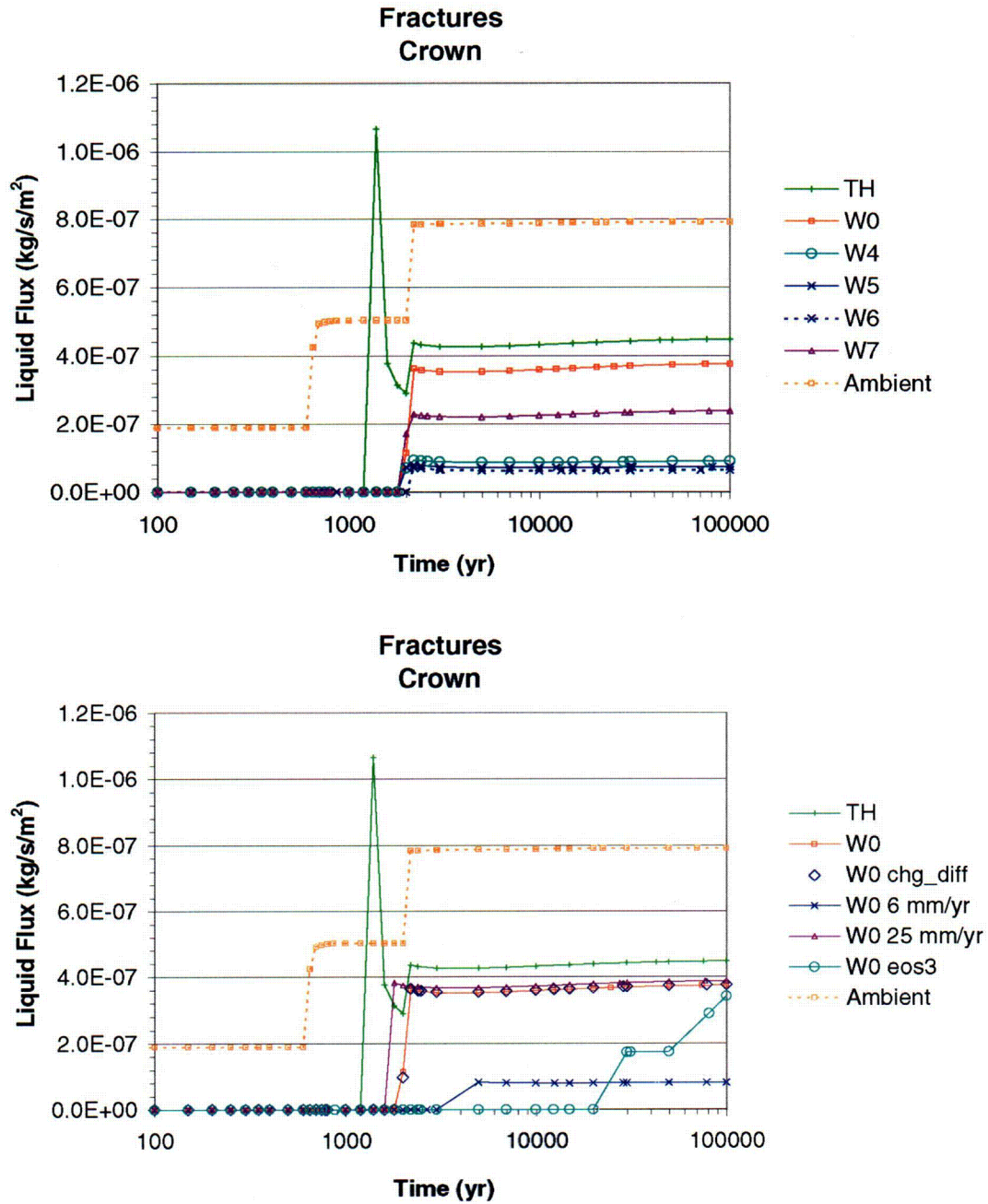
NOTE: Except as noted below, simulations consider vapor-pressure lowering and a stepwise-increasing infiltration rate (Table 6.8-2). Results are shown for various thermal loading simulations including: no chemical reactions (TH), five different input water compositions (W0, W4–W7), no vapor pressure lowering (W0—eos3), and two fixed infiltration rates (W0—6 mm/y and W0—25 mm/y). Predicted fluxes are also shown for ambient conditions (Ambient), without thermal load or a drift opening.

Figure 6.8-42.   TH and THC Simulations (Tptpll): Comparison of Modeled Liquid Flux at the Drift Crown in Fractures at 2,400 Years
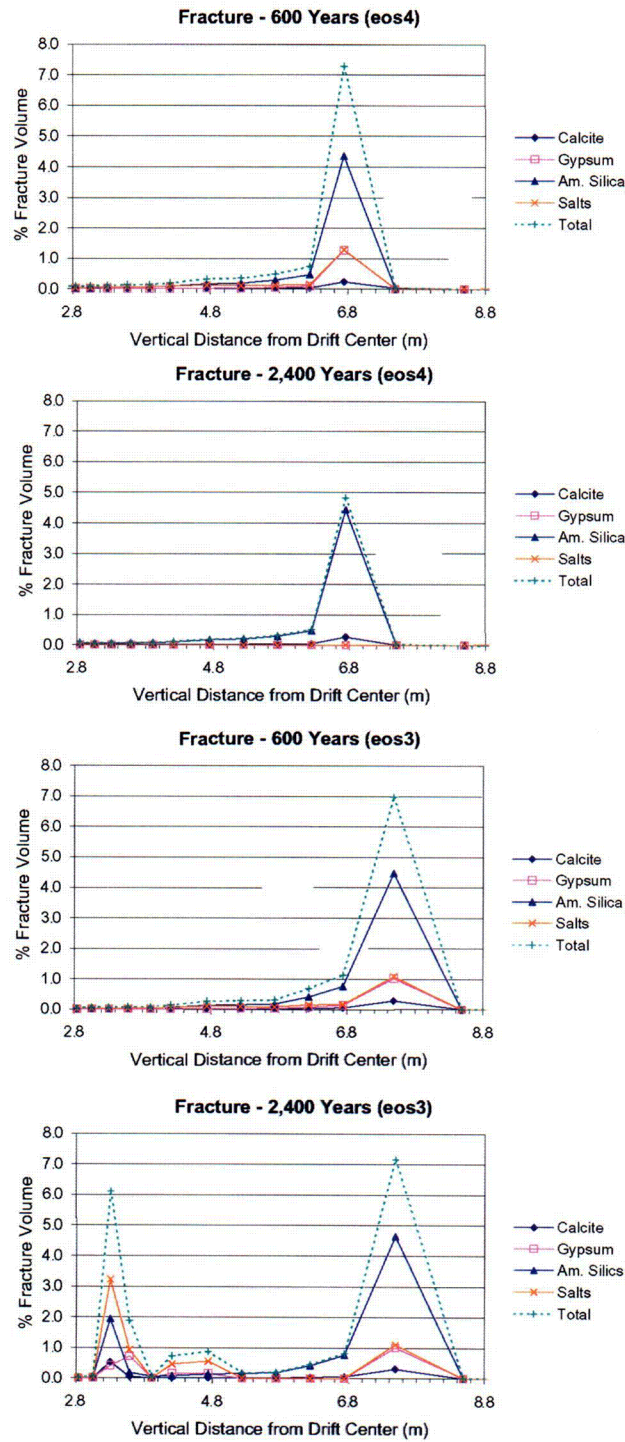
C95

Fracture - 600 Years (eos4)

Fracture - 2,400 Years (eos4)

Fracture - 600 Years (eos3)

Fracture - 2,400 Years (eos3)

Output-DTNs: LB0302DSCPTHCS.001, LB0307DSTTHCR2.001

NOTE: Profiles are shown for simulated times of 600 and 2,400 years, for simulations using Water W0 with vapor-pressure lowering (eos4) and without this effect (eos3). Infiltration rates are increasing from 6, to 16, to 25 mm/year in a stepwise manner (Table 6.8-2).

Figure 6.8-43. THC Simulations (Tptpll): Vertical Profile of Predicted Mineral Abundances above the Drift Crown

C96
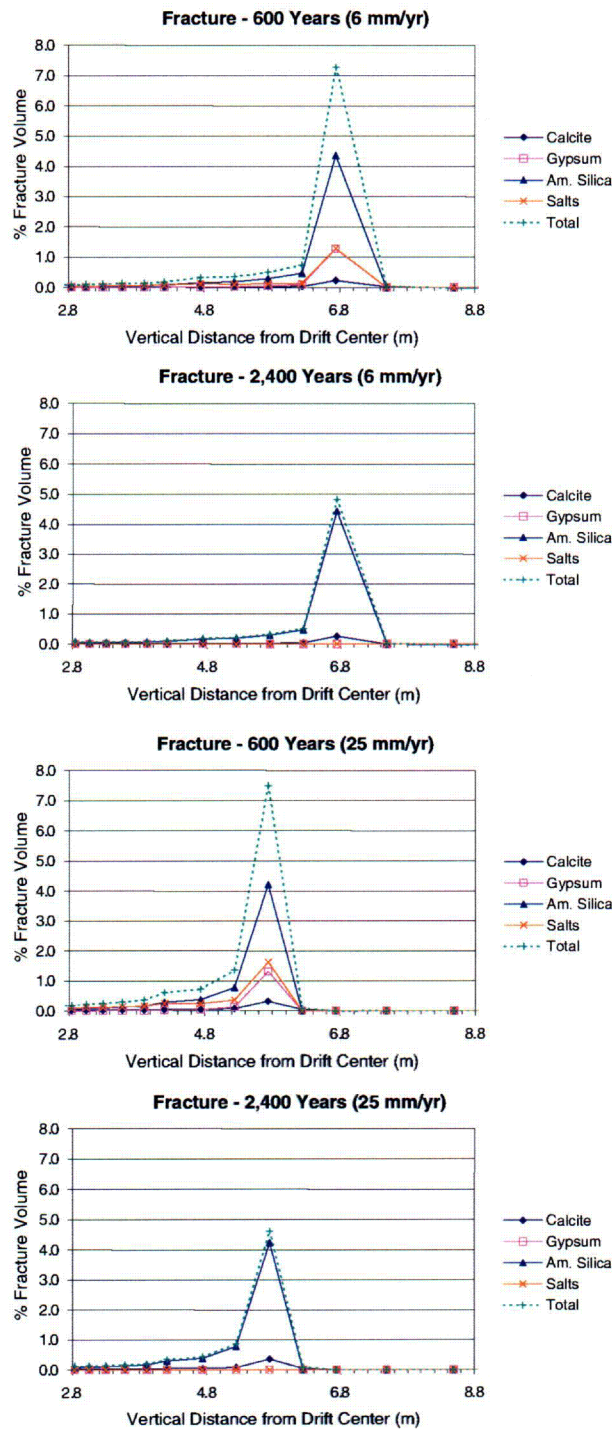
Output-DTNs: LB0302DSCPTHCS.001, LB0307DSTTHCR2.001

NOTE: Profiles are shown for simulated times of 600 and 2,400 years, for simulations using Water W0 with vapor-pressure lowering, and two different fixed infiltration rates (6 and 25 mm/year).

Figure 6.8-44.   THC Simulations (Tptpll): Vertical Profile of Predicted Mineral Abundances above the Drift Crown
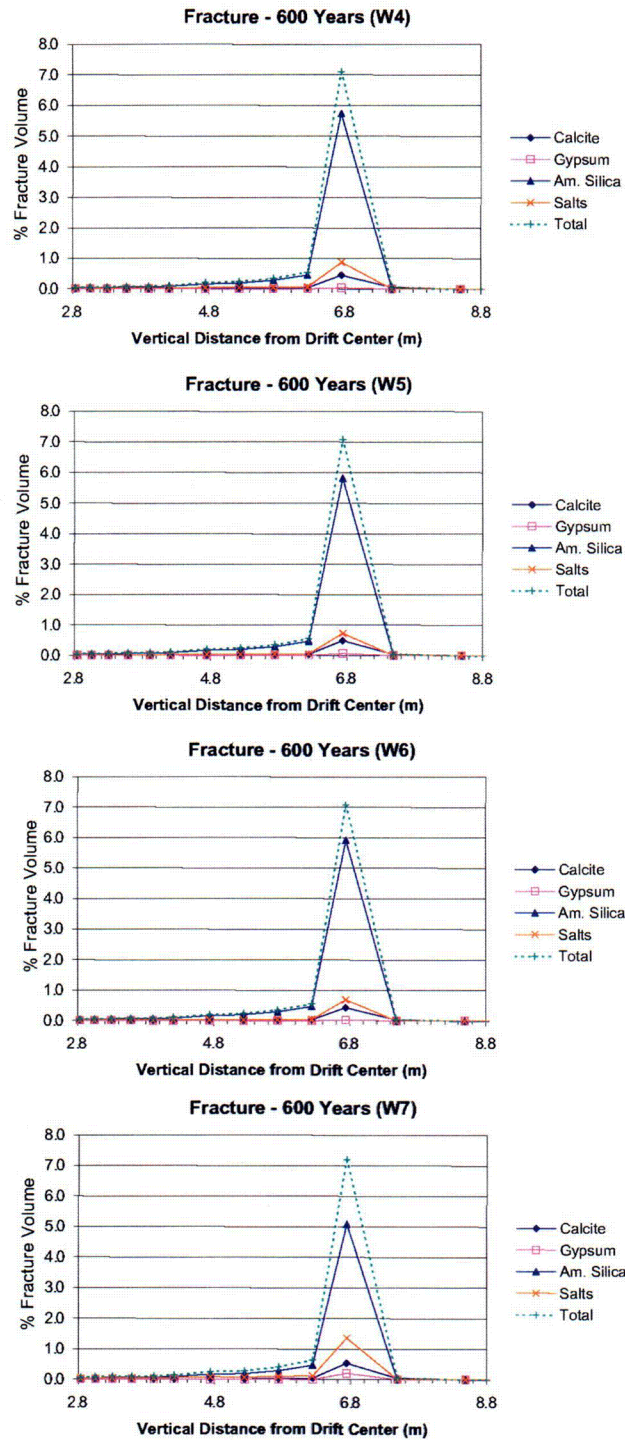
Output-DTNs: LB0302DSCPTHCS.001, LB0307DSTTHCR2.001

NOTE: Profiles are shown for a simulated time of 600 years, for simulations using vapor-pressure lowering
and four different input water compositions (W4–W7).

Figure 6.8-45.   THC Simulations (Tptpll): Vertical Profile of Predicted Mineral Abundances above the
Drift Crown

Output-DTNs: LB0302DSCPTHCS.001, LB0307DSTTHCR2.001

NOTE: Profiles are shown for a simulated time of 2,400 years, for simulations using vapor-pressure lowering and four different input water compositions (W4–W7). These profiles remain essentially unchanged for the rest of the simulated time period (100,000 years).

Figure 6.8-46.   THC Simulations (Tptpll): Vertical Profile of Predicted Mineral Abundances above the Drift Crown

C 99

6.9 MODEL UNCERTAINTY
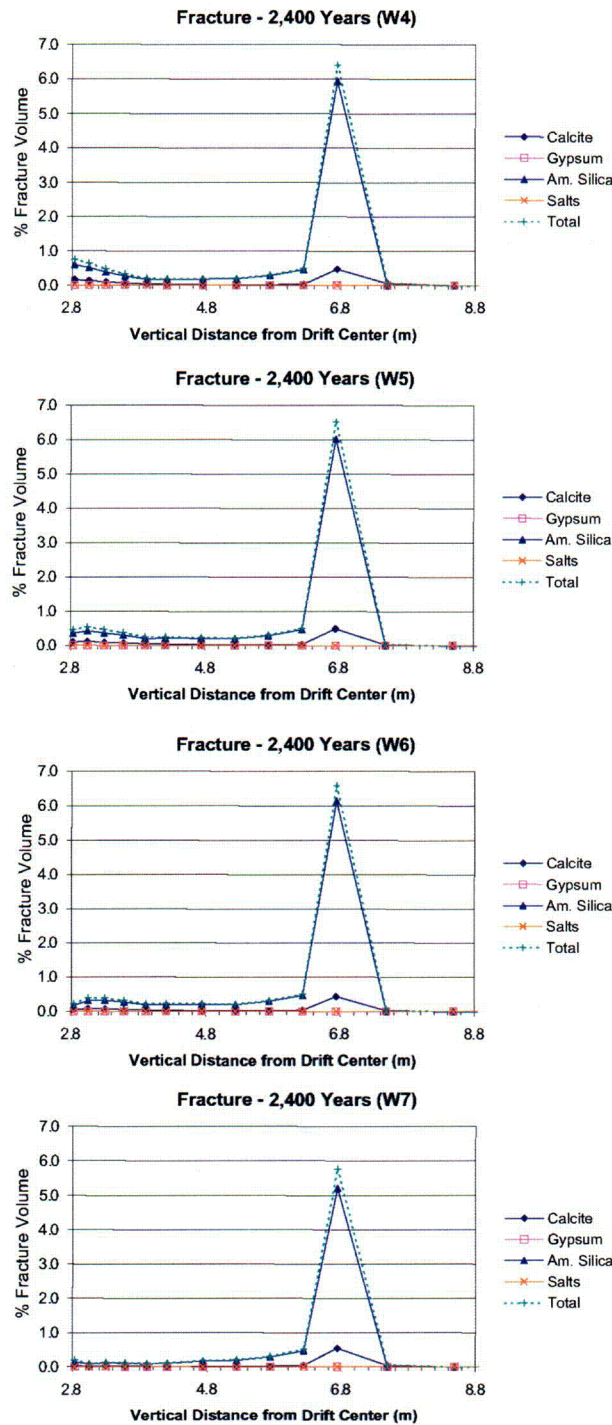
6.9.1 Potential Sources of Uncertainty

The simulations of THC processes include coupling between heat, water, and vapor flow, aqueous and gaseous species transport, kinetic and equilibrium mineral-water reactions, and feedback of mineral precipitation/dissolution on porosity, permeability, and capillary pressure (hydrological properties) for a dual-permeability (fracture-matrix) system. As such, the THC Seepage Model takes into account the effects of mineral dissolution and precipitation, the effects of carbon dioxide exsolution and transport in the region surrounding emplacement drifts, and the resulting changes to porosity, permeability, seepage, and chemical composition of percolating waters. The large number of input parameters, the numerical methods implemented in simulating these complex coupled processes, and the simplification and approximations pertaining to the physical setup of the model, all contribute to uncertainties in the predictions from these models. Uncertainties in model input data that could affect calculated water and gas compositions include:

- Thermodynamic data (equilibrium constants for mineral-water reactions and aqueous species dissociation)

- Kinetic data (rate constants, reactive surface areas, and activation energies)

- Initial compositions of pore water and pore gas

- Initial composition of infiltrating water and gas

- Infiltration rates

- Transport parameters (diffusion coefficients of aqueous species and gases, tortuosity)

- Initial rock mineralogy (model location and stratigraphy)

- Number of geochemical constituents included the simulations

- Number and types of potential secondary mineral phases

- Rock thermal, physical, and hydrological properties (including input data for both water-saturated and unsaturated rock)

Process model uncertainties may also affect the calculated water and gas compositions. These include:

- Formulation of models to simulate fluid flow in dual permeability media (e.g., fracture-matrix interactions; relative permeability and saturation-capillary pressure models)

- Activity coefficient models

- Kinetic mineral precipitation and dissolution models

- Inclusion or exclusion of certain specific thermal, hydrological, or chemical processes (e.g., active fracture model, vapor pressure lowering, mineral solid solutions, redox reactions)

Uncertainties in the setup of the model could also affect the results of the THC Seepage Model. These include:

- Physical model representation (stratigraphic/geologic extrapolations)

- Representation of the fracture and matrix continua in the model mesh

- Model discretization (in space and time)

- Boundary conditions (e.g., drift open versus closed to fluid flow)

Of these uncertainties, those directly affecting chemical processes would be most likely to have the most effect on predicted water and gas compositions. Such uncertainties, their treatment in the model, and their effect on model results are summarized in Table 6.9-1.

Note that temperature is also a critical parameter affecting modeling results, although it cannot be considered an uncertainty by itself (temperature can generally be predicted to within a few degrees; it is therefore not included in Table 6.9-1). Temperature directly affects equilibrium constants and reaction rates, the degree of water evaporation and boiling, and the amount of carbon dioxide volatilization from pore water, with direct implications for computed water and gas chemistries. Uncertainties affecting predicted temperatures could significantly affect computed aqueous and gas species concentrations. However, important changes in design heat load are likely to affect model results more than uncertainties associated with input parameters used to calculate temperatures (e.g., rock thermal conductivity and heat capacity). In this report, only the heat load from the current repository design was considered. This heat load leads to temperatures in the vicinity of emplacement drifts that exceed the boiling point of water for several hundred years if ventilation is not maintained after the 50-year preclosure period. The increased water-rock-gas interactions resulting from higher temperatures are expected to affect water chemistry and flow to a greater extent than if a lower heat load were considered. However, some of the effects of elevated temperatures, such as dryout and reduced permeabilities caused by mineral precipitation, could have positive aspects with respect to repository performance.

6.9.2 Evaluation of Model Result Uncertainty

The number of simulations that were performed to evaluate the uncertainty in model results was limited because the simulation of coupled THC processes is computation-intensive (typically 5–10 days CPU-time for one simulation). Nevertheless, the model sensitivity to key input parameters was evaluated (Sections 6.5–6.8). Furthermore, confidence in model results was obtained by comparing model results against data from the DST and laboratory experiments (Section 7), and improving the model conceptualization and mathematical formulation (Section 6.2–6.4) as necessary as to yield a reasonably good agreement between calculated and measured data (i.e., validation during development, as per AP-SIII.10Q, 5.4.1b, providing additional confidence).

In this study, the spread in predicted concentrations of aqueous species and CO_2 gas (i.e. Figures 6.8-12–6.8-21 and 6.8-25–6.8-38) is related to:

- The natural variability of input water compositions (Sections 6.2.2.1)

- The various investigated model conceptualizations (vapor-pressure model, drift location, stratigraphic columns, open versus closed drift wall) (Table 6-1)

- Ranges of input parameters other than water composition (in this case infiltration rates and CO_2 diffusion coefficients) (Section 6.8.5.3).

The relative spread caused by the variability of input water compositions (computed as standard deviation) is shown as a function of time in Table 6.9-2. This spread is up to around one order of magnitude and in many cases much less. As shown by comparing Figures 6.8-25a–6.8-38a with Figures 6.8-25b–6.8-38b, this spread is in most cases larger than the spread introduced by the various model conceptualizations and ranges of other input data considered in the model. Further evaluations of the spread in model result, as it directly ties to uncertainty, will be presented in the upcoming revision of *Abstraction of Drift-Scale Coupled Processes* (CRWMS M&O 2000 [123916]).

Uncertainties in kinetic and thermodynamic data could affect the standard deviations shown in Table 6.9-2, although the results of model validation against the DST and other laboratory experiments (Section 7), as well as the results of simulations of ambient conditions (Section 6.8.5.1), suggest these data are constrained to the extent that the model results are generally consistent with measured data. The model validation results (Section 7) also provide confidence that some of the other uncertainties listed in Table 6.9-1 do not significantly affect the spread in model results. This could be because model validation results are either not very sensitive to these uncertainties (at least over the period of time covered by the validation simulations) or that the effects of some of these uncertainties cancel out. Long-term effects of some of these uncertainties (e.g., ion exchange reactions, precipitation/nucleation kinetics) on model results may need further investigation, although it can be argued that the effect of these uncertainties on model results are already mostly captured by the variability in pore-water compositions input into the model.

Table 6.9-1. Summary of Uncertainties Affecting Chemical Processes in the THC Seepage Model

Category	Issue	Treatment	Consequences
Conceptual uncertainties	Geochemical system considered (minerals, gases, and aqueous species)	Treated by including major rock-forming minerals, major aqueous species, and major gases of interest (CO_2, air, water vapor) in the system, and also minor minerals such as clays. Effects of secondary mineral phase precipitation is most uncertain at higher temperatures and may require further evaluation. Uncertainty is limited under ambient conditions if ambient water concentrations can be reproduced. Trace minerals and aqueous species are not considered (not within the current scope for the THC Seepage Model). However, results of model validation (Section 7) against the Drift Scale Test and other experiments suggest the geochemical system, as modeled, is constrained enough to reproduce the experimental data within validation criteria. Also, the range of incoming waters considered in the model capture, at least in some part, the range of uncertainties related to the geochemical system.	Precipitation of secondary phases not currently included in simulations could affect the predicted composition of waters around the drift at high temperature. Reactions involving trace minerals (e.g., other clay minerals or Mg, Fe, Mn minerals) could affect pH which, in turn, could affect the precipitation/dissolution of other mineral phases and indirectly affect the concentrations of major species. The type of mineral precipitating could also affect the calculated porosity change (i.e., effect of different molar volume), although this effect would be minimal because the bulk of the precipitation consists of amorphous silica. Uncertainties affecting the precipitation of secondary phases would increase at near dryout conditions, however, such conditions (i.e., small liquid saturations) are not conducive to seepage.
	Drift wall conceptualization: closed vs. open to advective fluid flow; also, hydrological effect of ventilation is neglected.	Both cases of open and closed drift wall were addressed. Infiltration rates (even at high rates indicative of future wet climates) are below seepage thresholds, so there is little effect of closing the drift wall on water percolation fluxes around the drift. Evaporative concentration effects (due to ventilation) are indirectly taken into account by "downstream" in-drift evaporation models.	Boundary conditions of pressure and relative humidity in the drift could affect evaporative concentration effects at the drift wall, mostly during the preclosure ventilation period. In-drift interactions are not considered (this was not a goal of the THC Seepage Model).
	Precipitation/nucleation kinetics	Not treated This affects minerals such as silica and calcite, which have fast reaction rates. The reaction of calcite at equilibrium with a supersaturation gap (as done here) may approximate nucleation processes. Silica precipitation is modeled with a very fast reaction rate.	In areas where rapid boiling occurs, predicted silica concentrations are overestimated and silica precipitation is underestimated. However, the water saturation in these areas is very small and therefore the actual amounts of silica are minute.
	Water chemistry is not computed below a set water saturation limit (10^{-5}) or above a set ionic strength limit (4) (Activity coefficient model limitations)	In REV02 models, salt precipitation in the last remaining water when boiling or evaporating is taken into account using a simple model (Section 6.4.5). These salts are then available for dissolution upon rewetting, providing a conceptually correct (although simplified) representation of actual processes accompanying dryout and rewetting. In REV01 models, the composition of the last aqueous phase for which geochemical speciation is computed (prior to dryout) is saved. Water with this composition is assumed to mix instantly with percolating water during rewetting.	In REV02 models, the type and sequence of salts assumed to precipitate upon dryout affects computed water compositions at the very early stages of rewetting only. In REV01 models, assuming instant dissolution may overpredict dissolved salt concentrations when rewetting occurs.

Table 6.9-1.   Summary of Uncertainties Affecting Chemical Processes in the THC Seepage Model (continued)

Category	Issue	Treatment	Consequences
Conceptual uncertainties (cont.)	Vapor pressure lowering due to capillary pressure	Treated by running simulations with and without vapor pressure lowering.	No large effect on computed gas and water chemistries. However, a large effect on the predicted time of rewetting of fractures and matrix at the drift wall was observed. Neglecting vapor pressure lowering could increase the effect of evaporative concentration around the drift, resulting in higher water salinities, although this was not noticeable.
	Oxidation-reduction processes are neglected	Not treated (considers only oxidized conditions) Oxidizing conditions prevail in the unsaturated zone at Yucca Mountain such that the redox species considered in the THC Seepage Model (iron and sulfate) occur only in their oxidized state.	Limited anticipated effect because of the prevailing oxidized conditions. Likely no effect for iron and sulfate in the current models. Redox reactions involving microbial processes and species not presently modeled (nitrates, phosphates) could have a limited effect on pH.
	Mineral solid-solutions	Ideal solid-solution treatment for clays; no treatment for other minerals. Taken indirectly into account through adjustments of thermodynamic data necessary to reproduce ambient water compositions. Compositions of primary solid solution phases, when known, are directly taken into account by the relative amounts of individual end-members input into the model. Individual mineral phases with fixed solid-solution compositions (determined by analysis) are included in the simulations (e.g. zeolites).	Limited anticipated effect because solid solutions are partially treated as described in the adjacent table column. In the current THC Seepage Model, this would primarily affect the composition of precipitating alkali feldspars (thus affecting predicted Na and K concentrations). However, these minerals form nearly pure secondary phases in nature (i.e., as modeled). Zeolites in the repository host units (mostly stellerite) are not abundant and not particularly variable in composition.
	Ion-exchange and surface complexation	Not treated Dominant primary rock minerals in the repository host units are not strong ion exchangers (for major ions). THC seepage simulations do not include trace elements that could be strongly affected by surface complexation.	Limited effect for the current application range of the THC Seepage Model. However, a limited shift in the predicted concentrations of Na, K, Ca, and Mg could still affect significantly the composition of end-brines upon complete evaporation.
	Capillary pressure effect on chemical potentials of reacting species	Not treated It is taken indirectly into account through adjustments of thermodynamic data such that ambient water compositions can be reproduced.	Could potentially shift predicted concentrations of some species.
Data uncertainties	Infiltration water and initial pore-water composition	Five alternate water analyses are used in REV02 simulations, covering fairly well the compositional variability of pore waters in repository host units. Uncertainty can be assessed by comparing predictions of ambient water compositions with measured ambient pore-water compositions and pore-gas CO_2 concentrations.	Input water compositions affect predicted water compositions around the drift, and likely more so through infiltration/transport than through reaction.

Table 6.9-1. Summary of Uncertainties Affecting Chemical Processes in the THC Seepage Model (continued)

Category	Issue	Treatment	Consequences
Data uncertainties (cont.)	Carbon dioxide partial pressures	Composition of infiltrating water input into the model essentially dictates the boundary CO_2 pressure; therefore the uncertainty in infiltrating water composition overcomes this uncertainty. However, here, various infiltrating waters were assumed to equilibrate at the same boundary CO_2 pressure (around 3200 ppmv).	A large effect is not expected within the possible range of observed natural concentrations, because the range of thermally induced CO_2 partial pressures is much larger than (and thus overwhelms) background concentrations.
	Thermodynamic and kinetic data	Treated partly through sensitivity studies on long-term behavior of ambient system chemistry, assuming a fixed infiltration rate and different thermodynamic data for clays and zeolites (the model is very sensitive to the thermodynamic data for these minerals). When possible within the uncertainty of the original data, treated by revising the data to reproduce observed water compositions and mineralogical data. Other uncertainties treated through model validation (Drift Scale Test and laboratory experiments).	Currently one of the main uncertainties affecting predicted water compositions around the drift. However, it can be constrained by adjustments and model validation against observed data, such that ambient simulations predict concentrations consistent with observed values.
	Host rock mineralogy	Treated by considering alternative drift locations (Tptpmn versus Tptpll host rock unit). Bulk chemical composition of the repository host units do not differ significantly.	No significant effect on the predicted compositions of major aqueous species. Small amounts of fast reacting minerals containing elements present in minor quantities in pore water (e.g., fluorite) can have a large effect on the predicted concentrations of these minor species (e.g., F^-)
	Infiltration rates	Alternative infiltration rate scenarios are used.	Between 6 and 25 mm/y, there is a small effect on predicted concentrations at the drift wall. The effect would be greater under lower rates of infiltration (when reaction effects start to dominate transport), but such conditions would be less likely to cause in-drift seepage. At high-infiltration rates, most conducive to in-drift seepage, water compositions are more function of transport than of reaction with host rock minerals, such that the uncertainty regarding the composition of the infiltration water, rather than the rate of mineral dissolution/ precipitation, becomes more important.

Table 6.9-1. Summary of Uncertainties Affecting Chemical Processes in the THC Seepage Model (continued)

Category	Issue	Treatment	Consequences
Parameter uncertainties	Heterogeneity	Heterogeneous fracture permeability treated in REV01. Heterogeneity in matrix properties not treated. Local heterogeneity in mineralogy not treated; however, the bulk composition of host rocks is fairly uniform. Heterogeneity in initial water geochemistry not treated directly; treated indirectly through testing with alternate water compositions.	Possible local changes in predicted water compositions around the drift. However, the bulk composition of waters around the drift is not expected to be significantly affected, because the rock chemical composition and mineralogy in the repository units is fairly homogeneous.
	Transport parameters (effective diffusivity)	The CO_2 diffusion coefficient was changed by a factor of 6 between REV01 and REV02 analyses (and a factor of 30 since pre-REV01 simulations). Sensitivity to diffusion coefficient for aqueous species was not investigated. However, tortuosity was changed from 0.2 to 0.7 between earlier report revisions (REV00 and REV01) without noticeable effect.	CO_2 diffusion coefficient mainly affects in-drift predicted CO_2 concentrations during dryout. At other times, predicted CO_2 concentrations are mainly dictated by water compositions.

Table 6.9-2. Standard Deviations[1] in Water and Gas Compositions Predicted Using Five Different Input Water Compositions (W0, W4, W5, W6, and W7)

Time (yr)	pH	Ca	Mg	Na	Cl	$SiO_2(aq)$	HCO_3	SO_4
0	0.11	0.11	0.52	0.18	0.29	0.08	0.14	0.37
1	0.10	0.17	0.90	0.13	0.29	0.05	0.16	0.37
53	0.14	0.15	0.82	0 25	0.37	0.20	0.22	0.44
100	0.13	0.04	0.23	0.11	0.31	0.06	0.16	0.39
200	0.09	0.23	0.38	0.16	0.40	0.14	0.23	0.46
300	0.10	0.40	0.35	0 26	0.46	0.19	0.30	0.51
400	0.11	0.35	0.38	0 24	0.40	0.16	0.22	0.44
500	0.15	0.41	0.49	0 29	0.44	0.17	0.13	0.51
600	0.17	0.42	0.47	0.26	0.40	0.16	0.13	0.45
700	0.10	0.24	0.34	0.15	0.31	0.06	0.10	0.38
801	0.10	0.20	0.28	0.12	0.30	0.04	0.07	0.37
1,000	0.09	0.16	0.23	0.10	0.29	0.02	0.06	0.37
1,200	0.09	0.15	0.22	0.09	0.29	0.02	0.08	0.37
2,000	0.08	0.18	0.19	0.08	0.32	0.01	0.07	0.38
2,200	0.06	0.18	0.17	0.06	0.29	0.02	0.08	0.37
2,400	0.06	0.18	0.17	0.06	0.29	0.02	0.07	0.37
5,000	0.05	0.14	0.14	0.06	0.29	0.01	0.07	0.37
10,000	0.03	0.14	0.10	0.06	0.29	0.01	0.08	0.37
20,000	0.04	0.14	0.11	0.06	0.29	0.01	0.09	0.37
100,000	0.03	0.13	0.08	0.05	0.29	0.02	0.10	0.37

Time (yr)	K	F	NO_3	CO_2 (gas)	Ca/HCO_3	NO_3/Cl	Na/Cl	Ca/Cl
0	0.06	0.30	0.27	0.23	0.19	0.38	0.36	0.24
1	0.12	0.06	0.27	0.21	0.30	0.38	0.34	0.17
53	0.24	0.25	0.35	0.32	0.33	0.38	0.27	0.31
100	0.11	0.08	0.30	0.29	0.19	0.38	0.29	0.27
200	0.16	0.12	0.33	0.32	0.45	0.38	0.32	0.21
300	0.27	0.18	0.42	0.34	0.68	0.37	0.28	0.19
400	0.24	0.13	0.40	0.25	0.53	0.37	0.19	0.12
500	0.29	0.12	0.39	0.13	0.51	0.37	0.17	0.11
600	0.27	0.13	0.41	0.08	0.54	0.38	0.16	0.17
700	0.16	0.08	0.29	0.07	0.33	0.38	0.17	0.16
801	0.12	0.07	0.28	0.07	0.27	0.38	0.18	0.14
1,000	0.10	0.05	0.27	0.03	0.22	0.38	0.20	0.15
1,200	0.09	0.04	0.27	0.01	0.23	0.38	0.21	0.15
2,000	0.08	0.07	0.28	0.01	0.25	0.38	0.23	0.15
2,200	0.07	0.07	0.27	0.03	0.26	0.38	0.23	0.12
2,400	0.07	0.07	0.27	0.02	0.25	0.38	0.23	0.12
5,000	0.07	0.06	0.27	0.04	0.21	0.38	0.23	0.15
10,000	0.06	0.05	0.27	0.08	0.17	0.38	0.25	0.20
20,000	0.06	0.06	0.27	0.12	0.15	0.38	0.26	0.22
100,000	0.05	0.05	0.27	0.11	0.15	0.38	0.26	0.24

Output-DTN: LB0307DSTTHCR2.002

NOTE: [1] Standard deviations are computed using data depicted in Figures 6-25a through 6-28a (zones of highest liquid saturation above the drift) and represent:
   • For pH, standard deviation of pH values in (±) pH units
   • For other data, standard deviation of logarithmic values: i.e., (±) change in log10 values of concentrations and concentration ratios around the mean of log10 values (thus, a value of 0.5 corresponds to a total spread of one order of magnitude)